THESIS

INTRASEASONAL VARIABILITY OF THE WEST AFRICAN MONSOON AND AFRICAN EASTERLY WAVES DURING BOREAL SUMMER

Submitted by

Ghassan J. Alaka, Jr.

Department of Atmospheric Science

In partial fulfillment of the requirements

For the Degree of Master of Science

Colorado State University

Fort Collins, Colorado

Fall 2010

Master's Committee:

Department Head: Jeffrey Collett

Advisor: Eric D. Maloney

Wayne Schubert
Subhas Venayagamoorthy

ABSTRACT

INTRASEASONAL VARIABILITY OF THE WEST AFRICAN MONSOON AND AFRICAN EASTERLY WAVES DURING BOREAL SUMMER

Substantial subseasonal variability in African easterly wave (AEW) activity and cyclogenesis frequency occurs in the main hurricane development region of the Atlantic during boreal summer. A complete understanding of intraseasonal variability in the Atlantic and west Africa during boreal summer requires analysis of how the Madden-Julian Oscillation (MJO) modulates the west African monsoon and consequently AEWs. Because the MJO is predictable a few weeks in advance, understanding how and why the MJO impacts the west African monsoon may have a profound influence on Atlantic tropical cyclone prediction. This study documents the MJO influence on the west African monsoon system during boreal summer using a variety of reanalysis and satellite datasets.

This study aims to identify and explain the MJO teleconnection to the west African monsoon, and the processes that induce precipitation and AEW variability in this region. Intraseasonal west African and Atlantic convective anomalies on 30-90 day timescales are likely induced by equatorial Kelvin and Rossby waves generated in the Indian Ocean and west Pacific by the MJO. Previous studies have hypothesized that an area including the Darfur mountains and the Ethiopian highlands is an initiation region for AEWs. It is shown here that the initial MJO influence on precipitation and AEW

activity in the African monsoon appears to occur in these regions, where eddy kinetic energy (EKE) anomalies first appear in advance of MJO-induced periods of enhanced and suppressed AEW activity. In the initiation region, upper tropospheric temperature anomalies are reduced, the atmosphere moistens by horizontal advection, and an eastward extension of the African easterly jet occurs in advance of the MJO wet phase of the African monsoon, when AEW activity is also enhanced. These factors all support strong precursor disturbances in the initiation region that seed the African easterly jet and contribute to downstream development of AEWs. Opposite behavior occurs in advance of the MJO dry phase.

Moisture and eddy kinetic energy (EKE) budgets are examined to provide further insight as to how the MJO modulates and initiates precipitation and AEW variability in this region. In particular, meridional moisture advection anomalies foster moistening in the initiation region by anomalous flow acting across the mean moisture gradient. Additionally, positive (negative) upstream EKE tendency anomalies in advance of the MJO convective maximum (minimum) over tropical north Africa suggest wave growth (decay) near the entrance of the AEJ, while enhanced (suppressed) conversion of eddy available potential energy (EAPE) to EKE and barotropic conversion maintains downstream AEW growth (decay).

ACKNOWLEDGEMENTS

This research was made possible by several individuals. I would like to give my deepest appreciation to Dr. Eric D. Maloney, who provided invaluable motivation, guidance, and encouragement throughout this study. I would also like to extend my gratitude to Dr. Wayne Schubert and Dr. Karan Venayagamoorthy for serving on my Master's committee and providing insight on topics related to my study. The faculty and my peers at Colorado State University were paramount for refining my knowledge of the atmospheric sciences, which included several discussions during and outside of class. Specifically, I would like to thank Jim Benedict for his help in implementing a spatial filtering scheme and Walter Hannah for countless hours of advice and guidance in Rm. 231. I would like to extend my appreciation to my family and friends, whose support, encouragement, and confidence in me proved to be a constant inspiration. This study was funded by National Science Foundation project ATM-0828531: *Intraseasonal Variability of the West African Monsoon*.

TABLE OF CONTENTS

1. Introduction

1.1. Linking the Madden-Julian Oscillation to the West African Monsoon and African Easterly Waves

A complete understanding of intraseasonal variability over west Africa during boreal summer requires analysis of how the Madden-Julian Oscillation (MJO) modulates the west African monsoon and, consequently, African easterly waves (AEWs). Previous studies have provided evidence of 10-20 day and 30-90 day spectral peaks over tropical northern Africa (Sultan and Janicot 2003). While the 10-20 day peak may be associated with internal fluctuations of the monsoon, 30-90 day variability of rainfall and winds in tropical west Africa and the Atlantic intertropical convergence zone (ITCZ) is at least partly governed by the MJO (Maloney and Shaman 2008; Matthews 2004; Pohl et al. 2009; Janicot et al. 2009). This modulation by the MJO extends to Atlantic tropical cyclones (Maloney and Hartmann 2000; Mo 2000; Matthews 2004; Maloney and Shaman 2008). In particular, tropical cyclone activity in the Atlantic main development region is significantly enhanced (suppressed) about 5 days after MJO-related precipitation maximizes (minimizes) in the west African monsoon (Maloney and Shaman 2008; Camargo et al. 2009). Intraseasonal west African and Atlantic convective anomalies on 30-90 day timescales are likely induced by equatorial waves initiated in the Indian Ocean and west Pacific by the MJO (Matthews 2004; Janicot et al. 2009). These studies have shown that enhanced convection in the west African monsoon coincides with MJO

convective initiation over the Indian Ocean, although the Indian Ocean and west Pacific MJO anomalies that force west African monsoon variability likely occur in association with the previous Indian Ocean suppressed phase. It is hypothesized that Kelvin and Rossby waves, while traveling in opposite zonal directions, reach west Africa at approximately the same time to force variability in the west African monsoon region (Janicot et al. 2009).

This study aims to identify and explain the MJO teleconnection to the west African monsoon, specifically through the processes that induce convection and AEW variability east of Lake Chad. Several studies hypothesize that an area including the Darfur mountains and the Ethiopian highlands is an initiation region for AEWs (Thorncroft et al. 2008; Burpee 1972; Burpee 1974; Albignat and Reed 1980). Therefore, the MJO modulation of convection and budget terms in this initiation region will be one focus of this study to determine if this region effectively triggers intraseasonal AEW and convection variability in the west African monsoon. Of particular importance is how the moisture and eddy kinetic energy (EKE) budgets vary on MJO timescales in the initiation region and over the greater west African monsoon to provide clues as to how the MJO modulates and initiates variability in this region. Because the MJO is predictable a few weeks in advance, understanding how and why the MJO impacts the west African monsoon may have a profound influence on Atlantic tropical cyclone prediction (Vitart et al. 2010). A more in-depth discussion of equatorial wave theory, the MJO, AEWs and the west African monsoon intraseasonal variability that is relevant to the current study is now provided.

1.2. Equatorial Wave Theory

Equatorial waves are atmospheric phenomena that propagate parallel to the equator and are trapped within an equatorial waveguide produced by the change in Coriolis parameter with latitude. Equatorial waves are solutions to the "shallow water" equations, characterized by meridional mode number, frequency, planetary zonal wavenumber, and "equivalent depth" h of the shallow layer of fluid (Wheeler and Kiladis 1999). The equivalent depth, which is related to the phase speed by $c = \sqrt{gh}$, links the vertical structure equation and the shallow water equations through a separation constant (Lindzen 1967; Wheeler and Kiladis 1999). The relationship between phase speed and equivalent depth implies that deeper waves have faster phase speeds. The latitudinal extent of the waves is characterized by $(c/\beta)^{1/2}$, where c is the phase speed and β is the variation of the Coriolis force in the meridional direction (Matsuno, 1966). This relationship suggests that faster equatorial waves have greater latitudinal extent.

While convectively coupled versions of some waves produce significant outgoing longwave radiation (OLR) variations and are clearly visible on satellite, such as westward-propagating disturbances within the Intertropical Convergence Zone (ITCZ), other equatorial waves do not have a significant role in daily weather conditions and are primarily important from a theoretical standpoint (Wheeler and Kiladis, 1999). Kelvin waves and Rossby waves, in particular, are of key importance to this study due to their associated large-scale flow and low-frequency characteristics, as well as the ability to transmit information from the Indo-Pacific warm pool to the west African monsoon region. Different equatorial waves are may be analyzed through normalized OLR in the zonal wavenumber-frequency domain (Figure 1.1). Equatorial waves are divided into

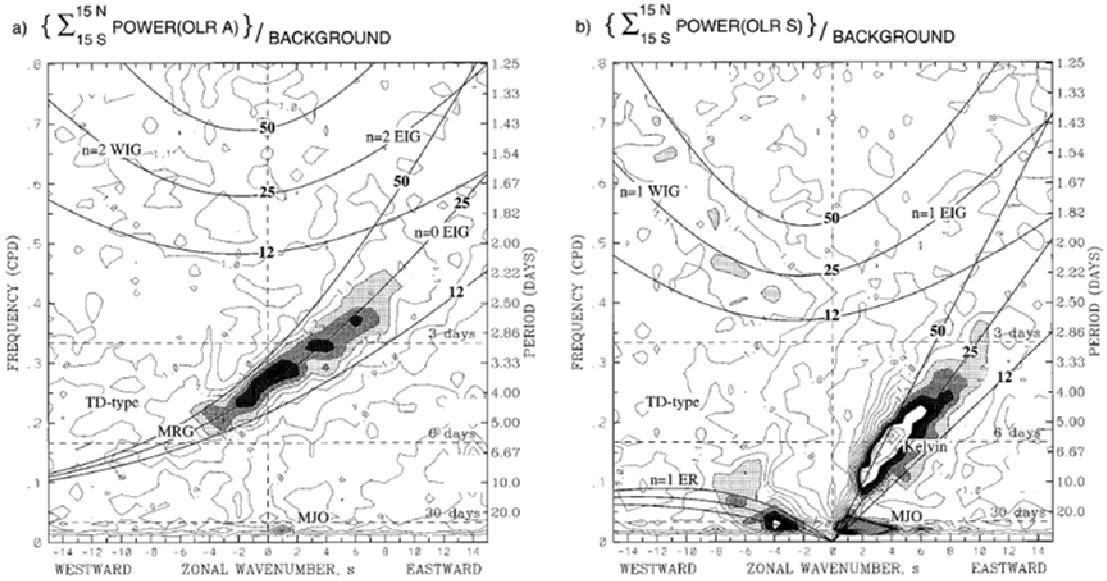

Figure 1.1. Normalized OLR power indicative of equatorial wave as in Figure 3 of *Wheeler and Kiladis (1999)*.

two regions by Wheeler and Kiladis (1999): symmetric and antisymmetric. Mixed Rossby-gravity waves are antisymmetric about the equator, while equatorial Rossby waves and Kelvin waves are symmetric about the equator. Inertia-gravity waves fall into both regimes. Although the MJO exhibits high power in the symmetric wavenumber-frequency domain, low power exists in the antisymmetric domain, which is likely a representation of the interaction between the MJO and Indian monsoon.

Kelvin and Rossby waves may be dry or convectively coupled, with each having different implications for equivalent depth and corresponding phase speed. Dry waves imply free propagation through the atmosphere without the continuous release of latent heat modifying the thermodynamic structure of the waves (Wheeler et al 2000). Although such waves lack convection, dry equatorial waves propagate energy efficiently to different parts of the world, and help to maintain weak tropical temperature gradients (e.g. Sobel and Bretheron 2000). Additionally, uncoupled waves travel much faster than their convectively coupled counterparts. For a dry wave that has half wavelength for the

depth of the troposphere, the equivalent depth and phase speed are 200 m and 40-50 m s^{-1}, respectively (Wheeler and Kiladis 1999; Lindzen 1967). When equatorial waves are convectively coupled, the phase speed is reduced, which consequently reduces the equivalent depth. Two schools of thought seek to explain why equatorial waves are slower when convectively coupled. The first theory is that latent heat release occurs in regions of upward motion, which effectively reduces the static stability and slows the waves (Gill 1982; Emanuel et al. 1994). The other theory is that shallower vertical modes of precipitation, like stratiform, reduce the vertical wavelength and hence equivalent depth, slowing the waves (Mapes and Houze 1995; Lindzen 1974; Mapes 1997). Wallace (1971) provided early evidence that equatorial waves modulate convection. Typically, convectively coupled waves receive more attention due to a direct modulating influence on precipitation patterns. The typical structures for Rossby and Kelvin waves are presented in Figure 1.2.

The equatorial Rossby (ER) wave is a westward-propagating disturbance with a period of 6-7 days and maximum amplitude in the upper troposphere (Yanai and Murakami 1970; Kiladis and Wheeler 1995). The ER wave exhibits a typical wavelength of ~9000 km (Wallace 1971), consistent with evidence for the role of the wave in large-scale tropical circulations. While Kiladis and Wheeler (1995) found that ER waves have a typical scale of wavenumber 6 and a period of 10-15 days in the Pacific, ER disturbances were observed over the TOGA COARE region as perturbation circulations with a broader range of timescales of 6-30 days (Kiladis et al. 1994). The classic Wheeler-Kiladis (1999) diagram reveals that the zonal extent of ER waves varies

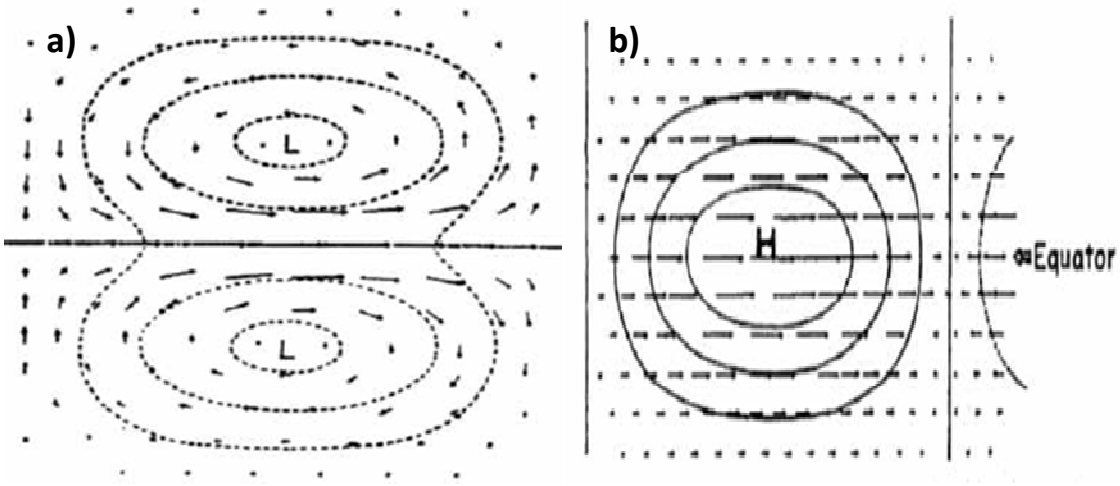

Figure 1.2. (a) Structure of an equatorial Rossby wave from Figure 4c of *Matsuno (1966)*. (b) Structure of a Kelvin wave from Figure 8 of *Matsuno (1966)*.

between wavenumbers 2-6, with the maximum amplitude around wavenumber 4 (Figure 1.1).

Matsuno (1966) defines the ER wave as an $n = 1$ solution to the shallow water equations characterized by slow, westward propagation and symmetry about the equator (Figure 1.2a). Here, n is the meridional mode and describes the relation between frequency and zonal wavenumber. ER waves are typified by the geostrophic relationship between pressure and velocity fields, resulting in anomalously strong zonal flow along the equator (Matsuno 1966). ER waves are structured with two areas of low pressure straddling the equator and centered between 10° and 20° of latitude. Since cyclonic flow is counterclockwise in the northern hemisphere and clockwise in the southern hemisphere, the two low pressure gyres enhance anomalous westerlies right along the equator, with weaker anomalies completing the cyclonic circulations on either side of the equator. The enhancement of anomalous westerlies at the equator in association with the Rossby gyres can support the observed phenomenon known as a "westerly wind burst" (McPhaden et al. 1988; Seiki and Takayabu 2007). The anomalous flow of the ER wave

generates differential planetary vorticity advection to either side of the gyres that results in westward propagation. As the symmetric cyclonic gyres propagate to the west, westward-propagating anticyclonic gyres are induced to the east and act to enhance easterlies along the equator (Kiladis and Wheeler 1995). Thus, the zonal wind will oscillate between anomalous westerlies and anomalous easterlies at a given location on the equator. This pattern supports rising motion and negative outgoing longwave radiation (OLR) anomalies within the poleward flow to the east of each low-level cyclone. Sinking motion and positive OLR anomalies exist within the equatorward flow to the west of each low-level cyclone (Kiladis and Wheeler 1995). ER waves have deep vertical structure of the first baroclinic mode in the troposphere (Wheeler et al, 2000). ER waves are of particular interest to this study due to their influence on off-equatorial fields. The role of ER waves in the spawning of convection in tropical north Africa will be investigated.

The Kelvin wave is an eastward-propagating, non-dispersive disturbance that explains a similar amount of convective variance as the MJO, yet is faster, has a wider range of spatial scales, and is more meridionally confined and centered on the equator (Wheeler and Kiladis 1999). The Kelvin wave signal links significant dynamical perturbations in the upper troposphere and lower stratosphere through convective coupling (Straub and Kiladis 2002; Wheeler et al. 2000). The Kelvin wave is an $n = -1$ solution to the shallow water equations that, like the ER wave, is symmetric about the equator (Matsuno 1966). The wave propagates like a gravity wave in the positive x-direction, while geostrophic equilibrium holds in the meridional direction with a balance between zonal velocity and the meridional pressure gradient force. Propagation speeds

for convectively coupled Kelvin waves are typically 10-25 m s^{-1}, although the wave may travel much faster in a dry atmosphere (Wheeler et al, 2000). When convectively coupled Kelvin waves initiated in the Indian Ocean propagate into the east Pacific, convection is no longer symmetric about the equator because of the equatorial cold tongue and its role in suppressing precipitation. In the east Pacific, convection associated with Kelvin waves is limited to the northern hemisphere (Straub and Kiladis 2002). Kelvin waves are structured with high pressure and low pressure located adjacent to one another in the zonal direction and centered on the equator (Figure 1.2b). These pressure anomalies decay in the meridional direction with a decay scale set by the equatorial radius of deformation (Matsuno 1966). Anomalous easterlies within the low pressure and anomalous westerlies within the high pressure produce convergence that supports positive convection anomalies in the Kelvin wave. The nature of the anomalous wind and convergence patterns results in the eastward propagation of the entire disturbance. Adiabatic cooling occurs within the region of surface convergence and upward motion that propagates the cold tropospheric anomalies and high surface geopotential anomalies eastward. This pattern causes convergence and precipitation to shift to the east over time. Diabatic heating anomalies may partially cancel adiabatic cooling anomalies, thus slowing eastward wave propagation. The role of Kelvin waves in the modulation of convection over west Africa will be examined in this study. In particular, fast eastward propagation may enhance monsoonal flow into west Africa and induce circulations crucial to initiating, maintaining, or diminishing convection. Further, temperature anomalies associated with Kelvin waves can alter the static stability of the atmosphere and thus make conditions less or more favorable for deep convection.

Together, convectively coupled Kelvin and ER waves provide a foundation upon which some aspects of the Madden-Julian Oscillation (MJO) structure may be described.

1.3. The Madden-Julian Oscillation (MJO)

1.3.1. MJO Structure

The Madden-Julian oscillation (MJO), which is the dominant mode of intraseasonal variability in the tropics, is characterized by interactions between the large-scale circulation and deep convection. The MJO was first identified by Madden and Julian (1971) as a 40-50 day oscillation in upper and lower tropospheric winds, surface pressure and temperature. However, the MJO may be more broadly defined as having a period between 30 and 90 days with a dominant spectral peak around 50 days (Zhang, 2005).

The MJO initiates in the western Indian Ocean with the onset of deep convection and propagates slowly eastward with time. As detected in rawinsonde data, the MJO wind anomalies in the lower troposphere are out of phase with the upper tropospheric winds, and demonstrate evidence of a large-scale circulation (Madden and Julian, 1971). This large-scale circulation is coupled to convection anomalies over the Eastern Hemisphere (e.g. Hendon and Salby 1994). The resulting circulation propagates to the east with propagation speeds of 5 m s^{-1} west of the dateline and 10-15 m s^{-1} east of the dateline. The phase speed increases at the dateline after the coupling of convection to the large-scale circulation is weakened. While the MJO is considered to be of planetary scale (described by wavenumbers one to three), much of the convective envelope and resulting

precipitation is non-uniform due to the effects of multiscale processes (Wheeler and Kiladis 1999; Wang 2005).

Much of the large-scale circulation response to the MJO may be described as a forced circulation response to a slowly-varying heat source. The anomalous wind field during an MJO event is of similar structure to the Gill model (Gill 1980), in which a positive heating anomaly is imposed on the equator. In the case of the MJO, the positive heating anomaly represents latent heat release from enhanced deep convection. An opposite-signed circulation response results from the MJO suppressed convection phase. Consequently, the response may be forced by a heating wave that travels in tandem with the disturbance and has both Kelvin and Rossby wave characteristics. The Rossby wave response is located to the west of the heating anomaly and is characterized by a low-level cyclonic eddy on either side of the equator. The Kelvin wave response occurs to the east of the heating anomaly and exhibits low-level easterly anomalies. The coupled Rossby-Kelvin wave response propagates to the east at 5 m s^{-1} along with the convective envelope, with the eastern front of the Kelvin wave response propagating rapidly ahead of the heating anomaly to the east and the Rossby wave response propagating to the west (Heckley and Gill 1984). Although the convective signal disappears around the dateline, the dynamical signal continues propagating eastward at 10-15 m s^{-1} as a Kelvin wave.

The dynamical signal associated with the MJO may reemerge into the Indian Ocean and start the next MJO cycle. Matthews (2008) describes two different types of MJO events. Primary MJO events are characterized by a precursor convective anomaly in the Indian Ocean in advance of the event that is not preceded by another MJO event. In some of these cases, MJO events may be initiated by a random blow-up of convection

that organized into a larger-scale event. Secondary MJO events are preceded by another MJO event and feature boundary-layer convergence, SST, and moisture anomalies in the Indian Ocean that pre-exist before the onset of new MJO convection.

1.3.2. MJO Theory

While observational studies have thoroughly documented various features of the MJO, the mechanisms that control its spatial structure and propagation characteristics are not well understood (Wang 2005). In order to develop a comprehensive theory for the MJO, a number of signature characteristics must be accounted for. In particular, the theory must explain features such as a dominant spectral peak ~50 days, the planetary scale circulation, a large-scale convective envelope, slow eastward propagation in the eastern hemisphere with an increase in phase speed in the western hemisphere, seasonally dependent poleward propagation, and a longitudinally dependent amplification or suppression of convection (Wang 2005). Since the MJO is characterized by interactions across a number of different scales, further comprehension of the small-scale structure and how it feeds back to the large scale could prove to be paramount to the complete understanding and prediction of the MJO (Majda and Stechmann 2009).

Due to the eastward propagation and similar dynamical structure, Kelvin wave dynamics were originally suspected as the mechanism behind the MJO. Since dry Kelvin waves propagate much too quickly (30-60 m s^{-1}) to explain the MJO propagation speed, Chang (1977) proposed convectively coupled Kelvin waves as a mechanism, since the phase speed is reduced relative to the dry Kelvin wave speed. Hendon and Salby (1994) argued that convectively coupled Kelvin waves have similar propagation speeds to the

MJO in the western hemisphere. However, the convectively coupled Kelvin waves move faster than the MJO in the eastern hemisphere. In fact, Wheeler and Kiladis (1999) showed that the MJO and convectively-coupled Kelvin waves appear in different parts of the wavenumber-frequency domain of OLR variance (Figure 1.1). Typically, the MJO is slower and on a larger scale than the convectively coupled Kelvin waves.

In the past few decades, several other theories have proposed physical mechanisms to explain MJO initiation, amplification and maintenance. In particular, these theories may be organized into five fundamental categories: 1) wave-Conditional Instability of the Second Kind (CISK), 2) wind-induced surface heat exchange (WISHE), 3) stratiform instability, 4) discharge-recharge, and 5) moisture mode instability.

Wave-CISK theory describes the MJO as an instability that arises from the interaction between convective heating and large-scale, low-level tropical wave convergence (Lindzen 1974). In general, CISK describes latent heat release and moisture convergence as positive feedbacks on each other, with this positive feedback providing a consistent energy source to maintain the instability. Specifically, latent heat and moisture convergence interact to transfer convective available potential energy (CAPE) to large-scale motions. Linear wave-CISK predicts increasing growth with increasing wavenumber (Chao 1995), which disagrees with the large-scale wavenumber one to three structure of the MJO. Another problem with wave-CISK is that such models produce eastward propagation that is faster than observations (Chang and Lim 1988; Wang 2005). Additionally, CISK requires that the atmosphere be conditionally unstable in the mean, whereas Emanuel (1994) observed that the tropical atmosphere is almost neutral to moist

convective ascent. Thus, CISK is able to describe some important features of the MJO, while failing to describe others.

In order to rectify the problem of the wave-CISK instability collapsing to small scales, a modified wave-CISK theory was developed that includes the effects of surface friction on moisture convergence within the atmospheric boundary layer. This particular type of wave-CISK is known as the "frictional-CISK" theory (Wang 1988), which includes boundary layer convergence that is forced in the equatorial wave trough ahead of the convective disturbance to support local frictional moisture convergence. Several studies have provided evidence for frictional moisture convergence ahead of convection associated with the MJO (Maloney and Hartmann 1998; Matthews 2000). Maloney and Hartmann (1998) found that the frictional moisture convergence that leads MJO convection has an important role in moistening the lower atmosphere and preconditioning the atmosphere for enhanced convection, which may be aided through shallow convection.

The WISHE, or wind-evaporation feedback, mechanism, first proposed by Neelin et al. (1987) and Emanuel (1987), asserts that the MJO is sustained by enhanced surface latent heat fluxes that arise due to the interaction of the anomalous MJO circulation with the mean flow. In particular, an eastward-propagating convective disturbance (such as the MJO) is sustained by anomalously high surface latent heat flux in regions of anomalous surface easterlies, which are located ahead of the convective disturbance. The anomalous surface easterlies add constructively to the mean easterly flow, increasing wind speed and, hence, latent heat flux to the east of MJO convection. As a result, convection is supported to the east of the disturbance, and the disturbance moves

eastward in response to the falling surface pressures and positive heating anomaly associated with the new convection.

WISHE has a number of drawbacks that deserve mentioning. Similar to wave-CISK, WISHE features wave growth at small scales and propagation speeds that are much too fast. Additionally, the WISHE mechanism depends on mean easterlies to produce zonal asymmetry in surface heat fluxes. However, observed basic state winds are westerly in the Indo-Pacific region where the MJO is most active. Data from TOGA-COARE show that large anomalous surface heat fluxes occur within the anomalous westerlies near and to the west of MJO convection (Lin and Johnson 1996), which is an observation that disproves the prototype WISHE model proposed by Emanuel (1987). Lin et al. (2000) argued that although the wind-evaporation feedback may partially explain modeled intraseasonal variability, it cannot sustain the oscillation for realistic parameters. Despite the aforementioned shortcomings, several recent studies assert that non-linear forms of WISHE may still be important in the maintenance and propagation of the MJO, and active investigations are ongoing along these lines (Neelin et al. 1987; Maloney and Sobel, 2004; Sobel et al. 2009).

"Stratiform instability" theory, as proposed by Mapes (2000), includes important interactions that involve both the first and second baroclinic modes of heating. In contrast, wave-CISK only considers processes that include the first baroclinic mode (i.e. – deep convective heating). The instability arises due to the interaction of convective and stratiform heating structures (Houze 1997; Mapes 2000). Specifically, anomalously warm upper-tropospheric temperatures and anomalously cool lower-tropospheric temperatures (above the boundary layer) reduce the convective inhibition (CIN), which

increases the frequency of deep convection. Three hours later, a stratiform mode appears in which anomalous heating is located aloft and anomalous cooling is located at lower levels. The stratiform mode generates eddy available potential energy (EAPE) due to a positive correlation of latent heat and temperature anomalies. Thus, the stratiform instability mechanism features a cycle of enhanced convective anomalies in the form of an eastward-propagating disturbance. The second internal mode temperature structure, which has a strong influence on CIN, may play a critical role in the observation of westward-moving cloud clusters inside an eastward-moving convective envelope (Mapes 2000; Oouchi 1999). While the second baroclinic mode is likely important to MJO structure, Benedict and Randall (2007) found that the observed temperature profile at the onset of convection suggests increased CAPE rather than reduced CIN.

Discharge-recharge describes the process through which atmospheric instability slowly increases through gradual moistening by shallow convection until deep convection can be supported and discharges the instability (Blade and Hartmann 1993; Hu and Randall 1994). The recharge process starts anew after the instability discharges. At the onset, the atmosphere slowly destabilizes through build-up of low-level moist static energy (MSE) and mid-tropospheric drying due to subsidence from the previous MJO event (Kemball-Cook and Weare 2001). The ensuing deep convection discharges MSE from the column, and the cycle must start again. Recharge-discharge results in a cycle of deep convective episodes that are separated by the recharge time. Several observational studies have found that MJO convection is preceded by low-level convergence, resulting in upward motion that produces a gradual moistening of the lower troposphere, accompanied by cooling and drying aloft (Sperber 2003; Lin et al. 2004; Kiladis et al.

2005; Agudelo et al. 2006). The corresponding vertical structure is tilted to the west as moisture anomalies deepen with the approach of the convectively active phase of the MJO. Woolnough et al. (2000) proposed that the strength and propagation speed of the MJO may be regulated by the feedback between convection and moisture. Despite the fact that the discharge-recharge model may play a significant role in the growth of MJO convection, Wang (2005) concludes that the moist processes associated with recharge-discharge theory are not sufficient in explaining the size or propagation speed of the MJO, although other evidence clearly argues for the importance of such processes (e.g. Benedict and Randall 2007; Thayer-Calder and Randall 2009).

Before discussing the moisture mode instability theory, the concept of gross moist stability (GMS) will be introduced. As originally defined, GMS is equal to the difference between total dry static stability (M_s) and gross moisture stratification (M_q) ($M = M_s - M_q$) (Neelin and Held 1987). M_s represents the column-integrated dry static energy export per unit vertical mass flux, and M_q represents the column moisture convergence per unit mass flux. Since this early work, GMS has also been used to argue that large-scale moisture convergence in the tropics may have important implications for the phase speed of the MJO (Neelin and Yu 1994). Conceptually, GMS represents the net export of MSE by divergent motions per unit mass flux in regions of deep convection. However, it is more useful to think of GMS as a measure of net stability in regions of moist convection.

Moisture mode instability theory is a recent, promising theory that explains many aspects of the MJO (Fuchs and Raymond 2007). A moisture mode is defined as a disturbance that exists under the weak tropical temperature gradients whose dynamics are largely determined by processes that control the tropical moisture field (Sugiyama 2009;

Sobel et al. 2001). Weak temperature gradients mandate a thermodynamic balance such that diabatic heating is balanced by adiabatic cooling. Moisture modes require strong moisture-convection feedbacks such that column specific humidity anomalies determine where convection will occur, and ensuing convection moistens the column to support more convection. Thus, moisture mode theory implies a strong correlation between tropical precipitation and total precipitable water, which is observed (Bretherton et al. 2004). Moisture mode instability requires negative values of effective GMS so that moisture anomalies are augmented in the free troposphere in response to vertical circulations driven by convection. The effective GMS combines MSE export by divergent circulations with sources of MSE, including surface fluxes and cloud radiative forcing. While studies such as Raymond and Fuchs (2009) suggest that unstable moisture modes require that vertical circulations alone import column-integrated MSE, GMS may also be effectively negative and support a moisture mode instability if divergent circulations are not exporting MSE from the column faster than surface fluxes and radiative forcing are importing it (Sugiyama 2009). Although the paradigm of the MJO as a moisture mode is gaining support, more observations are required to support such a mechanism.

1.4. West African Monsoon

The west African monsoon is a thermally-driven circulation that has a strong impact on rainfall and the large-scale circulations over tropical northern Africa during boreal summer. Overall, the monsoon flow is a forced response to the increased surface heating over west Africa during summer months, as well as the development of a cold

tongue in the Gulf of Guinea (Brandt et al. 2010; Janicot et al. 2010). Heating over west Africa induces ascent, which forms the Saharan heat low at approximately 15-20°N along Greenwich. Janicot et al. (2008) explain that the southwesterly monsoon winds are controlled by a pressure gradient between the Saharan heat low and the Santa Helena anticyclone, which is located near the Gulf of Guinea. This pressure gradient coincides with a sharp temperature gradient, with ascent within the hot Saharan region driving the monsoonal circulation (Lebel et al. 2010). The low-level southwesterly monsoon flow is met by low-level northeasterly dry Harmattan winds from the Sahara, which results in confluence from 10-15°N (Janicot et al. 2008). The low-level southwesterly flow from the Gulf of Guinea enhances moisture anomalies and primes the west African region for convection (Gu et al. 2004). The return monsoon flow in the mid-troposphere and the surface temperature gradient is responsible for the formation of the African easterly jet (AEJ; Section 1.5).

Tropical west Africa receives most of its annual rainfall in the boreal summer months from June to September. The increase in precipitation is associated with the seasonal variability of the ITCZ, which shifts from the Gulf of Guinea in April to 10°N in the heart of boreal summer, then retreats south again in late September or early October (Sultan and Janicot 2000; Le Barbe et al. 2002; Redelsperger et al. 2002). The seasonal variability of the ITCZ, in addition to the variability of winds, is a response to the varying state of the west African monsoon.

In June-July, the ITCZ and major rain zone shift to approximately 10°N north, which Sultan and Janicot (2000) argue is initiated by an intraseasonal westward-moving monsoon depression. Gu et al. (2004) propose that the abrupt shift is a manifestation of

the onset of strong convection near 10°N and the simultaneous suppression of rainfall in the Gulf of Guinea. In June, the onset of strong convection is positively correlated with spatially-limited, yet enhanced, low-level southwesterly flow (Janicot et al. 2008). Hagos and Cook (2007) assert that the enhancement of low-level westerlies creates an inertially-unstable environment, which also helps promote the northward shift of the ITCZ. The ITCZ creeps northward to about 8°N, and is clearly in a transition period throughout June. By July, low-level southwesterly flow is observed up to 20°N, with westerly components greater than 2 m s^{-1} over much of tropical north Africa. The ITCZ attains a quasi-stable state at about 10°N during July (Janicot et al. 2008). Importantly, Sultan and Janicot (2003) define two steps in the seasonal evolution of the west African monsoon that occur in June and July. The first, called the "preonset", advances the northward limit, or intertropical front, of southwesterly winds. The second, called the "onset", characterizes the abrupt northward shift of the ITCZ.

In August, the west African monsoon is at maximum amplitude, as evidenced by the northernmost location of the Saharan heat low and the highest pressures associated with the Atlantic subtropical ridge. Additionally, the westerlies associated with monsoon flow attain maximum coverage over Africa (Janicot et al. 2008), which indicates that moisture advection and, hence, precipitation are at a seasonal maximum. The ITCZ is relatively stable at around 10°N. By September, the west African monsoon begins winding down, with a noticeable decrease in westerly winds (Janicot et al. 2008). Strong southwesterly monsoon flow only penetrates northward to about 12°N, and the Saharan heat low starts to break down.

1.5. African Easterly Jet (AEJ)

The African easterly jet (AEJ) is a thermally-driven phenomenon that is located within strong low-level meridional potential temperature and geopotential height gradients between the Sahara and the Gulf of Guinea (Hsieh and Cook 2005; Thorncroft and Blackburn 1999). Low-level flow associated with the west African monsoon is paramount to the development of the AEJ, as shown in Figure 1.3. As low-level southwesterlies associated with the west African monsoon extend to 20°N, surface heating leads to dry adiabatic ascent up to about 600 hPa in association with the Saharan heat low. The 600 hPa return flow contributes to the thermal wind balance of the AEJ with the help of Coriolis acceleration in the same direction (Lebel et al. 2010). The mid-tropospheric jet, which is centered near 15°N in boreal summer, is associated with observed African easterly wave activity. The AEJ is characterized by strong easterly flow at 650 hPa that exceeds 12 m s^{-1}, as evidenced by Figure 3.20 and several studies (Thorncroft and Blackburn 1999; Burpee 1972; Reed et al. 1977). The AEJ is in thermal wind balance with the sharp temperature gradient between the Sahara and the Gulf of Guinea (Holton 2004).

The seasonal evolution of the AEJ during boreal summer is well-documented. Janicot et al. (2008) utilize observations and reanalysis to study AEJ variability. The jet is strongest and widest in June, with maximum amplitudes over 14 m s^{-1}. From June to August, the jet thins out and generally weakens, but is associated with an increasing amount of wave activity (Thorncroft and Blackburn 1999; Janicot et al. 2008). In September, the jet amplitude increases once again, but wave activity has started to diminish.

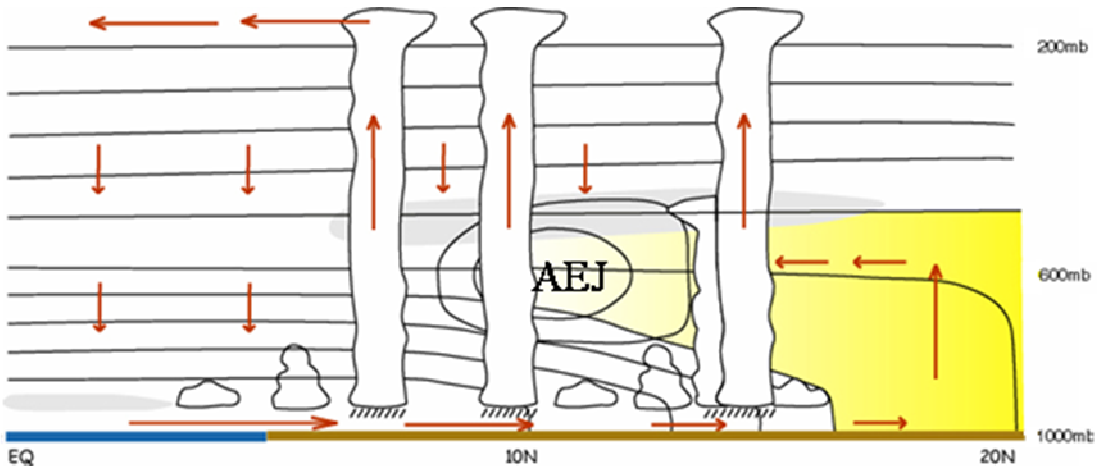

Figure 1.3. Schematic of the west African monsoon in boreal summer as in *Lebel et al. (2010)*. The solid, nearly horizontal lines are isentropes.

The barotropic-baroclinic instability associated with the AEJ is a focal point for many studies (Burpee 1972; Thorncroft and Hoskins 1994; Thorncroft 1995). The necessary condition for barotropic-baroclinic instability, as described by Charney and Stern (1962), states that such a jet may be unstable if the isentropic potential vorticity gradient is negative. Ertel's isentropic potential vorticity (IPV) is given by:

$$q = -g(\zeta_\theta + f)\frac{\partial \theta}{\partial p}. \qquad 1.1$$

Since $\frac{\partial \theta}{\partial p}$ is typically negative and the planetary vorticity *f* increases with latitude, the potential vorticity *q* typically increases from equator to pole. However, Figure 1.3 suggests that $\left|\frac{\partial \theta}{\partial p}\right|$ at 10°N is much greater than at 15°N, which is due to the contrast between moist, tropical west Africa and the dry adiabatic nature of the Saharan region. This decrease, in addition to a transition from cyclonic relative vorticity ($\zeta_\theta > 0$) to anticyclonic relative vorticity ($\zeta_\theta < 0$), results in a negative meridional IPV gradient near the AEJ. The satisfaction of the Charney-Stern necessary condition near the AEJ is manifested in AEW growth (Lebel et al. 2010; Thorncroft and Blackburn 1999).

1.6. African Easterly Waves (AEWs)

1.6.1. AEW Characteristics

African easterly waves (AEWs) are synoptic-scale disturbances that form near the African easterly jet (AEJ) over tropical north Africa during boreal summer (Burpee 1972; Kiladis et al. 2006). The typical period of AEWs is approximately 3-5 days, based on spectral analysis of the meridional wind by Burpee (1972). However, it has been suggested that some AEWs may exhibit periods of 6-9 days (Pytharoulis and Thorncroft 1999). AEWs typically exhibit similar scale and structure as Pacific easterly waves (Reed and Recker 1971), although their generation mechanisms likely differ. Several studies have pointed to AEWs as seed disturbances for Atlantic tropical cyclones (Landsea et al. 1998; Thorncroft and Hodges 2001), and the interannual variability of AEWs may modulate Atlantic tropical cyclones on similar timescales. Evidence exists that AEWs may travel on either side of the AEJ, with the two tracks combining over the eastern Atlantic (Thorncroft and Hodges 2001; Hodges et al. 2003). AEWs on the southern track are associated with more convection, while AEWs on the northern track are associated with larger values of kinematic wave activity (Pytharoulis and Thorncroft 1999). AEWs on the southern track propagate faster than those on the north track (Kiladis et al. 2006). Additionally, waves on the northern track maintain convection within the southerly flow, whereas convection associated with AEWs on the southern track begins within the northerly flow and shifts to the southerly flow over the Atlantic. In support, observations of AEWs on the southern track show that convection tends to be on the west side of the wave axis while over land and on the east side of the wave axis over the ocean (Kiladis et al. 2006). The wave axis appears to catch up to the convection

approximately at Greenwich. As the wave moves into the Atlantic, convection, now shifted to the east of the wave axis, is oriented southwest to northeast.

AEW convection is strongest near the AEJ, which meanders from about 10°N and 500 hPa in east Africa to about 15°N and 700 hPa over the eastern Atlantic (Kiladis et al. 2006; Figure 3.20). Over Africa, low-level westerly winds are located beneath the AEJ, enhancing AEW convection. While the AEJ is predominantly composed of easterly winds, meridional wind perturbations occur that are characteristic of southerly and northerly flow perturbations associated with AEWs. Kiladis et al. (2006) notes that the perturbation streamfunction associated with AEWs exhibits a southwest-northeast tilt south of the AEJ and a southeast-northwest tilt north of the AEJ. Thus, waves may grow via barotropic energy conversions on either side of the AEJ. Specifically, the horizontal wave tilt extracts easterly momentum from the AEJ, allowing conversion of zonal kinetic energy to eddy kinetic energy. Kiladis et al. (2006) found that the meridional and zonal extents of AEWs are much greater than previously suggested. Meridionally, AEWs may extend from 20°S to 40°N, while the zonal wavelength is about 4000 km (Diedhiou et al. 1999).

As AEWs propagate to the west, certain characteristics vary or evolve. For example, the phase speed of AEWs varies from 11.5-12.5 m s^{-1} east of Greenwich to 8.5 m s^{-1} over the central Atlantic. Kiladis et al. (2006) found that the OLR signal propagates slightly slower than meridional wind and vorticity fields. Additionally, NCEP reanalysis and observations of the waves during GATE provide evidence for the dynamical contraction of AEW zonal wavelength (Diediou et al. 1999; Reed et al. 1977).

AEWs are typically coupled to deep convection and feature a vertical structure that extends to the tropopause. Kiladis et al. (2006) utilize reanalysis to show that the 200 hPa circulation is of the opposite sense to the low-level circulation and slightly displaced to the east. Analysis of the meridional wind at 10°N reveals a first baroclinic structure, with westward tilted wind maxima below 300 hPa and opposing meridional flow above 300 hPa (Reed et al. 1977; Kiladis et al. 2006). The meridional wind structure of AEWs at 15°N is quite different, with eastward tilted meridional wind maxima below 500 hPa, and westward tilts in meridional wind maxima above 500 hPa (Kiladis et al. 2006), suggesting baroclinic conversion. While studies have found that the maximum meridional wind perturbation occurs around 700 hPa (Reed et al. 1977; Burpee 1975), Kiladis et al. (2006) discovered that the maximum occurs in the lower troposphere over Africa and occurs near to 500 hPa over the Atlantic. Vertical motion peaks at 700 hPa and 400 hPa over Africa, corresponding to the influence from shallow and deep convection. Accordingly, divergence maximizes at 250 hPa, with a secondary signal at 500 hPa, while convergence peaks at low levels. Once the waves propagate offshore, the lower vertical motion peak disappears (Kiladis et al. 2006).

1.6.2. AEW Initiation

The initiation of African easterly waves (AEWs) is still not that well understood. It is known that the waves initiate somewhere to the east of Greenwich in the west African monsoon region. Several studies assert that AEWs could arise from small amplitudes and an unstable African easterly jet (AEJ; Rennick 1976; Simmons 1977; Thorncroft and Hoskins 1994a,b). Specifically, a reversal in the meridional gradient of

potential vorticity (PV) satisfies the Charney-Stern necessary condition for instability (Charney and Stern 1962), which allows AEWs to grow via a mixed barotropic-baroclinic instability mechanism for about 50° of longitude (Dickinson and Molinari 2000). While waves may grow in this fashion, the short zonal extent of the unstable AEJ may not be ample enough to explain the observed AEW growth rate. In fact, with realistic surface damping, the AEJ is near neutral stability (Hall et al. 2006). Therefore, many studies have determined that AEWs are most likely initiated in the form of finite-amplitude precursors east of 10°E (Burpee 1972; Carlson 1969; Thorncroft et al. 2008).

Terrain-induced convection is a likely source of finite amplitude disturbances that generate AEWs, given that the orography of northern Africa helps to generate mesoscale convective systems (MCSs; Hodges and Thorncroft 1997; Berry and Thorncroft 2005; Mekonnen et al. 2006; Carlson 1969). North Africa features several topographic features that could spawn convection, including the Ethiopian highlands, Darfur Mountains, the Cameroon highlands, and the Fouta Djallon highlands. Figure 1.4 features a topographical map of northern Africa and the primary ranges that may be important for AEW initiation and maintenance. The Ethiopian highlands are centered at 10°N, 35°E and feature continuous elevation above 1500 m, with summits reaching above 4500 m. The Darfur Mountains (or Marrah Mountains) are located at approximately 15°N, 23°E and are characterized by a plateau above 800 m and several volcanic peaks above 3000 m. The Darfur Mountains are of particular interest in this study due to their proximity to the entrance of the AEJ. The Cameroon highlands (8°N, 10°E) and Fouta Djallon highlands (10°N, 10°W) may be important for spawning convection after AEWs have already developed and propagated downstream. Additionally, the Ahaggar Mountains

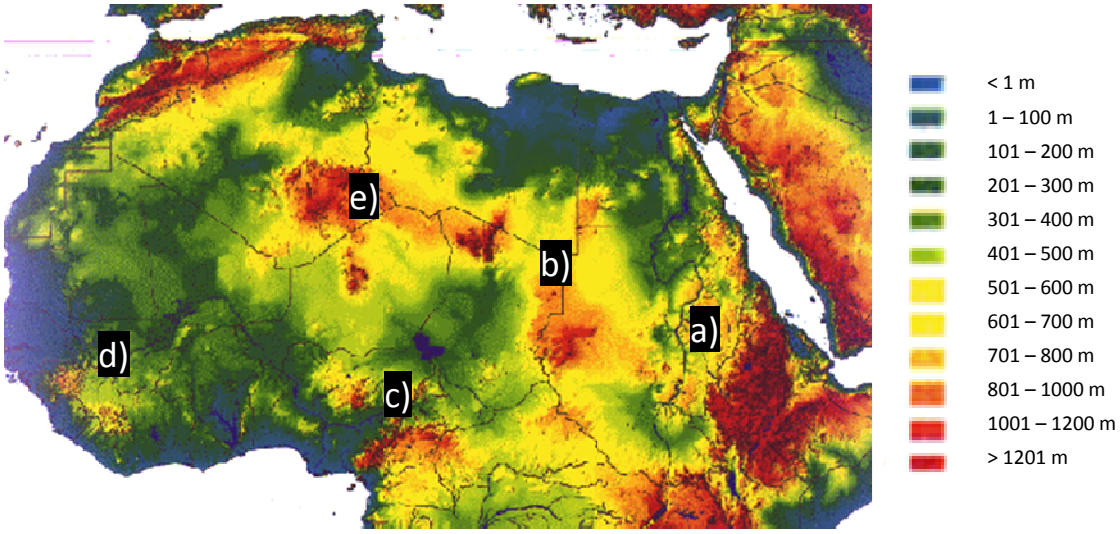

Figure 1.4. Topographical map of northern Africa. The shading represents height as described by the table to the right of the image. Four topographical features of importance are a) the Ethiopian highlands, b) the Darfur Mountains, c) the Cameroon highlands, d) the Fouta Djallon highlands, and e) the Ahaggar Mountains.

(23°N, 5°E) may be important for modulating large-scale circulation patterns over tropical Africa, although AEWs are not often observed that far north. Thorncroft et al. (2008) contend that AEWs are initiated by a localized forcing in the form of upstream latent heating associated with topography, which is realistic given that upstream latent heating strengthens the PV strip associated with the AEJ and provides a more favorable environment for AEW growth (Schubert et al. 1991).

Kiladis et al. (2006) assert that convection with AEWs is initiated by dynamical forcing associated with the wave, which forces vertical motion at low levels and couples the wave to deeper convection as it matures. However, the large zonal wavelength and large meridional extension from the northern hemisphere extratropics to across the equator could imply that extratropical forcing contributes to the initiation AEWs as well.

1.7. MJO Modulation of West African Monsoon and AEWs

Since the MJO is the dominant mode of intraseasonal variability and shows prediction skill to two-three weeks, a connection to the west African monsoon and AEWs could prove to be valuable for forecasting the activity of these waves and resulting tropical cyclones that they spawn. However, the influence of the MJO on winds, precipitation and AEWs associated with the west African monsoon are not well understood (Maloney and Shaman 2008). While some studies have found a relatively weak relationship between the MJO and tropical north Africa (Maloney and Hartmann 2000a; Knutson and Weickmann 1987; Annamalai and Slingo 2001; Wheeler and Weickmann 2001; Knutson et al. 1986), the work of Matthews (2004) and Janicot et al. (2009) suggest that the MJO may have a significant remote influence on the region.

Despite the fact that 10-25 day timescales dominate west African monsoon variations, substantial intraseasonal variability occurs on timescales greater than 25 days (Maloney and Shaman 2008; Janicot and Sultan 2001; Sultan et al. 2003). Janicot and Sultan (2001) discovered a 40-day statistically significant spectral peak from wavelet analysis in Sahel rainfall, while Janicot et al. (2010) asserts that the 25-90 day mode is important for producing enhanced or suppressed convection periods on a broader range of timescales. In the 2006 African Monsoon Multidisciplinary Analysis (AMMA) campaign, Janicot et al. (2008) determined that large-scale intraseasonal events had a role in the onset of the west African monsoon. Matthews (2004) documented strong 30-90 day variability of Atlantic trade winds, and suggests a potential link to the reversal of the IPV gradient over sub-Saharan Africa. Via a modeling study, Thorncroft and Rowell

(1998) support the notion that AEW activity is dependent on the intraseasonal variability of the IPV gradient.

Several studies have cited negative OLR anomalies initiating in a region to the northeast of Lake Chad and propagating downstream toward west Africa (Janicot et al. 2010; Thorncroft et al. 2008; Matthews 2004). However, these studies do not investigate why OLR anomalies exist upstream or the relationship between convection and AEW activity on 30-90 day timescales. On intraseasonal timescales, positive convective anomalies grow over Africa and occur at the same time that positive convective anomalies occur in the Indian Ocean in association with the MJO (Janicot et al. 2009; Janicot et al. 2010). Matthews (2004) utilized NCEP reanalysis and satellite data to show that convective anomalies over Africa may be initiated via a delayed remote response to reduced convection over the Indo-Pacific warm pool. The reduced convection forces a "negative" anomalous equatorial Kelvin and Rossby wave response that meets over Africa twenty days later, along with the onset of convection (Janicot et al. 2009). Specifically, Matthews (2004) hypothesizes that the "negative" equatorial wave response destabilizes the troposphere through anomalous deep ascent that produces negative mid-tropospheric temperature anomalies and triggers anomalous deep convection over tropical north Africa (Janicot et al. 2010). The convective response due to the equatorial Rossby wave is located at about 10°N. The equatorial Kelvin wave forces a convective response closer to the equator, and also increases the monsoon flow, available moisture, and cyclonic shear associated with the AEJ (Matthews 2004). Several studies argue that since tropical Africa is dominated by westward propagation, convectively coupled equatorial Rossby waves are the dominant means by which the MJO influences this

region (Janicot et al. 2009, 2010; Lavender and Matthews 2009). The relationship between the MJO and tropical north Africa is likely complicated, with anomalously negative geopotential heights associated with enhanced convection located over northern India that spread into west Africa and enhance westerly moisture advection associated with the west African monsoon (Janicot et al. 2010).

With a strong link between west African monsoon rainfall, AEWs, and Atlantic tropical cyclones, it is reasonable to expect that if the west African monsoon varies on intraseasonal timescales, so will Atlantic tropical cyclones (Maloney and Shaman 2008; Mo 2000; Maloney and Hartmann 2000b). In particular, Maloney and Hartmann (2000b) found significant MJO modulation of tropical cyclones in the Gulf of Mexico and Caribbean Sea, while Mo (2000) discovered significant MJO-related modulation of vertical wind shear west of 60°W in the Atlantic that affected TCs. Maloney and Shaman (2008) documented significant TC variability in the Atlantic main development region that corresponded to 30-90 day fluctuations of the west African summer monsoon. If the MJO significantly modulates fields over tropical north Africa, extensive potential exists for predicting periods of enhanced or suppressed Atlantic TC activity.

1.8. Study Outline

This study aims to identify and explain the MJO teleconnection to the west African monsoon, specifically through the processes that induce convection and AEW variability east of Lake Chad. Section 2 describes the various datasets utilized in this study. The methodology is also described in this section, with information on filtering, compositing, and significance testing. Section 3 analyzes intraseasonal variability over

tropical north Africa using a number of datasets. The analyzed fields include brightness temperature, precipitation, total precipitable water, upper-level air temperature, and various aspects of the flow. Section 4 analyzes the intraseasonal moisture budget to determine the dominant processes that moisten (dry) the troposphere in advance of the MJO wet (dry) phases in this region. Section 5 describes how the eddy kinetic energy budget varies on intraseasonal timescales. Section 6 features a summary and discussion, where the main findings of the thesis are explained.

2. Data and Methodology

2.1. Data

2.1.1. ECMWF Interim Re-Analysis

The European Centre for Medium-Range Weather Forecasts (ECMWF) Interim Reanalysis (ERA-Interim) is the primary dataset utilized in this study. ERA-Interim is a reanalysis of the global atmosphere beginning in 1989 and continuing in real time (Berrisford et al. 2009). The ERA-Interim dataset serves as a bridge between ERA-40 (1957-2002) and the next generation ECMWF extended reanalysis product. While ERA-40 has been used in several important studies, ERA-Interim aimed to improve representation of the hydrological cycle, the stratospheric circulation and the handling of biases and changes in the observing system. Berrisford et al. (2009) assert that the aforementioned objectives have been achieved primarily through model improvements, four-dimensional variational analysis, and revised humidity and bias corrections for satellite data.

The ERA-Interim atmospheric model has higher spatial resolution than ERA-40 and NCEP-II Reanalysis. ERA-Interim features 60 levels in the vertical, ranging from 0.1 hPa to 1000 hPa, and T255 spherical-harmonic representation of basic dynamical fields, which is reduced to a horizontal resolution of 1.5° in the output datasets provided. The atmospheric model is coupled to an ocean-wave model with 1.0° resolution and

ability to resolve 30 wave frequencies and 24 wave directions (Berisford et al. 2009). We use model output with four times daily resolution, or every six hours. A daily average of these 4x daily values is constructed for the fields displayed below. Thus, ERA-Interim allows for detailed study of the troposphere and stratosphere at any location on the planet over a 21-year (and growing) period.

The higher horizontal resolution of ERA-Interim is of higher importance in the tropics, where the distance between each degree of latitude is greatest on the global Gaussian grid. ERA-Interim is an improvement over ERA-40 and NCEP-II Reanalysis at resolving smaller-scale features and topographic interaction. In northern Africa, a region of focus in this study, the increased resolution results in better depiction of topographical variances, such as the Darfur Mountains, Tibesti Mountains and the Ethiopian highlands, which can have significant implications for convection, in particular generation of AEWs over the highlands of Africa. The improved hydrologic cycle of the ERA-Interim product also provides more confidence in the results derived below.

2.1.2. NCEP/DOE AMIP-II Reanalysis

The National Centers for Environmental Prediction (NCEP)/Department of Energy (DOE) Atmospheric Model Intercomparison Project 2 (AMIP-II) Reanalysis (hereon referred to as NCEP-II) is a widely utilized dataset that is occasionally used to test the robustness of results obtained in this study. The NCEP-II dataset was developed to correct human error in the NCEP-I reanalysis (Kanamitsu et al. 2002). Despite the improvement, Kanamitsu et al. (2002) assert that NCEP-II is not part of the next generation of renanalyses (i.e. ERA-Interim) due to the absence of higher vertical and

horizontal resolution, assimilation of radiances and rainfall and the use of SSM/I data. Of particular importance is the fact that NCEP-II improves upon soil wetness, which could improve surface fluxes associated with the west African monsoon. However, this dataset also smooths orography, which likely hinders the effect of smaller mountain ranges in north Africa on convection.

The dataset currently spans 1979 to 2008, providing 30 years of data to make meaningful composites. The spatial resolution is lower than ERA-Interim, with T62 representation that is degraded to 2.5° horizontal resolution and 28 vertical levels in the output dataset provided. In the vertical, NCEP-II offers less than half of vertical levels of ERA-Interim, and features like the African easterly jet (AEJ), which has a peak near 650 hPa, must be interpolated from the 600 hPa and 700 hPa levels. Although the vertical resolution of NCEP-II is not ideal, it is sufficient for this study.

2.1.3. CLAUS Brightness Temperature

The Cloud Archive User Service (CLAUS) is a project coordinated, maintained and updated by the National Environment Research Council (NERC) Environmental Systems Science Centre (ESSC). The British Atmospheric Data Centre (BADC) provides access to CLAUS data. Presently, the CLAUS archive is produced from 10 µm thermal Infra-red window (channel 2) data to create a uniform grid of brightness temperature values (Robinson and Hodges 2005). The data set is available from July 1983 to December 2006. The resulting horizontal and temporal resolutions are 0.5° and three hours, respectively. CLAUS brightness temperature data was chosen over NOAA outgoing longwave radiation (OLR) because of the higher spatial and temporal

resolutions. For this study, CLAUS brightness temperature is utilized as a proxy for deep convection since colder brightness temperatures correspond to higher cloud tops.

2.1.4. GPCP

The Global Precipitation Climatology Project (GPCP) is maintained by the National Aeronautics and Space Administration (NASA) and provides daily rainfall for each 1° on the globe from October 1996 to August 2009. In order to derive rainfall estimates, GPCP incorporates a blend of the six best quasi-global datasets (Huffman et al. 2001). In particular, these datasets are: 1) Special Sensor Microwave/Imager (SSM/I; fractional occurrence of precipitation), 2) GPCP Version 2.1 Satellite-Gauge (monthly accumulation of precipitation), 3) geosynchronous orbit IR brightness temperature histograms, 4) low-orbit IR GOES Precipitation Index (GPI), 5) Television and Infrared Operation Satellite (TIROS) Operational Vertical Sounder (TOVS), and 6) Atmospheric Infrared Sounder (AIRS). The use of high resolution precipitation data over west Africa is important to account for topographical variances and the sharp moisture gradient between the Gulf of Guinea and the Sahara. Additionally, GPCP provides an alternative to ERA-Interim precipitation and provides a precipitation dataset to supplement the measure of convection provided by CLAUS, which improves the robustness of the study.

2.1.5. NVAP

The NASA Water Vapor Project (NVAP) dataset is a multi-year (1988-1999) total column water vapor dataset. The total column water vapor is determined through a combination of radiosonde observations, as well as the Television and Infrared

Operational Satellite (TIROS) Operational Vertical Sounder (TOVS) and SSM/I data sets. With 1° horizontal resolution, NVAP provides an alternative to ERA-Interim total column water vapor, which has stronger dependence on parameterized physics. However, the latter is used to calculate the moisture budget given the better vertical resolution of the water vapor data and the consistency with the other moisture budget terms provided by the reanalysis model.

2.2. Methodology

2.2.1. Time Filtering

In order to study how certain fields are modulated by the MJO, data is filtered to intraseasonal timescales. In particular, intraseasonal anomalies are produced via a linear non-recursive digital bandpass filter with half-power points at 30 and 90 days. The 30-90 day bandpass filter is effective at retaining nearly full frequency power at 40-50 day timescales, or the dominant timescale of the MJO. The bandpass filter is comprised of a high-pass 90-day filter and a low-pass 30-day filter. Each of the two filters is constructed with one-hundred nineteen weights, and thus one-hundred eighteen values are lost from each end of the time series after applying the bandpass filter. The data loss is negligible for this study given that it primarily occurs outside of the boreal summer, which is the season of interest.

2.2.2. Spatial Filtering

Some fields are spatially-filtered based on zonal wavenumber as a means to analyze the potential modulation of tropical north African fields via Kelvin- and Rossby-

type waves. These include intraseasonal Kelvin waves emitted by MJO heating in the Indo-Pacific warm pool, as well as Rossby waves emitted by the MJO heating anomalies in the Indian Ocean. Kelvin and Rossby waves are represented by low wavenumbers, or larger spatial scales. In order to capture these waves, as well as others with similar characteristics, data is filtered to include wavenumbers 0 to 10 for eastward propagating disturbances and wavenumbers -1 to -10 for westward propagating disturbances. Zonal wavenumber zero represents the zonal mean and is included with eastward propagating disturbances to capture the potentially fast propagation of Kelvin waves and their modulation of the tropical zonal mean (e.g. Bantzer and Wallace 1996). Considering that lower wavenumbers correspond to larger spatial scales, the combination of eastward and westward zonal wavenumber filtering performed in this study, which spans from zonal wavenumber -10 to 10, may aid in understanding the relationship between large-scale anomalies and total anomalies. Although methods exist to filter the time-frequency domain to extract only Kelvin or Rossby waves, it was important to include all features with MJO-like timescales. All data that is spatially-filtered is temporally-filtered as well. However, in some cases, such as with eddy kinetic energy, the spatial and temporal filtering methods are modified, as discussed in Section 5.

2.2.3. MJO Composites

Composites that describe the evolution of an MJO lifecycle were constructed using an index derived from empirical orthogonal functions (EOFs). Multivariate EOF analysis was performed on 850 hPa zonal wind, 200 hPa zonal wind and brightness temperature data. All data was 30-90 day bandpass filtered, meridionally-averaged from

15°S-15°N, and had the annual and seasonal cycles removed. The first two EOFs were retained. The first EOF is in quadrature with the corresponding second EOF. Figure 2.1 shows the first and second EOFs for the aforementioned data, which together explain 55.15% of the total combined variance. For each variable, the first EOF generally peaks ten days before and 90° to the west of the second EOF, representing eastward propagation. Wheeler and Hendon (2004; hereon WH04) found the same result, with the first EOF leading the second EOF. From the principle components (PCs) of the two leading EOFs, an index was constructed that features daily information about MJO amplitude and phase. The amplitude and phase are calculated by (2.1) and (2.2), using the same method as WH04. Sign information for the PCs is retained in the construction of the phase.

$$Amplitude = \sqrt{PC1^2 + PC2^2} \tag{2.1}$$

$$Phase = \arctan\left(\frac{PC1}{PC2}\right) \tag{2.2}$$

Although the methods are consistent, WH04 utilize OLR, whereas this study incorporates brightness temperature. The use of brightness temperature was motivated by the desire to create a slightly different index to test the robustness of results and the fact that CLAUS has higher spatial resolution, which is manifested as a greater number of latitudinal data points between 15°S and 15°N. This higher resolution is important in the composite maps below. The results are qualitatively similar to WH04, due to the dominance of the MJO at 30-90 day timescales. The phase and amplitude for the first three years of the index are shown in Figure 2.2. The MJO may be split into eight phases of equal angular extent, with each phase representing enhanced MJO activity at a particular part of the world. With one MJO cycle taking approximately 40 days, each phase represents

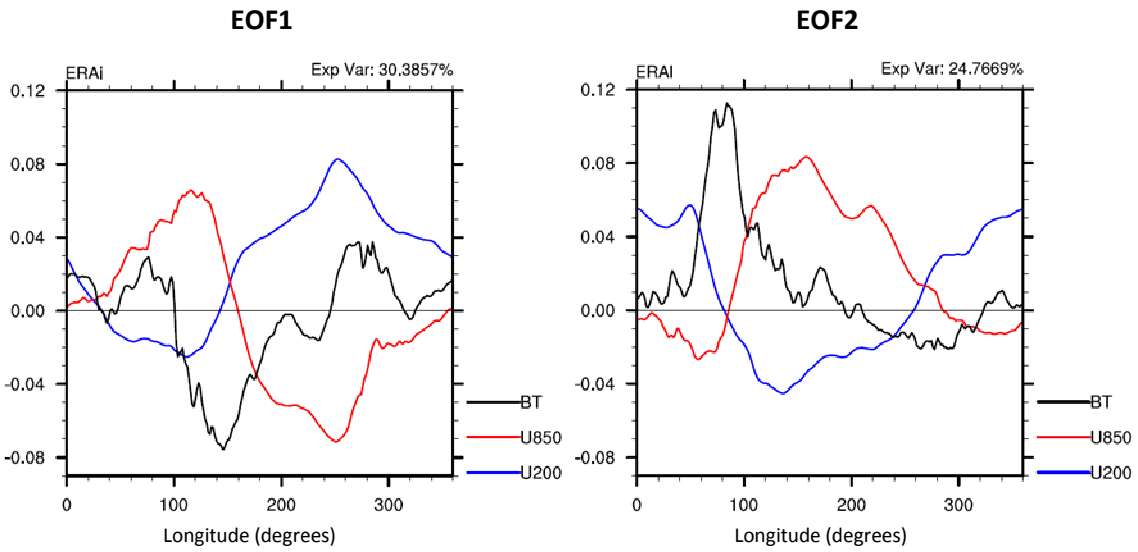

Figure 2.1. EOF1 and EOF2 of the equatorial-averaged (15°S – 15°N), 30-90 day bandpass filtered (i) CLAUS brightness temperature, (ii) ERAi 850 hPa zonal wind and (iii) ERAi 200 hPa zonal wind.

approximately 5 days of that cycle. The phase index assigns each day to be within a particular phase of the MJO. The amplitude index determines the strength of the MJO on each individual day. In accordance with WH04, only days with amplitude over 1.0 are included in composites below in order to eliminate any potential biases that weaker MJO events may create. As a test of the viability of the MJO index described above, global composites of brightness temperature and low-level zonal wind produced with this index are compared with OLR and zonal wind composites from WH04's index.

Figure 2.3 shows an eight-phase MJO composite of 30-90 day bandpass-filtered anomalous brightness temperature (CLAUS) and 30-90 day anomalous 850 hPa zonal wind (ERAi) for significant MJO events during boreal summer (June to September) from 1989-2005. Importantly, the data record includes at least 151 significant MJO days for each phase, which means the composites include enough unique days to produce reliable averages. Significance testing in several fields below will verify this. When NCEP-II zonal winds are used instead of ERAi (not shown) zonal winds, the results are very

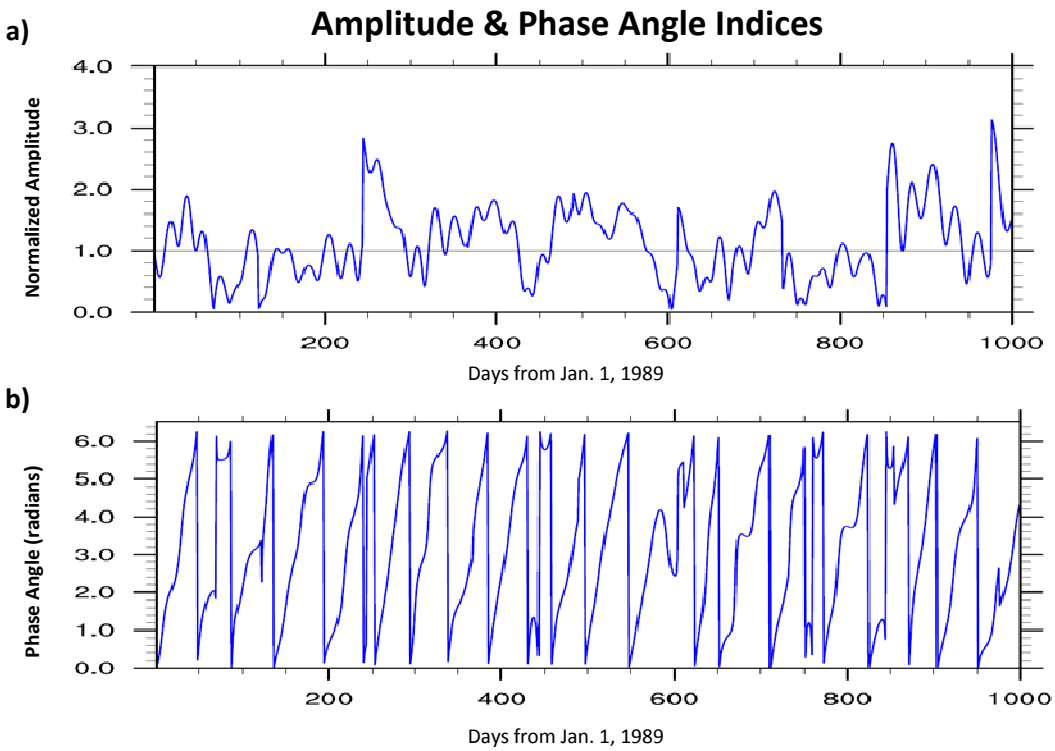

Figure 2.2. 1000-day time series for a) the amplitude index and b) the phase angle index. Amplitudes values over 1.0 (solid black) are indicative of significant MJO events.

consistent, providing evidence that the pattern shown in Figure 2.3 is robust across multiple reanalyses.

Phase 1 is defined by anomalously low brightness temperature and low-level anomalous westerlies in the central Indian Ocean. Low brightness temperature is indicative of high clouds tops, and, thus, deep convection associated with the MJO. The low-level anomalous westerlies are located on the western side of the convective envelope, which is consistent with previous observations (WH04). By Phase 4, convection has spread eastward to the west Pacific, which is consistent with the eastward propagation of the MJO, and north to India, indicative of the relationship that the MJO has with the Indian monsoon during boreal summer. In particular, the MJO is responsible for active and break periods of the Indian summer monsoon. Phase 4 also features low-

level anomalous westerlies throughout the entire Indian Ocean, with a maximum located under the western half of the convection. In Phase 6, much of the convective signal has moved north or damped out by the dateline and low-level anomalous westerlies dominate the tropical Pacific. Phase 6 also marks a distinct increase in brightness temperatures and a transition to low-level anomalous easterlies over the Indian Ocean, indicative of dry conditions. By Phase 8, the dry signal has propagated northeast and low-level anomalous easterlies have spread across much of the Indian Ocean and maritime continent. In the eastern Indian Ocean, weak negative brightness temperatures anomalies return, marking the start of a new MJO cycle.

The relationship of African anomalies to the global MJO evolution may be analyzed in Figure 2.3. In particular, negative brightness temperature and low-level westerly zonal wind anomalies are evident in tropical west Africa and the tropical eastern Atlantic during Phase 1. The increase in deep convection over tropical Africa in Phase 1 is the consequence of enhanced west African monsoon flow and Atlantic ITCZ convection. Thus, convection anomalies maximize over Africa as MJO convection initiates in the Indian Ocean. Importantly, the negative brightness temperature anomalies in the Indian Ocean and over tropical Africa are separated by low amplitude anomalies in east Africa, which indicates a complex relationship. Conversely, positive brightness temperature and low-level easterly zonal wind anomalies maximize over tropical west Africa and the eastern Atlantic in Phase 5, which coincides with the suppression of MJO convection in the Indian Ocean. Low-level easterly anomalies indicate a suppression of west African monsoon flow, which supports the decrease in convection.

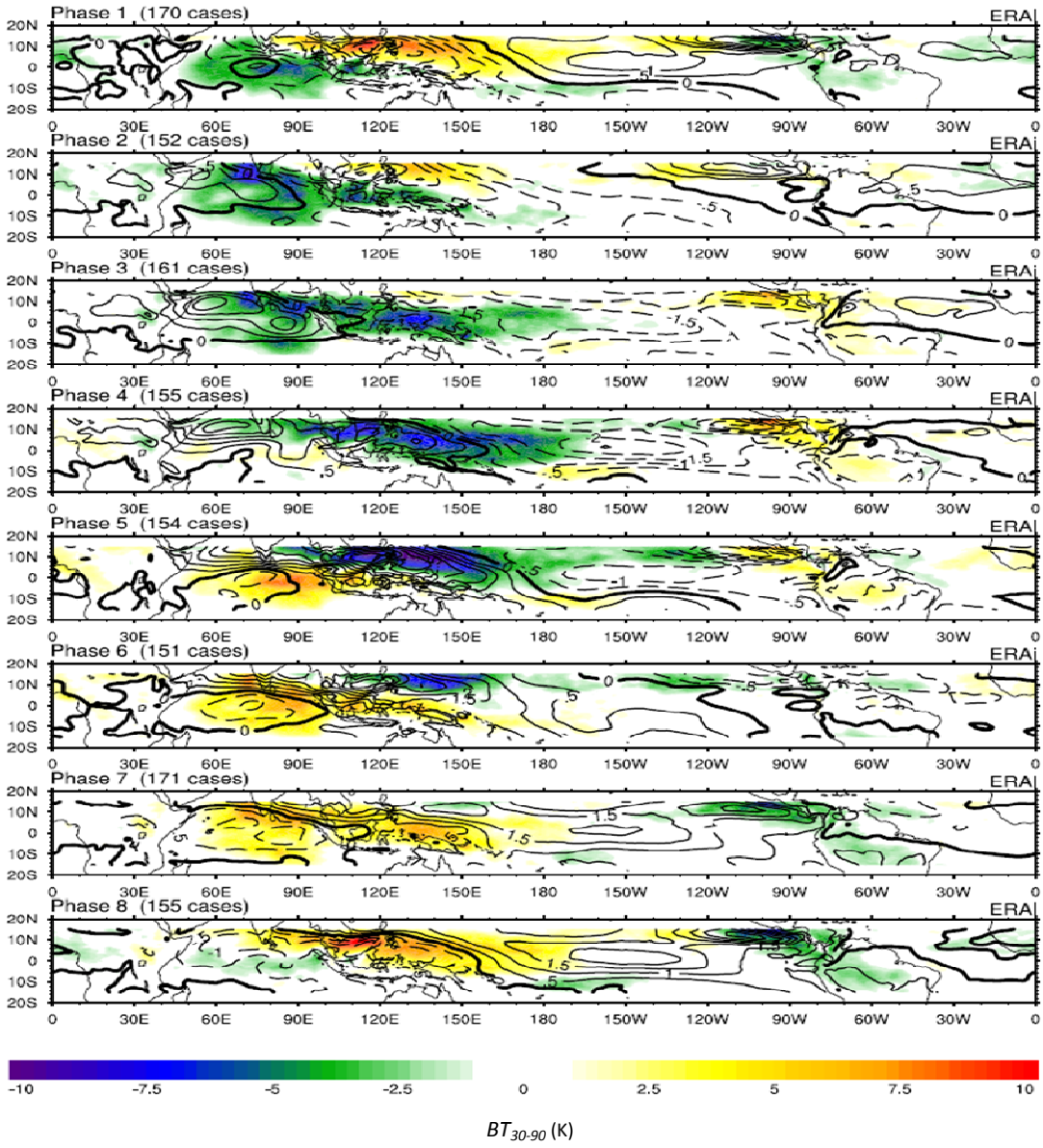

Figure 2.3. MJO phase composites of CLAUS anomalous 30-90 day brightness temperature (shading) and 30-90 day 850 hPa zonal wind anomalies for June-September. The scale for brightness temperature is given by the color bar. The contour interval for the zonal wind is 0.5 m s^{-1}.

Since this study is primarily concerned with intraseasonal variability over tropical north Africa, this region will be highlighted for the remainder of this analysis. Brightness temperature anomalies over tropical Africa are on the order of 2.5 K, which is about a quarter of the maximum amplitudes observed in the Indo-Pacific region associated with the MJO. Regardless, intraseasonal brightness temperature variability over tropical north

Africa will be shown to be significant below and requires more analysis. Also, this brightness temperature variability is associated with fluctuations in TC activity in the Atlantic. Further inspection of tropical north African variability on MJO timescales may reveal a link between AEW initiation and/or maintenance and the MJO.

2.2.4. Significance Testing

It is important to note that low amplitude variations in brightness temperature and zonal wind exist over north Africa relative to other regions of the tropics, providing a first glimpse into how atmospheric conditions over northern Africa vary on MJO timescales. Because of the relatively low amplitude signal over Africa, Student's *t*-test at the 95% confidence interval is performed in many of the analyses described below to discern whether or not the low amplitude anomalies over northern Africa are significant. The 95% confidence limits are computed by

$$\mu = \bar{x} \pm \frac{t_c \sigma}{\sqrt{\nu - 1}}, \tag{2.3}$$

where $\bar{x}$ is the composite value at a particular spatial point for a given phase, t_c represents the critical value of the *t*-statistic given the degrees of freedom and the confidence interval desired, σ is the sample standard deviation at a particular spatial point and phase, and ν describes the degrees of freedom. The degrees are freedom are calculated by dividing the total number of days in an MJO phase bin by the characteristic number of days that the MJO exists in a given MJO phase, which is typically 5. This value also represents the fewest possible number of unique MJO events for a single phase and produces a conservative value for degrees of freedom. Here, the average number of days per MJO phase is 158.625, so assuming that one MJO phase represents 5 days, the

degrees of freedom is determined to be 31.725. This value for degrees of freedom is used for all variables described below for consistency. The corresponding critical *t*-statistic value (t_c) for calculating 95% confidence intervals is 2.04. If the confidence interval does not include the June-September mean for a particular spatial point, then that value is considered to be significant. In the case where the composite value $\bar{x}$ is an anomaly, as is the case with many fields analyzed in this study, then the value is significant if the confidence interval does not include zero.

3. Convective Variability of Tropical Northern Africa on MJO Timescales

3.1. Brightness Temperature

In order to investigate how AEWs are modulated on intraseasonal timescales, the convective pattern over tropical northern Africa is analyzed with the goal of identifying MJO phases with anomalously high or low CLAUS brightness temperature. While outgoing longwave radiation (OLR) is utilized in several studies as a proxy for convection (Wheeler and Kiladis 1999; Wheeler and Hendon 2004; Wheeler et al. 2000; Knutson and Weickmann 1987), brightness temperature serves the same purpose. The CLAUS brightness temperature dataset features a higher resolution (0.5°) than the NOAA OLR (2.5°) dataset, which translates into a better representation of convective variability in tropical north Africa, given small-scale, yet important, mountain ranges. The pattern of brightness temperature anomalies over the region provides insight about when convective anomalies are enhanced or suppressed during the eight phase MJO cycle. When brightness temperatures are anomalously low, for example, convection is enhanced. Although AEW activity cannot be directly diagnosed from intraseasonal variations in brightness temperature, this study hypothesizes that enhanced AEW activity is correlated with positive convective anomalies on 30-90 day timescales.

Figure 3.1 shows the anomalous ERAi 30-90 day brightness temperature field for the eight MJO phases as defined by Wheeler and Hendon (2004). As a reminder, composites only use significant days as defined in Section 2.2.3. Since Phase 1

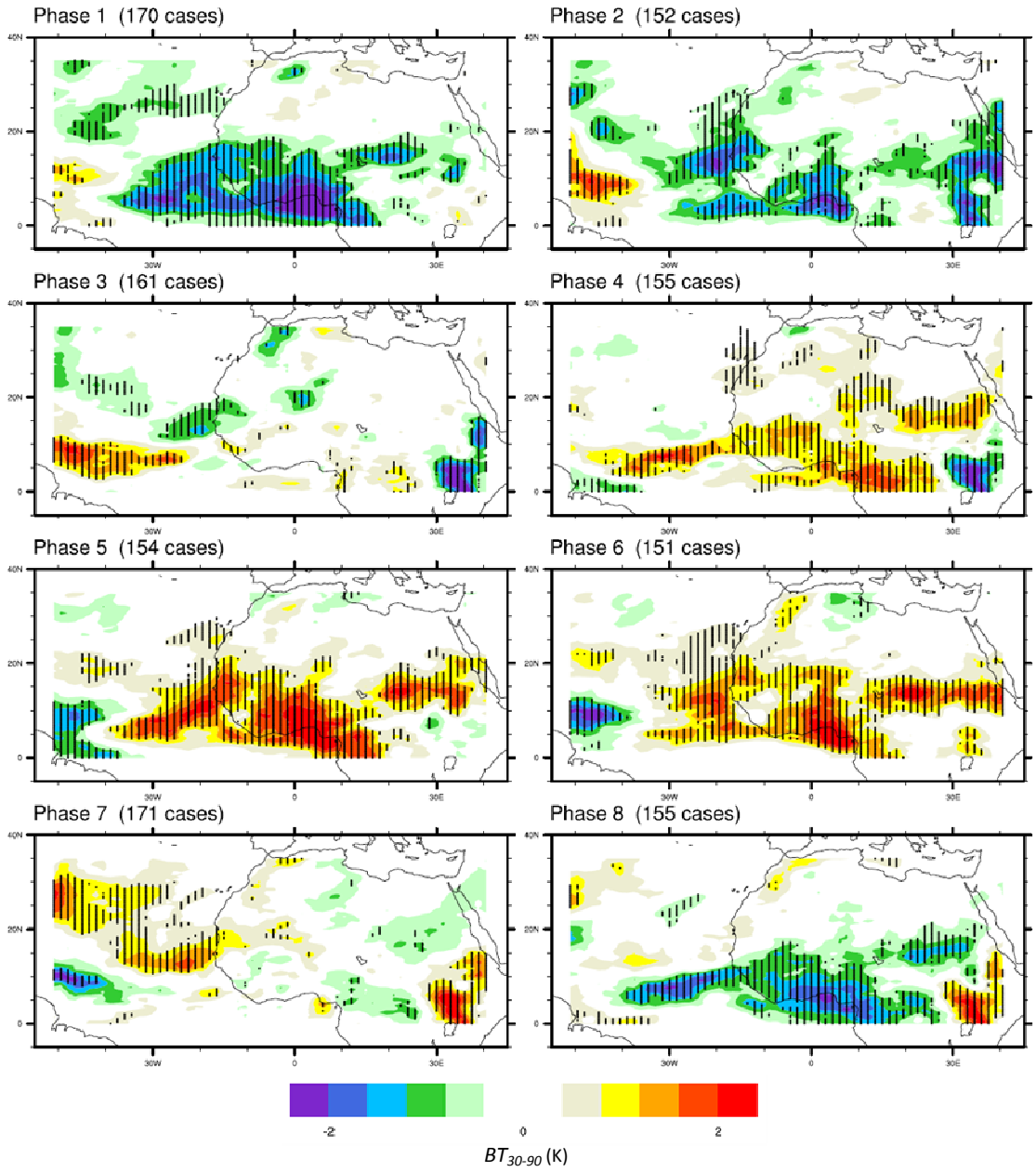

Figure 3.1. MJO phase composites of CLAUS anomalous 30-90 day brightness temperature for June-September. The scale for brightness temperature is given by the color bar. The shading interval is 0.4°K. The vertical lines represent significant anomalies at the 95% confidence interval.

represents the onset of MJO convection in the Indian Ocean, Figure 3.1 reveals that tropical north Africa is convectively active at the same time that the MJO is active in the Indian Ocean (see Figure 2.3). In Phase 1, significant negative 30-90 day brightness temperature anomalies are widespread from the equator to ~20°N and from 35°W to

35°E. This period is also associated with enhanced convective activity linked with AEWs (Section 5 below). Due to this pattern, Phase 1 will be referred to as the "wet" phase of the MJO over tropical north Africa. The convectively enhanced region, which includes tropical west Africa and the Gulf of Guinea, features brightness temperature anomalies less than -2 K. Importantly, a region in the vicinity of the Darfur Mountains (15°N, 23°E) exhibits negative brightness temperature anomalies at Phase 1. Significant negative brightness temperature anomalies first appear in this region in Phase 7. These results suggest that anomalous upstream latent heating may help initiate periods of enhanced AEW activity, as in Thorncroft et al. (2008). Additionally, during Phase 1, significant negative brightness temperature anomalies are located in the northeast Atlantic, including latitudes from 18°N to 30°N and longitudes from 47°W to 15°W. Although the northeast Atlantic exhibits significant anomalies, the region will not be emphasized here due to the lack of correspondence to AEW initiation.

Phase 3, which lags Phase 1 by about 10 days, serves as a transition from the MJO convective phase to the dry phase, as evidenced by the lack of widespread significant brightness temperature anomalies over northern Africa. Significant negative brightness temperature anomalies are located just off the west African coast, in a SE-NW line extending from approximately 15°N, 15°W to 25°N, 45°W. These significant anomalies are associated with enhanced convective activity associated with AEWs that have propagated into the Atlantic. Additionally, suppressed convection in the intertropical convergence zone (ITCZ) extends from 5-10°N and 20-50°W.

Phase 5 is dominated by significant positive brightness temperature anomalies over tropical north Africa and coincides with a suppression of MJO convection in the

Indian Ocean. The pattern of positive brightness temperature anomalies in Phase 5 matches up almost perfectly with the negative brightness temperature anomalies in Phase 1, and magnitudes are in excess of 2 K. For that reason, Phase 5 will be referred to as the "dry" phase of the MJO over tropical north Africa. Positive 30-90 day brightness temperature anomalies are prevalent from the equator to 20°N and 40°E to 40°W. In the opposite sense of Phase 1, the suppression of convection in tropical north Africa may be partly attributed to the suppression of upstream convection over the Darfur region near 15°N, 20°E, and, thus, a lack of mesoscale system generation in this region. This suppression of convection in the Darfur region commences during Phase 4.

Phase 7 is almost a mirror image of Phase 3. In Phase 7, tropical west Africa is mostly void of significant brightness temperature anomalies. The suppressed area of convection has propagated out into the Atlantic, and the ITCZ (5-10°N; 20-50°W) is characterized by enhanced convection. As mentioned above, significant negative brightness temperature anomalies exist upstream of the wave development region, providing evidence of precursor disturbances near the entrance of the AEJ before the onset of convection across tropical north Africa in Phase 1. Phase 8 provides a more convincing picture of significant convection upstream, with more significant negative brightness temperature anomalies populating the region near the Darfur Mountains and Ethiopian highlands.

3.1.1. Convective Averaging Boxes

As a supplement to the MJO phase composites, Phase 1 of the 30-90 day, June-September brightness temperature anomalies (Figure 3.1) is utilized to identify three

regions of local convective maxima. Line plots will be produced below to show how the average value of several variables in each region varies as a function of MJO phase. The three regions are oriented more or less in the zonal direction in order to analyze downstream propagation. Figure 3.2 shows the three regions of interest. The first region, marked (a) in Figure 3.2, is located near the entrance to the AEJ and includes the Darfur Mountains and the northern Ethiopian highlands (see Figure 1.4). This region is important for detecting upstream precursor disturbances, and, as a result, is called the "trigger region". The trigger region is bounded by the 10.5°N and 24°N latitude lines and the 16.5°E and 37.5°E longitude lines. The (b) region, which is nicknamed the "land region", incorporates a local minimum of brightness temperature over tropical west Africa and represents the AEW development region. The land region is situated such that it measures how fields vary as a function of MJO phase where AEW growth is often maximized. The land region is bounded by the 4.5°N and 18°N latitude lines and the 15°W and 11°E longitude lines. The (c) region, or the "ocean region", includes the tropical east Atlantic and measures the intraseasonal variability of fields that may reflect offshore AEW activity. The ocean region is enclosed by the 3°N and 15°N latitude lines and by the 36°W and 13.5°W longitude lines. The ocean and land regions slightly overlap near the west Africa coast due to the idealized rectangular structure of the averaging boxes. Since the African coast is oriented southeast to northwest, the slight overlap of these two regions was a compromise. Together, the line plots from each of these regions can provide more convincing evidence about whether or not terms like total precipitable water peak in the trigger region before peaking in the land and ocean regions.

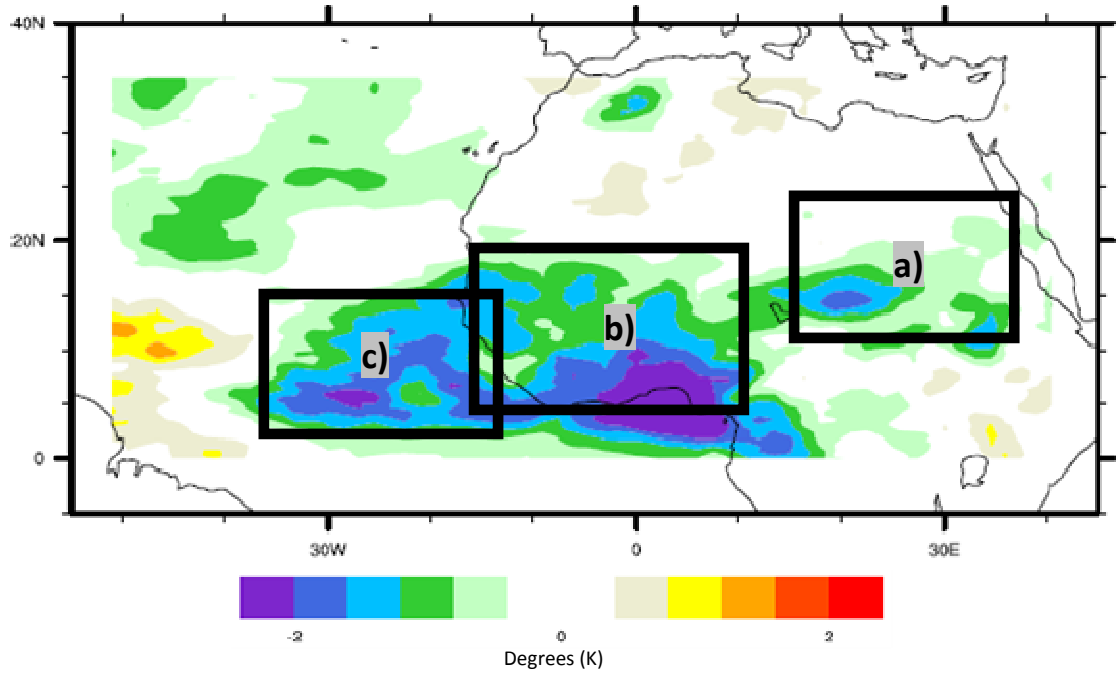

Figure 3.2. Phase 1 of the anomalous 30-90 day brightness temperature (from Figure 3.1). Three boxes are chosen based on convective activity. The regions are: a) trigger region, b) land region, and c) ocean region.

3.2. Precipitation

Since deep convection variability, as diagnosed by brightness temperature, is associated with significant variations in rainfall events, examination of the precipitation field is an important complementary to the analysis of convective activity over tropical north Africa. The boreal mean precipitation reveals critical basic state information about tropical north Africa and the east Atlantic, including the locations of climatological precipitation maxima. Importantly, plotting the boreal mean provides an opportunity to compare the GPCP and ERAi precipitation datasets, which is important because ERAi moisture fields will be used later to diagnose moisture budget terms. As evidenced by Figure 3.3, three precipitation maxima exist across tropical north Africa and the tropical east Atlantic. The maxima reside within the east Atlantic ITCZ, the Gulf of Guinea, and in the vicinity of the Ethiopian Highlands. Despite similarities in rainfall pattern, the

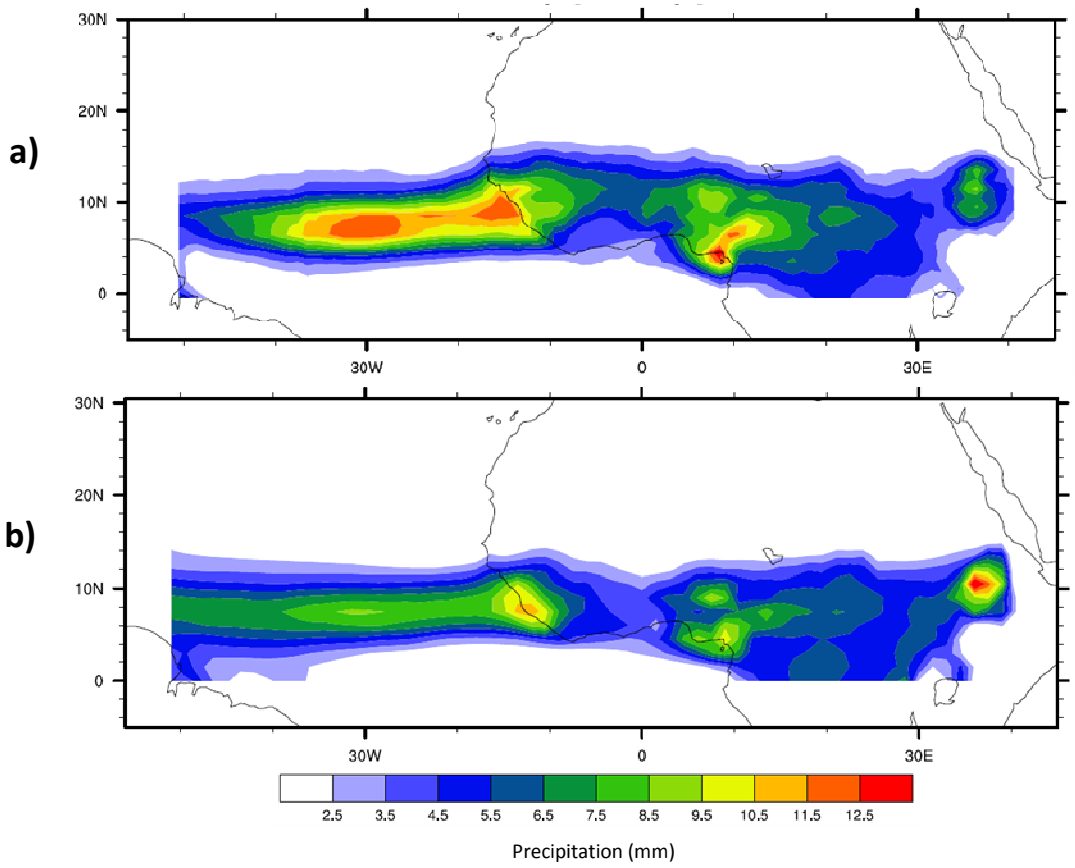

Figure 3.3. June-September mean precipitation for a) GPCP and b) ERAi. Units are millimeters. The shading is given by the color bar and the contour interval is 1 mm day^{-1}.

GPCP and ERAi precipitation datasets produce vastly different amplitudes, with the GPCP values often doubling those from ERAi. Some of this difference may be a manifestation of the disparity in horizontal resolution between the two precipitation datasets. Although GPCP will be analyzed on intraseasonal timescales in this section, ERAi precipitation will be included in the moisture budget analysis in Section 4. This choice is made for consistency with other terms in the moisture budget, which are also created with ERAi datasets. Additionally, it is unknown how trustworthy GPCP is over land, although model-derived precipitation from ERAi may not present much of an improvement.

MJO phase composites of 30-90 day GPCP precipitation anomalies are created to test the robustness of the CLAUS brightness temperature results in Section 3.1. Overall, the results in Figure 3.4 support the brightness temperature anomalies displayed in Figure 3.1. Phase 1 depicts significant and positive rainfall anomalies on the order of 0.9 mm day^{-1} in essentially the same location as the negative brightness temperature anomalies (Figure 3.1). The rainfall maximum extends across tropical west Africa and the tropical east Atlantic. Generally, the anomalies are positive and significant in the trigger region, which provides some evidence of upstream convection initiation. Significant and positive precipitation anomalies first appear in Phase 7. Rainfall anomalies are significant at the 95% confidence interval over the Sahara, but these anomalies will be ignored due to the dry nature of this region and low amplitude of precipitation anomalies.

Phases 2-4 illustrate a transition from the wet phase to the dry phase, with fewer significant positive/negative rainfall anomalies scattered over tropical west Africa from the equator to 15°N. Positive rainfall anomalies extend throughout the Atlantic north of 15°N and are associated with downstream AEW or tropical cyclone activity. Additionally, anomalously low precipitation is located in the Atlantic ITCZ.

Phase 5 features anomalously low significant rainfall amounts on the order of -0.9 mm day^{-1} extending across tropical west Africa and into the Atlantic. These anomalies match up well with the positive brightness temperature anomalies in Phase 5 of Figure 3.1. Some significant negative rainfall anomalies populate the AEW development region, although the signal here is not as strong as in brightness temperature.

Phases 6-7 represent the transition from anomalously dry to anomalously wet conditions over tropical north Africa. Like Phases 2-4, significant positive/negative

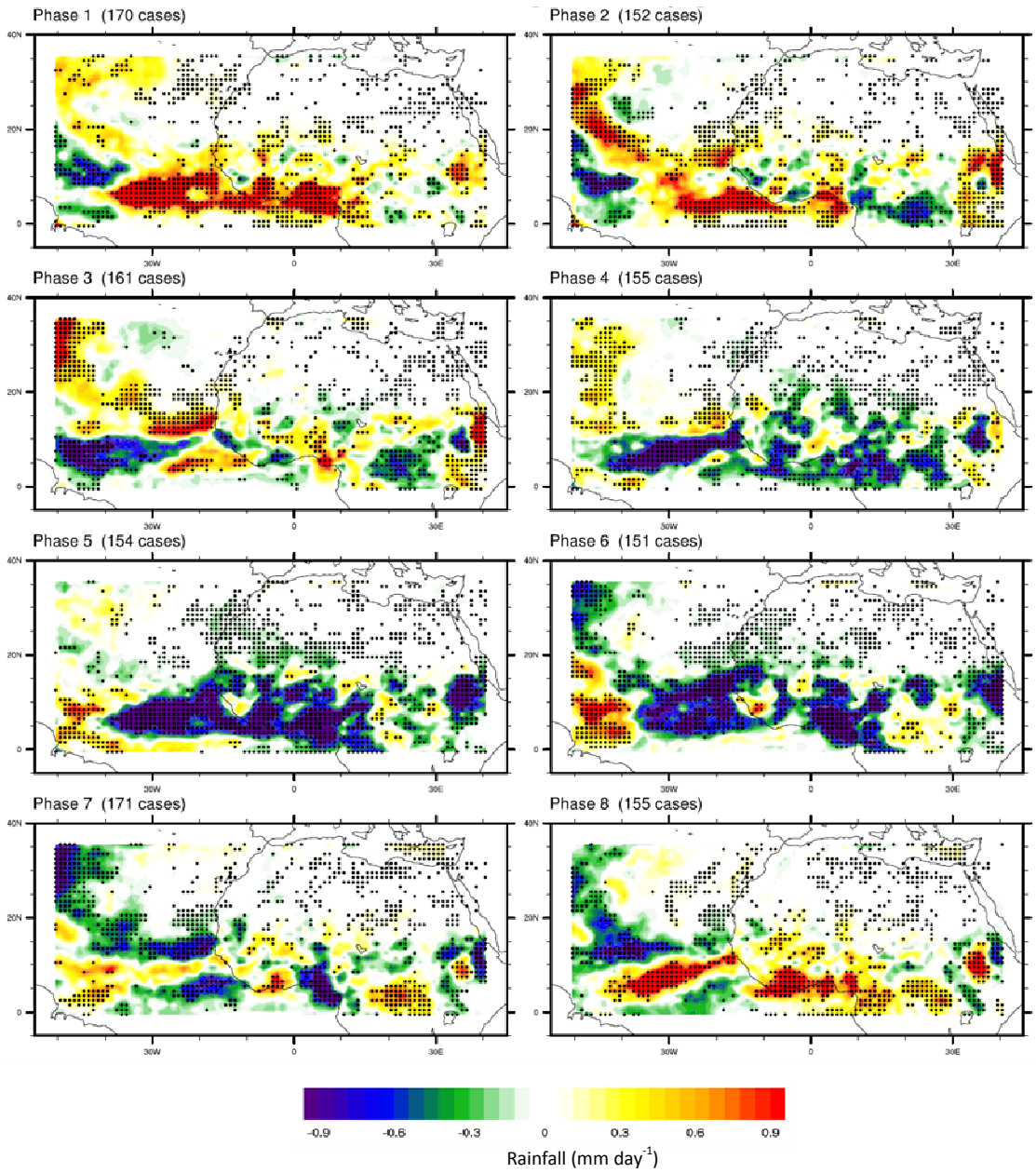

Figure 3.4. MJO phase composites of GPCP anomalous 30-90 day precipitation for June-September. The scale is given by the color bar. The shading interval is 0.06 mm day^{-1}. The dots represent significant data points at the 95% confidence interval.

rainfall anomalies are dispersed throughout tropical west Africa during this time. By Phase 8, positive rainfall anomalies return to north Africa and the eastern Atlantic in advance of the convective maximum in Phase 1. Specifically, anomalously high precipitation is located within the eastern Atlantic ITCZ, on a SW-NE line from (5°N, 40°W) to (12°N, 15°W), and along the African coast in the Gulf of Guinea. This pattern

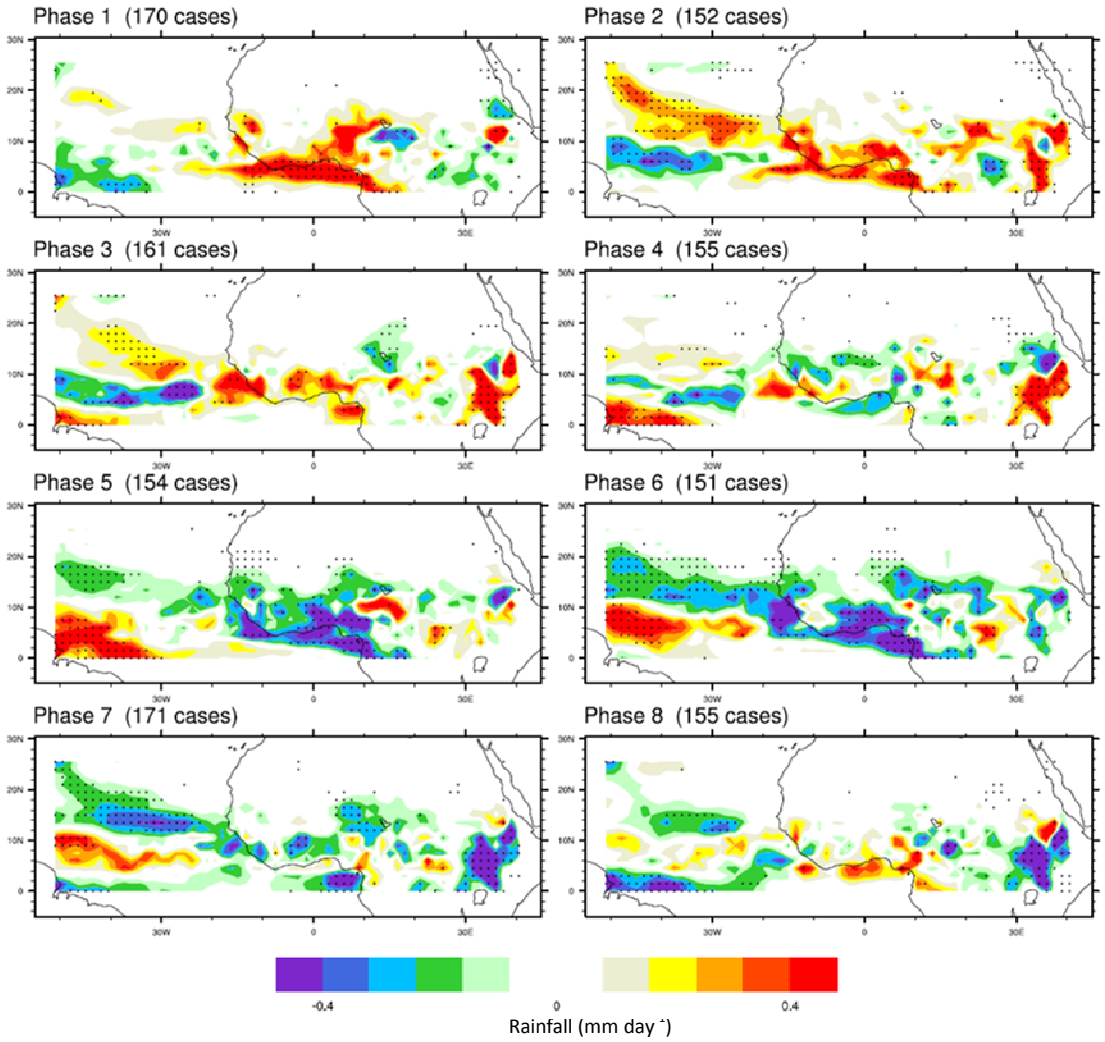

Figure 3.5. The same as Figure 3.4, except for ERAi precipitation. The shading interval is 0.08 mm day^{-1}.

is indicative of enhanced monsoon flow, which may supply the region with moisture to support AEWs. Phase 8 in Figure 3.17 displays a return of onshore flow in the form of anomalous westerlies at the west African coast and weak anomalous southeasterlies near the Guinea coast, which are located in the vicinity of positive precipitation anomalies. Importantly, significant positive rainfall anomalies develop near the trigger region, which indicate that intraseasonal precipitation anomalies there may aid the initiation of AEWs. ERAi precipitation has a similar structure to GPCP on intraseasonal timescales, although

the magnitudes of 30-90 day anomalies are smaller than those observed in GPCP (Figure 3.5).

3.3. Total Precipitable Water

The total precipitable water (TPW), which is equivalent to the mass-weighted vertical integral of specific humidity, provides a measure of the moisture content within an atmospheric column. While high amounts of TPW do not necessarily translate into more precipitation at that particular location, increased moisture within an atmospheric column certainly makes conditions more favorable for deep convection. Bretherton et al. (2004) document the close relationship between column water vapor and tropical precipitation. The boreal summer mean TPW field reveals sharp moisture gradients, as depicted in Figure 3.6. Regions with sharp TPW gradients may allow for significant moisture advection anomalies depending on the direction of the flow (Section 3.5). Figure 3.6a depicts the boreal mean TPW in the NVAP product, while Figure 3.6b shows the ERAi boreal mean TPW. The NVAP product exhibits TPW values above 47 mm in the Atlantic ITCZ and the Gulf of Guinea, with values of 32+ mm over most of tropical north Africa. ERAi TPW maximizes over tropical Africa, in contrast to over the Atlantic for the NVAP product. TPW values of 44+ mm span the eastern Atlantic ITCZ and tropical north Africa in the ERAi product. The TPW maximum at 10°N, 32°E in ERAi is suspicious given how far inland, but evidence of this feature is also seen in Figure 3.6a, with TPW values from NVAP being closer to 38 mm extending into tropical east Africa. Despite the differences, the two datasets generally show the same pattern, justifying the use of the ERAi TPW for further analysis in the moisture budget (Section 4). Importantly, a portion of the sharp TPW gradient is located near the trigger region. If the

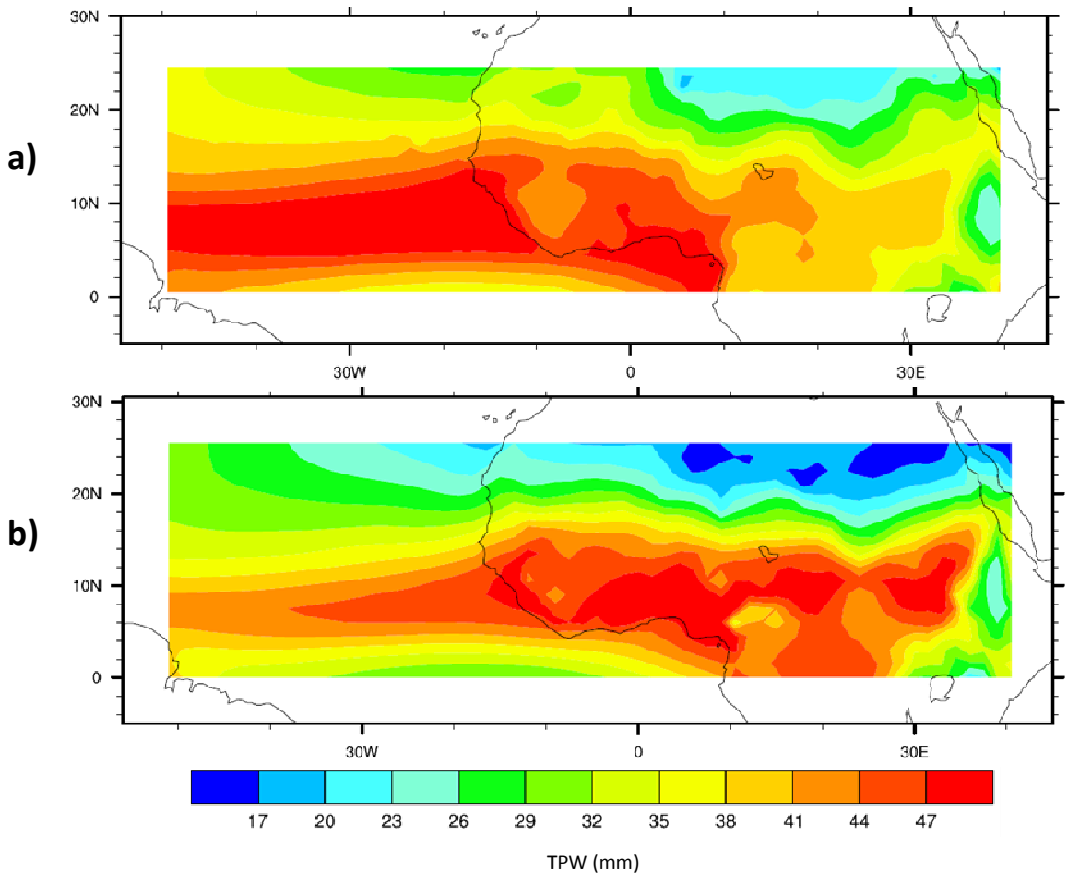

Figure 3.6. June-September mean TPW for a) NVAP and b) ERAi. Units are millimeters. The shading is given by the color bar and the contour interval is 3 mm.

flow is southerly or southwesterly (see Section 3.6), positive moisture advection will occur in the trigger region, supporting the development of precipitation anomalies and upstream precursor disturbances in the Darfur region and Ethiopian highlands.

While the boreal mean TPW field is important, the variability of TPW on MJO timescales reveals whether or not the convective maximum that occurs in Phase 1 is triggered in advance by an increase of moisture in the column, either locally, or in the highlands of east Africa. The ERAi TPW is 30-90 day bandpass filtered to investigate regions of positive or negative TPW anomalies based on MJO phase (Figure 3.7). The 30-90 day NVAP TPW anomalies are displayed in Figure 3.8. The most important

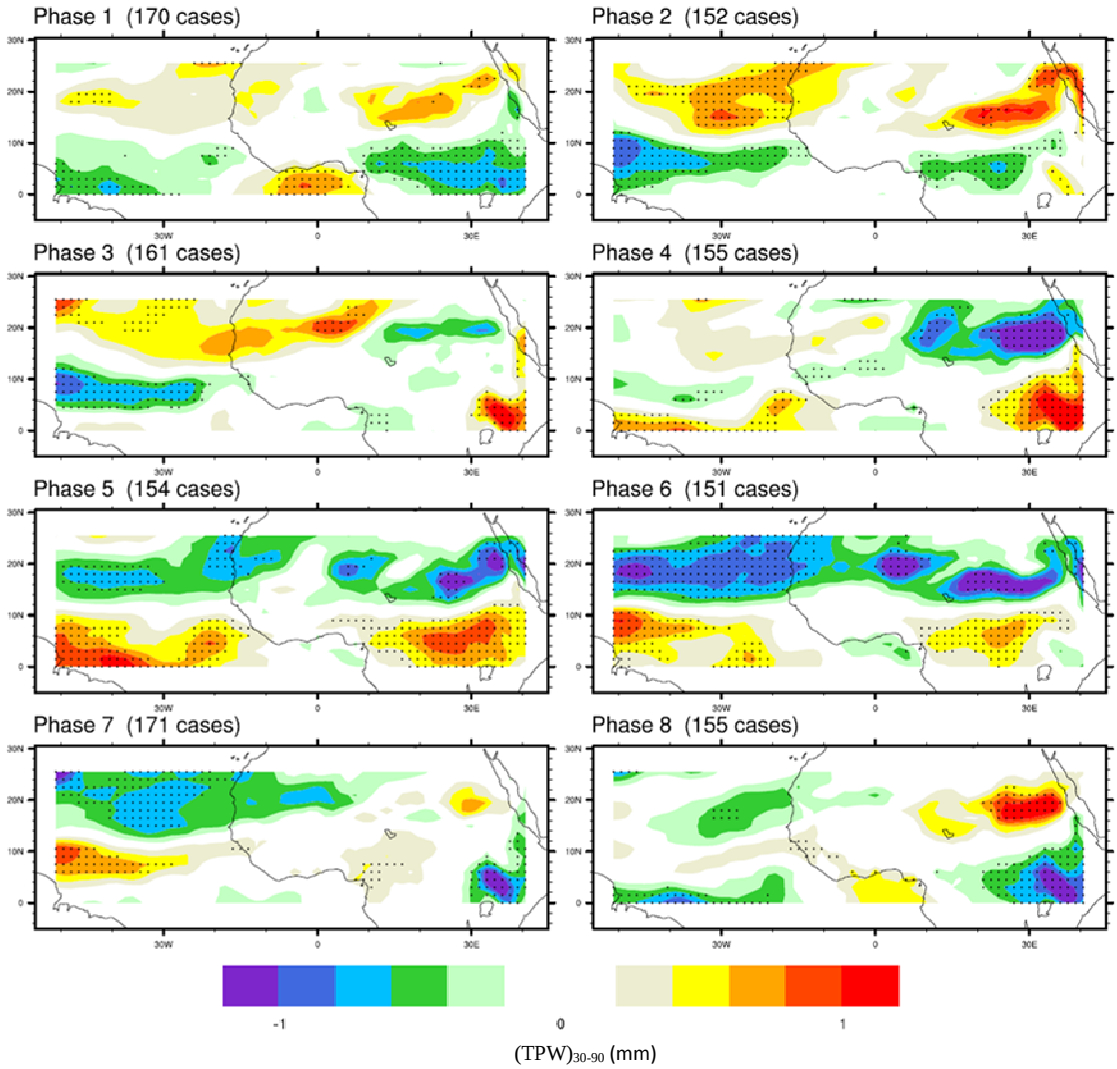

Figure 3.7. MJO phase composites of ERAi anomalous 30-90 day total precipitable water for June-September. The scale is given by the color bar. The shading interval is 0.2 mm. The dots represent significant data points at the 95% confidence interval.

feature is by far the significant positive $(TPW)_{30\text{-}90}$ anomaly around 20°N, 30°E in Phase 8. Evidence of this growing positive anomaly is also present in Phase 7, although the values are not significant at the 95% confidence level. This region also contains development of a negative brightness temperature anomaly in Phases 7-8 (Figure 3.1). Significant positive $(TPW)_{30\text{-}90}$ anomalies within the trigger region support deep convection upstream of the AEW development region in advance of the convective maximum in Phase 1. This upstream feature persists until disappearing in Phase 3, when

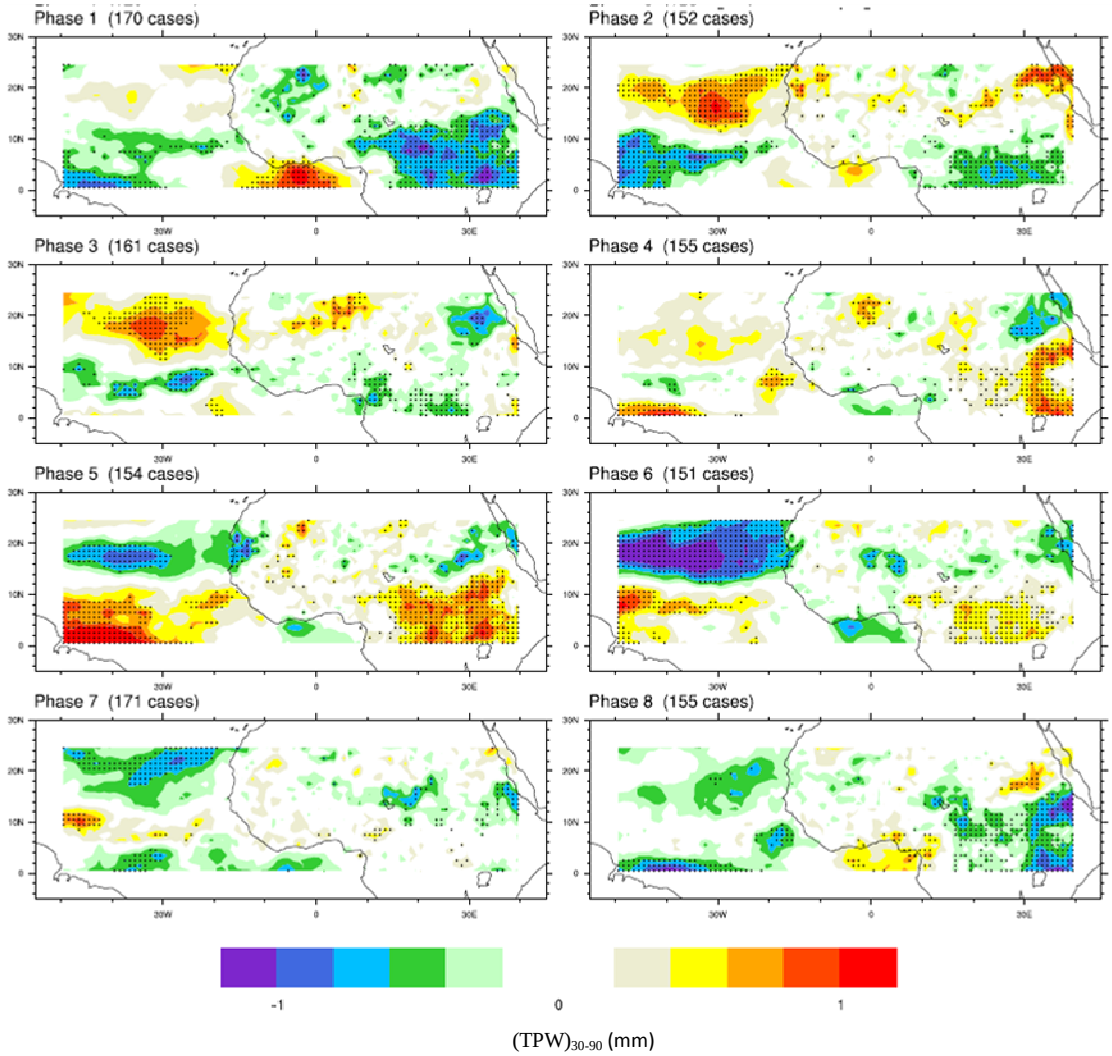

Figure 3.8. The same as Figure 3.7, except using NVAP TPW.

negative brightness temperature anomalies no longer dominate tropical north Africa. Negative moisture anomalies exist in the trigger region in Phase 3-4 in advance of the suppressed phase. The lack of upstream precursors may suppress generation of strong AEWs, which is also reflected in negative convection anomalies that develop in Phases 5 and 6 (Figure 3.1). The AEW development region is void of significant $(TPW)_{30\text{-}90}$ anomalies during most phases, suggesting that tropical west Africa has a consistent and high amount of moisture. Convection in these regions may also be strongly forced by dynamical forcing associated with AEWs (Hall et al. 2006). Boreal mean TPW values in

this region are approximately 44+ mm, indicative of the associated high moisture content. Quite a bit of intraseasonal TPW variability exists over the east Atlantic, with significant, positive $(TPW)_{30\text{-}90}$ anomalies maximizing over the north Atlantic and negative $(TPW)_{30\text{-}90}$ anomalies occurring over the tropical Atlantic in Phases 2 and 3. The opposite is true in Phases 6 and 7.

The 30-90 day ERAi TPW is spatially-filtered to study its relationship with large-scale eastward- or westward-propagating disturbances as a function of MJO phase. Here, large scale refers to wavenumbers between -10 and 10. In particular, large-scale components of the flow, including the influence of equatorial waves, may modulate fields over tropical north Africa and potentially prime the environment for anomalous convection. Figure 3.9(a-c) presents composite $(TPW)_{30\text{-}90}$ anomalies for of the trigger, land and ocean regions as a function of MJO phase for eastward and westward zonal wavenumbers. Due to the difficulty involved in establishing how eastward and westward components of the flow may force TPW anomalies, the relationship between large-scale and total $(TPW)_{30\text{-}90}$ anomalies is analyzed (Figure 3.9d-f). In the trigger region, large-scale $(TPW)_{30\text{-}90}$ and total $(TPW)_{30\text{-}90}$ anomalies are very similar throughout an MJO cycle, especially in Phase 8, which corresponds to increased moisture content in advance of convective maximum. However, total $(TPW)_{30\text{-}90}$ anomalies are positive in Phase 7, which indicates more moisture about ten days in advance of the wet phase. On the other hand, large-scale $(TPW)_{30\text{-}90}$ anomalies are negative in the trigger region during Phase 7. In the land and ocean regions, total $(TPW)_{30\text{-}90}$ anomalies are not well-represented by the large-scale components of the flow. Overall, large-scale $(TPW)_{30\text{-}90}$ anomalies coincide with the total $(TPW)_{30\text{-}90}$ anomalies throughout the trigger region. Eastward- and

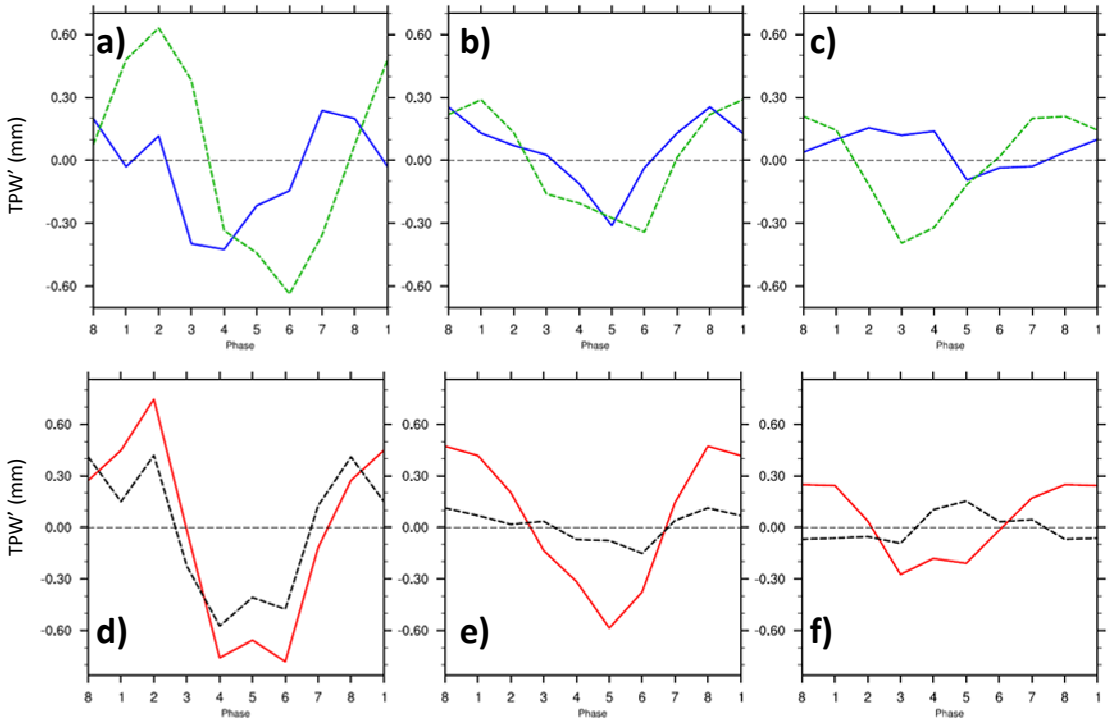

Figure 3.9. Convective box line plots for ERAi 30-90 day TPW anomalies. (a-c) show how TPW anomalies evolve as a function of phase for eastward (green dashed) and westward (solid blue) zonal wavenumbers. (d-f) illustrate how well the 30-90 day anomalies with wavenumbers [-10, 10] (red solid) match up with the total 30-90 day anomalies (black dashed). The trigger box is shown in a) and d). The land box is shown in b) and e). The ocean box is shown in c) and f). Values are TPW anomalies averaged for each phase over the three regions of interest.

westward-propagating disturbances combine to introduce positive $(TPW)_{30\text{-}90}$ anomalies in to the trigger region during Phase 8.

3.4. Upper-Level Air Temperature

Negative upper-level air temperature anomalies indicate a decrease in static stability, which supports more vigorous deep convection. Upper-level air temperature anomalies may be associated with equatorial waves modulating the upper troposphere during their passage, as suggested by Matthews (2004) and Maloney and Shaman (2008). Thus, air temperature anomalies are filtered by zonal wavenumber and frequency to examine the respective contributions of Kelvin- and Rossby-like disturbances. The

zonally-filtered and total 30-90 day anomalies provide significant evidence about which mechanisms are responsible for decreasing the static stability over north Africa. In particular, the 30-90 day ERAi 400 hPa air temperature is analyzed in order to understand how the upper troposphere temperature variations may affect the large-scale conditions for convection on intraseasonal timescales.

MJO phase composites of 30-90 day bandpass filtered ERAi 400 hPa air temperature anomalies are shown in Figure 3.10. In Phase 1, negative temperature anomalies are widespread over much of tropical north Africa and the east Atlantic, which indicates that the troposphere is more favorable for stronger convection. The anomalous $T_{30\text{-}90}$ pattern supports the deeper convection in Phase 1 and the negative temperature anomalies have magnitudes greater than 0.2 K. Two regions of minimum temperature anomalies straddle the AEJ, with one minima located over the Sahara (-0.5 K) and another of the Gulf of Guinea (-0.35 K). Significant positive $T_{30\text{-}90}$ anomalies appear in northeast Africa before spreading throughout tropical north Africa in Phases 4 and 5. The northeasterly propagation of $T_{30\text{-}90}$ anomalies may suggest the penetration of subtropical energy with the reduction of upper-tropospheric tropical easterlies. $T_{30\text{-}90}$ anomalies may be associated with the North African-Asian (NAA) jet and heating in the central Pacific (Shaman et al. 2009). The NAA jet may act as a "westerly duct" for 400 hPa $T_{30\text{-}90}$ anomalies.

By Phase 5, significant positive 30-90 day 400 hPa air temperature anomalies fill most of the map, especially south of 20°N. Positive air temperatures aloft increase the static stability and supports less vigorous convection. Therefore, the $T_{30\text{-}90}$ pattern supports this phase being termed the "dry" phase. Maximum $T_{30\text{-}90}$ anomalies once again

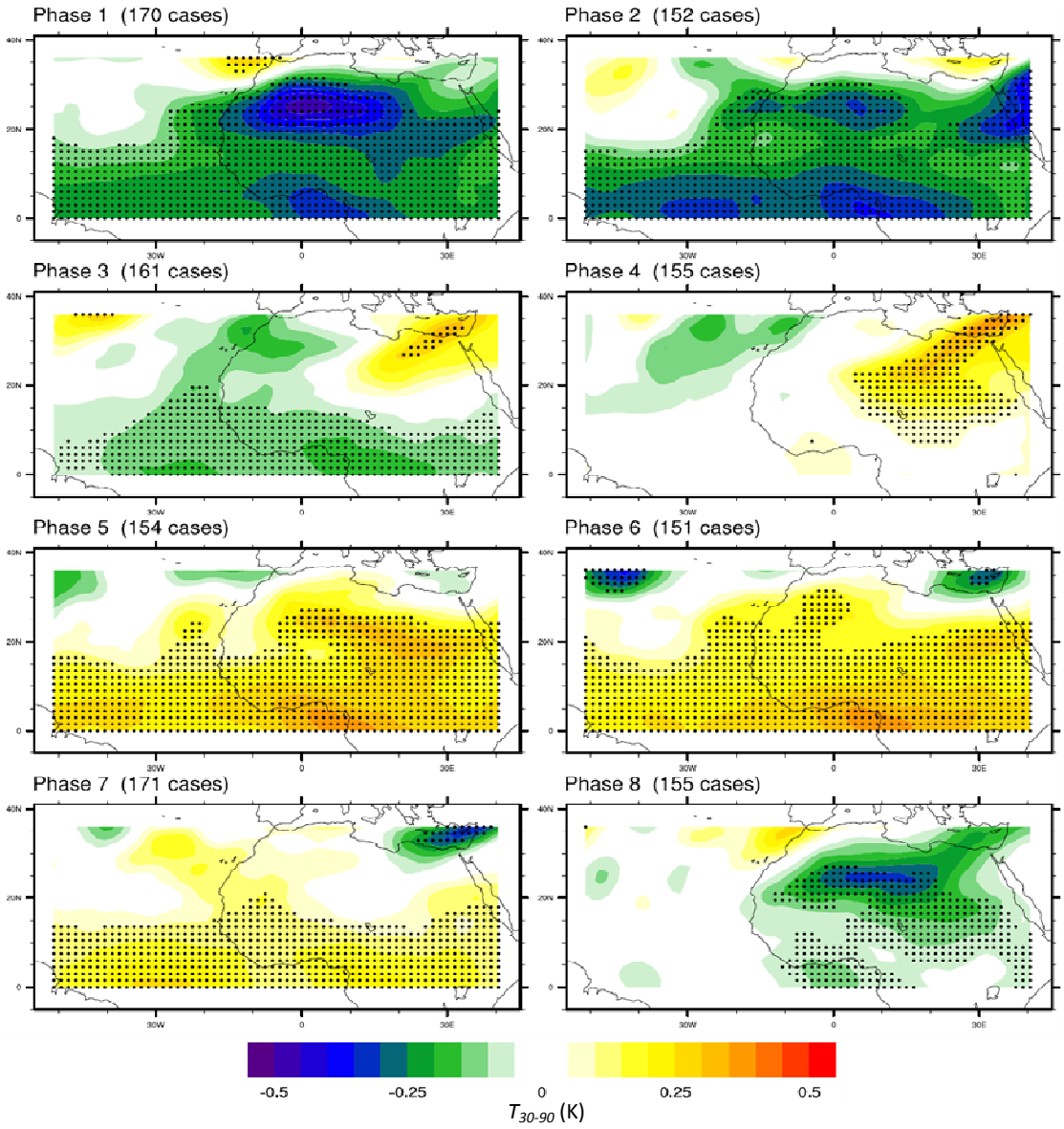

Figure 3.10. MJO phase composites of ERAi anomalous 30-90 day 400 hPa air temperature for June-September. The scale is given by the color bar. The shading interval is 0.05 K. The dots represent significant data points at the 95% confidence interval.

straddle the AEJ and are located in the Gulf of Guinea (0.35 K) and the eastern Sahara (0.3 K).

Phase 8 depicts significant negative upper tropospheric $T_{30\text{-}90}$ anomalies in the vicinity of the trigger region, which insinuates that more vigorous convection is supported, which favors upstream precursor disturbances that may seed the AEJ. Anomalies are on the order of -0.2 K and seem to be associated with a 30-90 day

temperature minimum extending outward from the Sahara. Given the emergence of a potential precursor signal in the 400 hPa $T_{30\text{-}90}$ field, eastward and westward zonal wavenumber-filtered composites are created to analyze the temperature anomalies associated with large-scale flow and provide attribution of the observed temperature anomalies.

Figure 3.11 shows $T_{30\text{-}90}$ anomalies that are filtered for large-scale (zonal wavenumbers 0 to 10) eastward-propagating disturbances. The significant negative $T_{30\text{-}90}$ anomalies on the order of 0.1-0.2 K over tropical northern Africa in Phase 1 support the anomalies witnessed in Figure 3.10. Importantly, Phase 1 features two $T_{30\text{-}90}$ minima: one centered along the equator and the other centered at 20°-25°N. While the significant negative $T_{30\text{-}90}$ anomalies along the equator are likely associated with a Kelvin wave response, the origin of off-equatorial $T_{30\text{-}90}$ anomalies in Phase 1 is investigated through Phases 7-8 in Figure 3.11. In Phase 7, significant positive $T_{30\text{-}90}$ anomalies, which are propagating eastward along the equator, are consistent with an equatorial Kelvin wave response from the Indian Ocean. By Phase 8, warm anomalies have diminished near the equator, while eastward-filtered cold $T_{30\text{-}90}$ anomalies encroach on the western boundary of the trigger region. Although it is not clear what is causing this signal, it is consistent with behavior observed in Maloney and Sobel (2007), whereby a warm equatorial temperature anomaly associated with a Kelvin wave response induces off-equatorial cold temperature anomalies that persist even though the warm equatorial temperature anomalies decay. Conversely, significant positive $T_{30\text{-}90}$ anomalies dominate Phase 5 (Figure 3.11), which is also consistent with Figure 3.9. In Phases 3-4, negative equatorial

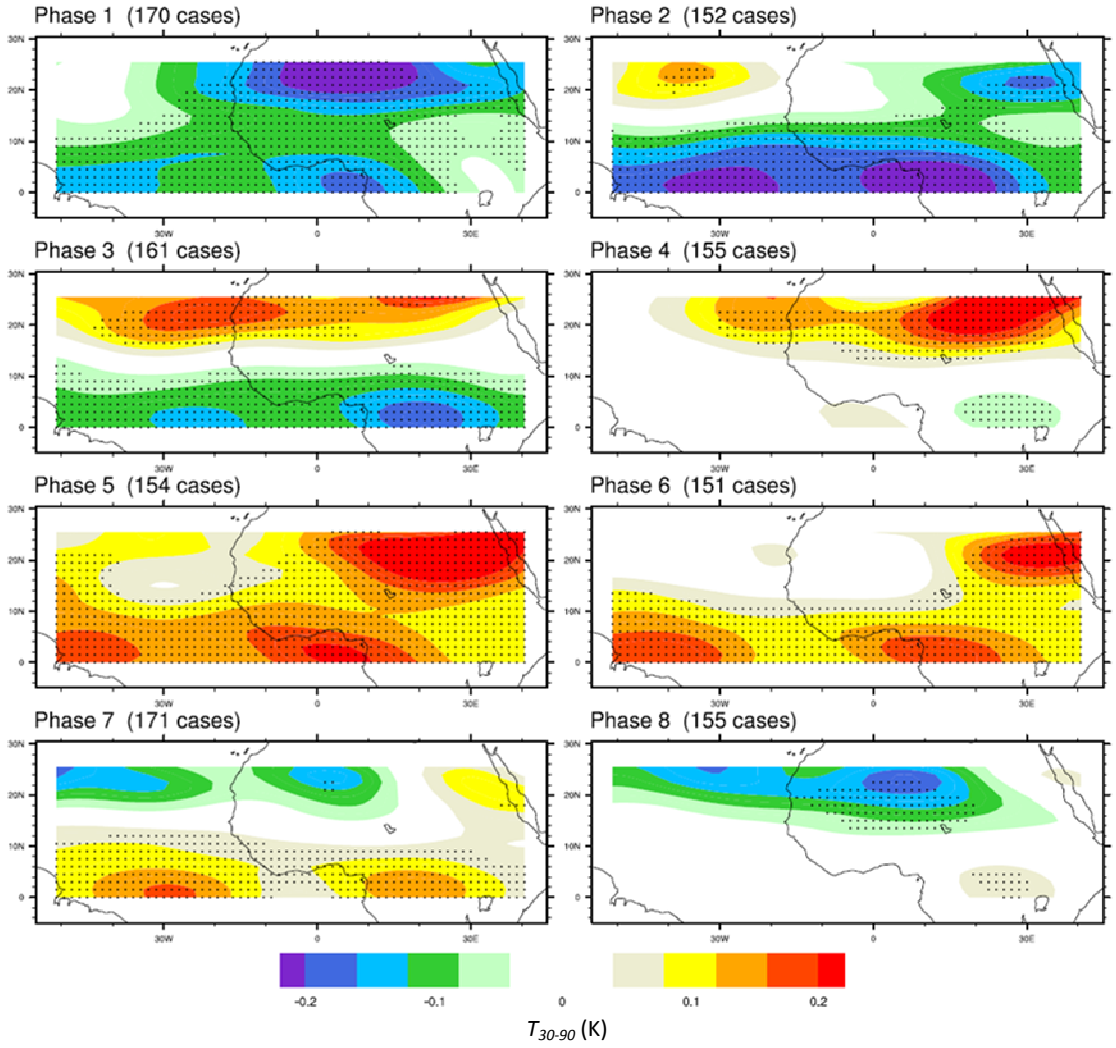

Figure 3.11. MJO phase composites of ERAi anomalous 30-90 day, eastward-propagating 400 hPa air temperature for June-September. The scale is given by the color bar. The shading interval is 0.04 K. The dots represent significant data points at the 95% confidence interval.

$T_{30\text{-}90}$ anomalies may induce the positive off-equatorial $T_{30\text{-}90}$ anomalies that encroach on the trigger region, also consistent with Maloney and Sobel (2007).

The $T_{30\text{-}90}$ anomalies associated with large-scale, westward zonal wavenumbers are not nearly as interesting (Figure 3.12). While significant negative $T_{30\text{-}90}$ anomalies are observed in Phase 1, they are of low amplitude (< 0.1 K). In fact, these negative $T_{30\text{-}90}$ anomalies minimize in Phases 3-4. In Phase 8, negative $T_{30\text{-}90}$ anomalies in association with westward-propagating disturbances are on the order of -0.1 K, but are insignificant

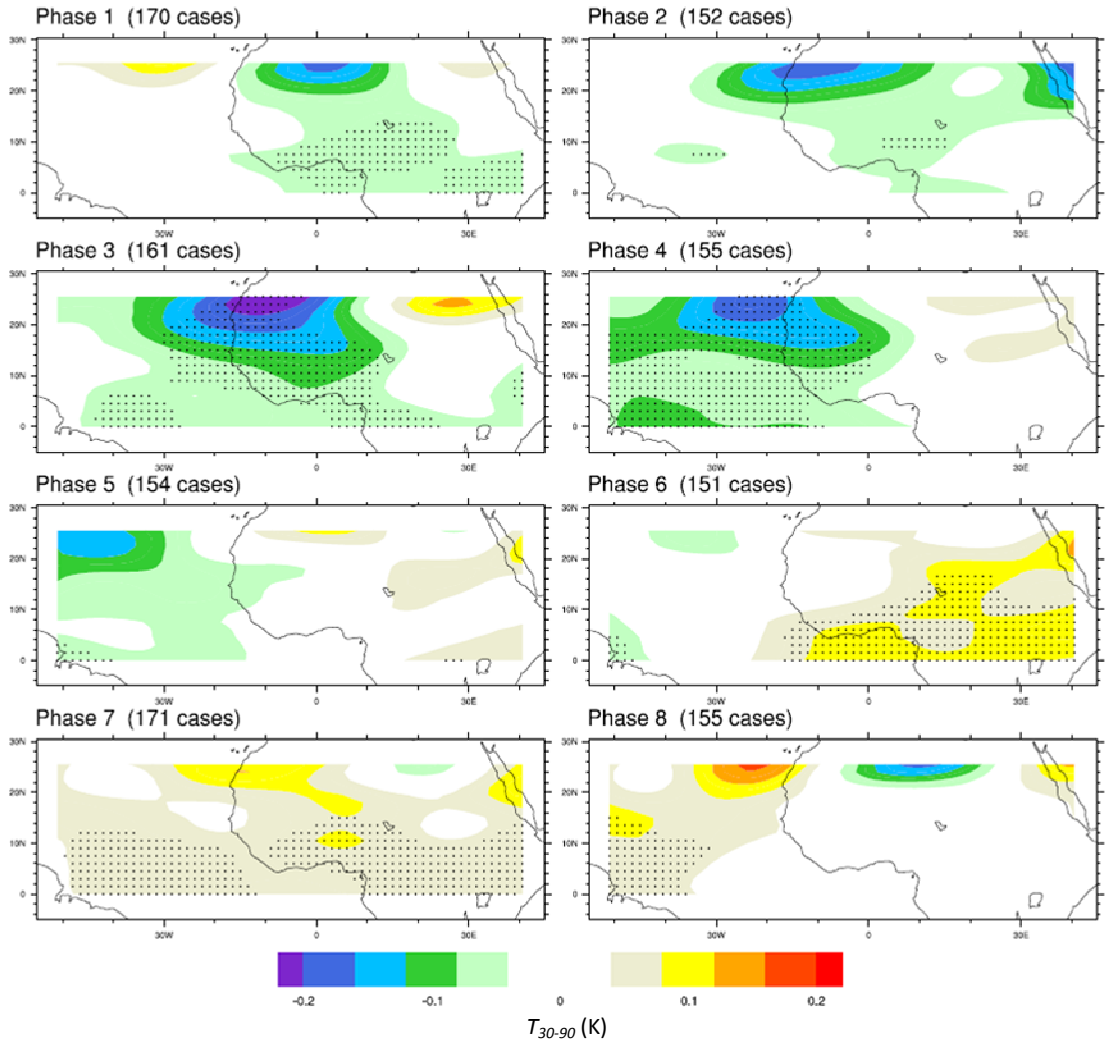

Figure 3.12. MJO phase composites of ERAi anomalous 30-90 day, westward-propagating 400 hPa air temperature for June-September. The scale is given by the color bar. The shading interval is 0.04 K. The dots represent significant data points at the 95% confidence interval.

at the 95% confidence interval and displaced to the northwest of the trigger region and to the north of the AEW development region.

Figure 3.13 displays the 0°-10°N average of anomalous 30-90 day 400 hPa air temperature for eastward zonal wavenumbers. The plot for westward-propagating zonal wavenumbers is not included due to a lack of interesting results. Positive MJO convective anomalies initiate near the equator at approximately 75°E -90°E near Phase 1. As an MJO event begins, positive upper-tropospheric temperature anomalies grow via

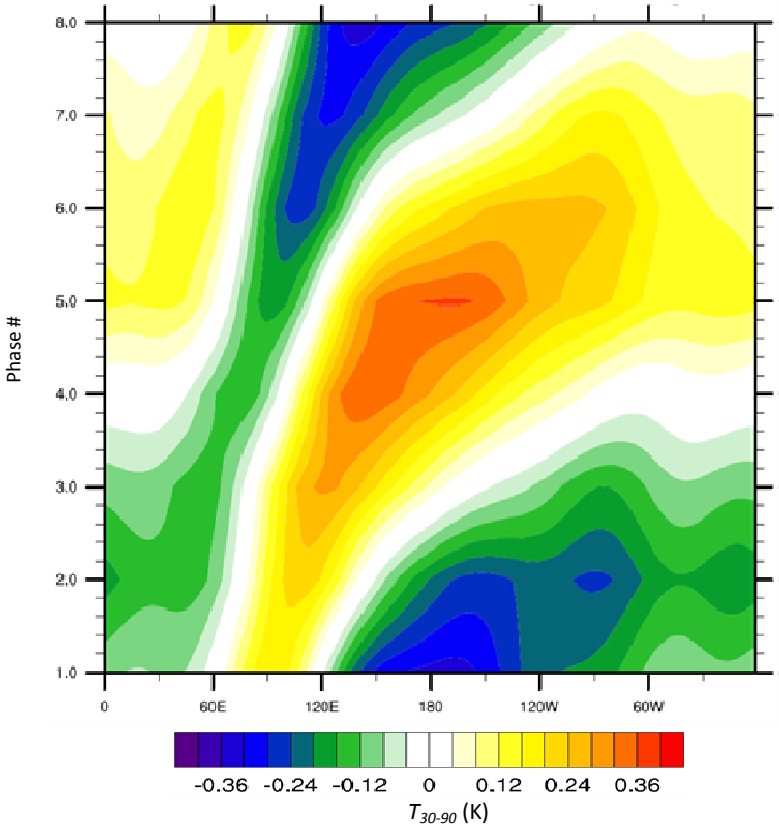

Figure 3.13. Phase vs. Longitude for anomalous 30-90 day air temperature for eastward zonal wavenumbers 0 to 10 from 0°-10°N. The plot shows the propagation of temperature as a function of phase.

condensational heating. The opposite is the case for the negative phase of the MJO, where negative temperature anomalies initiate in the Indian Ocean in Phase 5. In both cases, these anomalies propagate slowly to the east at approximately 5 m s^{-1} until they reach the dateline. Anomalies accelerate eastward to the east of the dateline, with average phase speeds of about 15 m s^{-1}. This observation supports the notion that Kelvin waves travel faster once east of the dateline, which is likely due to the wave decoupling from convection. Despite the presence of Kelvin-type disturbances propagating from the Indian Ocean, Figure 3.13 strongly suggests that 0°-10°N temperature anomalies initiated by the negative phase of the MJO (Phase 5) arrive in northern Africa by Phase 1 and maximize in Phase 2. Thus, it is reasonable to conclude that eastward-propagating 30-90

day air temperature anomalies associated with negative Kelvin waves do not destabilize the upper troposphere over northern Africa in advance of convection. Instead, the negative temperature anomalies associated with Kelvin waves may reinforce the positive convective anomalies that have already been initiated. However, the large-scale off-equatorial $T_{30\text{-}90}$ anomalies associated with eastward zonal wavenumbers may be induced by an equatorial Kelvin wave response to MJO heating and reduce the static stability near the trigger region in advance of the convective maximum in Phase 1. These off-equatorial anomalies may be indirectly associated with the previous positive Kelvin wave event. Further investigation is necessary to determine what mechanism is responsible for producing off-equatorial $T_{30\text{-}90}$ anomalies in the large-scale eastward flow.

3.5. Upper-Level Vertical Velocity

Vertical velocity is another quantity related to convective activity. Dynamical forcing can support deep convection (e.g. Kiladis et al. 2006), and convection can produce large-scale area-averaged ascen through diabatic heating anomalies. In order to capture the maximum ascent associated with deep convection, vertical velocity is analyzed at the 400 hPa level. When filtered to intraseasonal timescales, the vertical velocity field over tropical north Africa may provide evidence of deep convective variability associated with the MJO. Additionally, zonal wavenumber filtering is incorporated to analyze respective contributions from eastward and westward components of the flow.

ERAi 30-90 day 400 hPa vertical velocity anomalies are composited for the eight MJO phases (Figure 3.14). Significant negative $\omega_{30\text{-}90}$ anomalies, which are indicative of

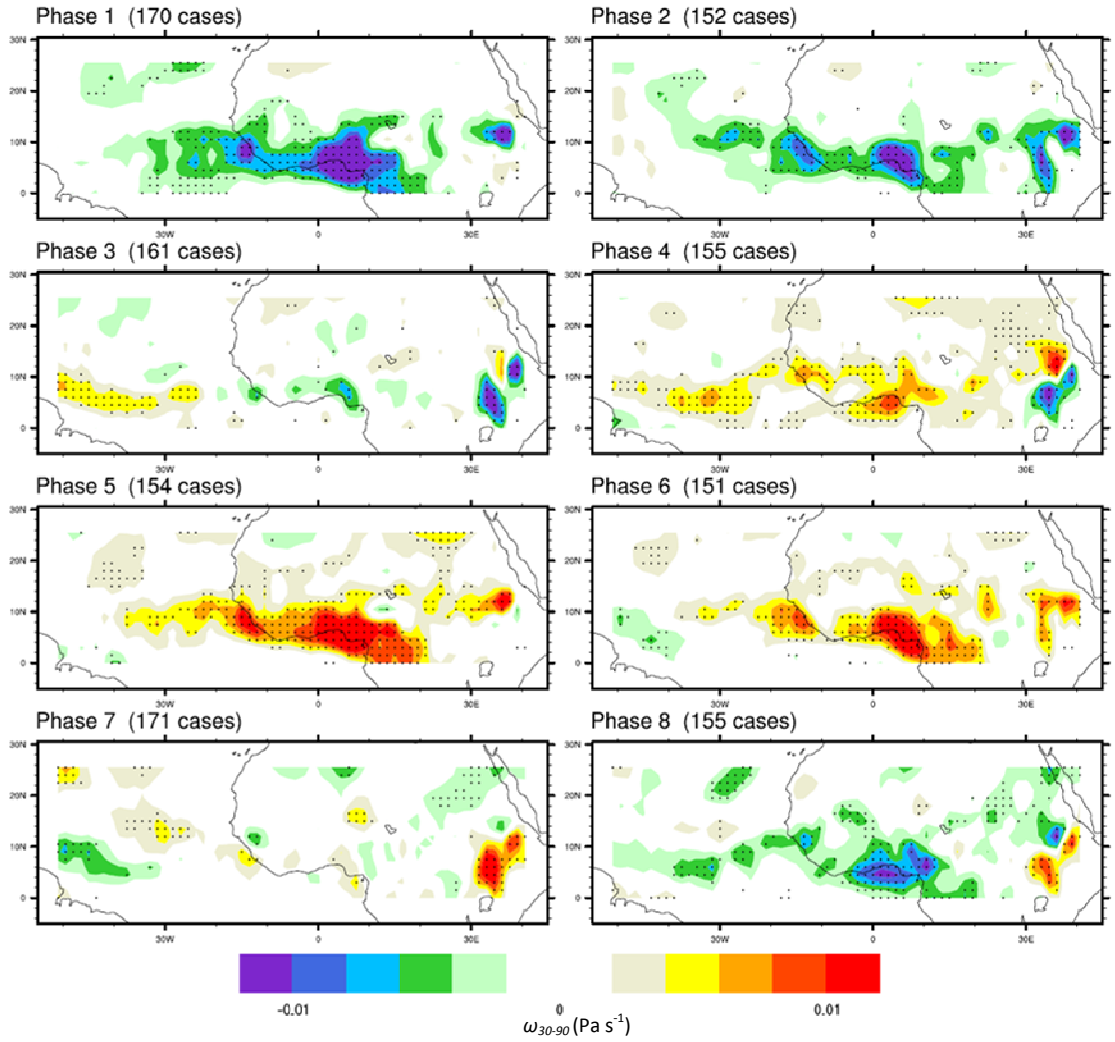

Figure 3.14. MJO phase composites of ERAi anomalous 30-90 day 400 hPa vertical velocity for June-September. The scale is given by the color bar. The shading interval is 1x10^{-3} Pa s^{-1}. The dots represent significant data points at the 95% confidence interval. Negative values represent ascent.

ascent, are widespread cross tropical west Africa and the tropical east Atlantic in Phase 1. Ascent within the AEW development region is consistent with the analyses of brightness temperature, precipitation, TPW, and upper-tropospheric temperature performed thus far. The ascent maximizes at around 0.01 Pa s^{-1} in the Gulf of Guinea and just inland, as well as at the west African coast at 9°N. Phase 5, or the dry phase, is also consistent with the analysis of other fields, as pervasive descent dominates tropical west Africa and the tropical east Atlantic.

The intraseasonal variability within the trigger region suggests a significant enhancement of rising motion in Phases 7 and 8, or about 5-10 days before the wet phase. The ascent is coincident with the anomalously high TPW values in Phases 7 and 8 (Figures 3.7, 3.8) and highlights the relationship between rising motion, low-level convergence, and column moisture. By Phase 1, significant vertical velocity anomalies shift south of 15°N and are likely associated with an increase in AEW development region activity.

Zonal wavenumber filtering is employed once again in order to isolate contributions from eastward and westward components of the flow that include Kelvin and Rossby waves. In Figure 3.15(a-c), the intraseasonal variability in vertical velocity for eastward (green dashed) and westward (blue dashed) zonal wavenumbers is given as a function of phase for the trigger (a), land (b) and ocean (c) regions. In particular, $\omega_{30\text{-}90}$ anomalies are filtered for wavenumbers 0 to 10 for large-scale eastward flow components and from -1 to -10 for large scale westward flow components.

Figure 3.15a reveals that eastward- and westward-propagating components of 30-90 day vertical velocity anomalies are out of phase with one another in the trigger region. Weak ascent that is associated with westward zonal wavenumbers is evident in Phase 7, although this anomaly is almost completely cancelled by the large-scale eastward component. In fact, 30-90 day $\omega_{30\text{-}90}$ anomalies filtered for westward zonal wavenumbers lead the total 30-90 day anomalies by 1-2 phases, the Phase 7 behavior in the trigger region suggests that westward wavenumbers explain most of the ascent signal in this region.

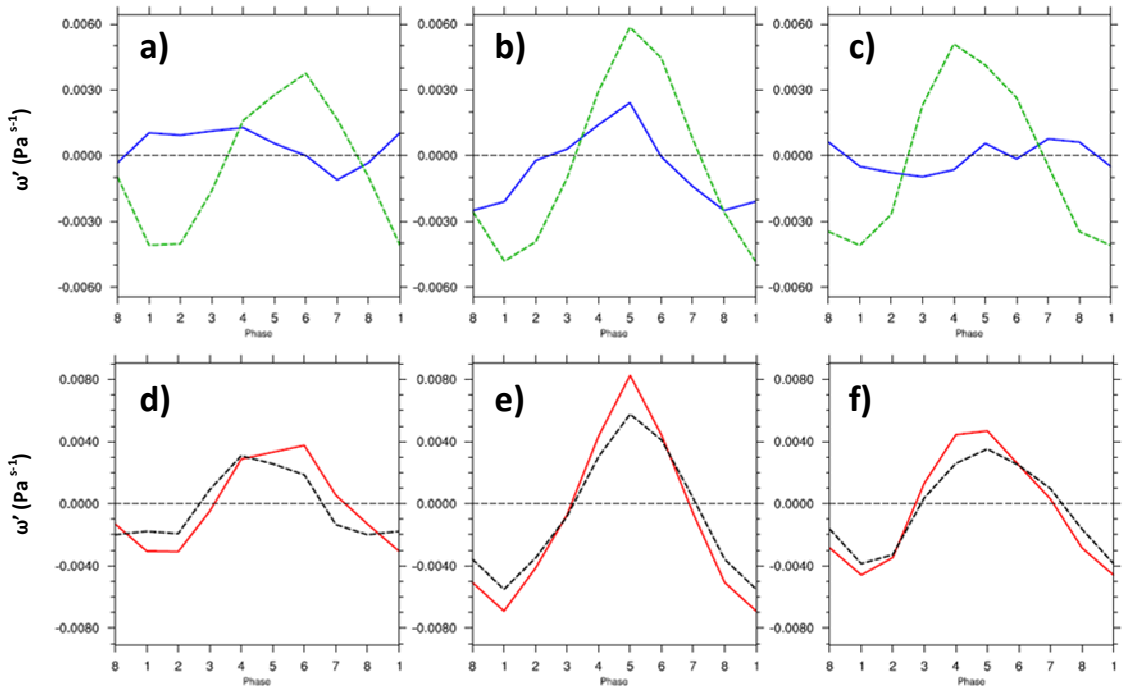

Figure 3.15. Convective box line plots for ERAi 30-90 day vertical velocity (ω) anomalies. (a-c) show how ω' evolves as a function of phase for eastward (green dashed) and westward (solid blue) zonal wavenumbers. (d-f) illustrate how well the 30-90 day ω anomalies with wavenumbers [-10, 10] (red solid) match up with the total 30-90 day anomalies (black dashed). The trigger box is shown in a) and d). The land box is shown in b) and e). The ocean box is shown in c) and f). Values are ω' averaged for each phase over the three regions of interest.

The large-scale (zonal wavenumbers -10 to 10) and total 30-90 day vertical velocity anomalies are compared in Figure 3.15(d-f). Overall, the large-scale vertical velocity anomalies match up quite well with the total $\omega_{30\text{-}90}$ anomalies, indicating a strong link between ascent variations and large-scale disturbances over tropical north Africa. Upon closer inspection, the progression of vertical velocity is quite similar for the large-scale and total flows for the land (Figure 3.15e) and ocean (Figure 3.15f) regions. In the trigger region, the large-scale $\omega_{30\text{-}90}$ anomalies, which maximize in Phase 6, explain most of the total $\omega_{30\text{-}90}$ anomalies for all phases (Figure 3.15d). The $\omega_{30\text{-}90}$ anomalies filtered for large-scale eastward and westward zonal wavenumbers combine to describe most of the total intraseasonal anomaly in the trigger region for all MJO phases. Large-scale

zonal wavenumbers also make significant contributions to the total $\omega_{30\text{-}90}$ in the land and ocean regions. Thus, Figure 3.15(d-f) suggests that vertical velocity anomalies over tropical north Africa and the tropical east Atlantic are mostly governed by the large-scale flow. In particular, vertical velocity associated with eastward- and westward-propagating disturbances may reinforce convection via anomalous ascent in Phase 8, which is in advance of the wet phase.

3.6. Flow Field Variability

Examining variations in the large-scale flow are crucial to understanding the relationship between the MJO, African convection, the west African monsoon, and large-scale disturbances propagating through the region. Lower-tropospheric vector wind, the AEJ, and upper-tropospheric vector wind are analyzed here to assess behavior during the wet and dry phases defined in Section 3.1. Then, how the flow contributes to upstream convection prior to the wet phase over northern Africa is examined. Variations in the flow over tropical north Africa may be induced by MJO heating anomalies in the Indian Ocean (Matthews 2004; Janicot et al. 2009).

3.6.1. 850 hPa Vector Wind

Examination of the low-level flow is important for diagnosing variations in southwesterlies associated with the west African monsoon, in addition to isolating aspects of the flow variations that may affect the moisture budget through the modulation of moisture advection. The June-September mean ERAi 850 hPa vector wind is plotted in Figure 3.16. In the boreal summer mean, a low-level convergence center is located at

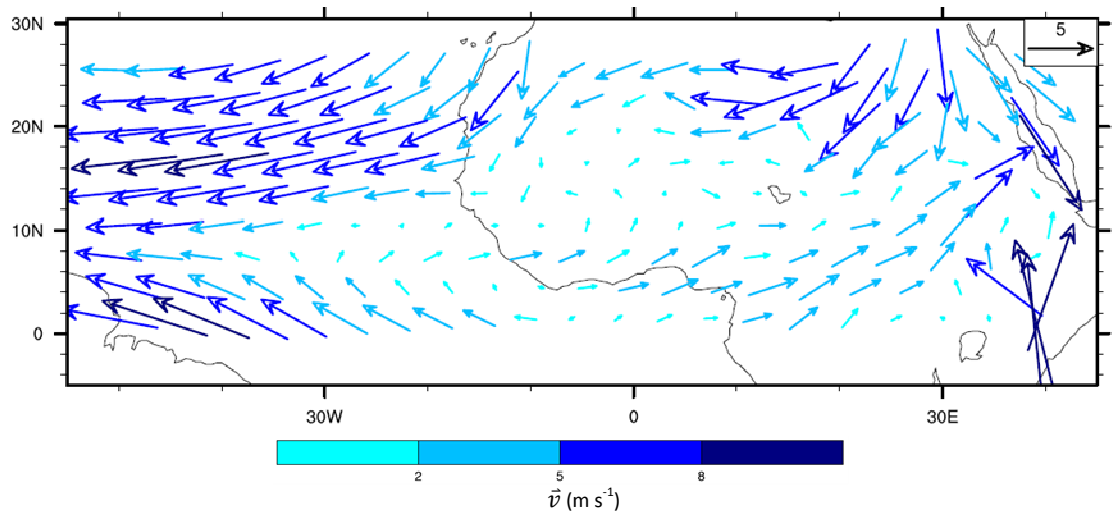

Figure 3.16. June-September mean ERAi 850 hPa vector wind. Units are m s^{-1}. The shading is given by the color bar.

approximately 15°N, 25°E, which is within the trigger region. This convergence zone is located close to the AEJ entrance, consistent with a possible origin of AEW convection in the boreal mean. Additionally, the southwesterly west African monsoon flow is approximately 3-4 m s^{-1} and is located from 20°W to 30°E and the equator to 15°N. The monsoon flow is characterized by low-level southwesterlies that produce a convergence zone and a region of cyclonic shear when combined with easterlies along 20°N. The subtropical ridge is the dominant feature at low levels over the eastern Atlantic, with easterly flow on its southern fringe and boreal mean velocity approaching 10 m s^{-1}. The southern periphery of the subtropical ridge steers AEWs upon their emergence into the Atlantic.

MJO phase composites of the anomalous 30-90 day ERAi 850 hPa vector wind were created in Figure 3.17. Combined with the boreal mean low-level flow pattern, intraseasonal anomalies provide insight about how that flow is enhanced or suppressed as a function of MJO phase. Phase 1 features anomalous westerlies and southwesterlies associated with the west African monsoon west of Greenwich and south of 15°N, which

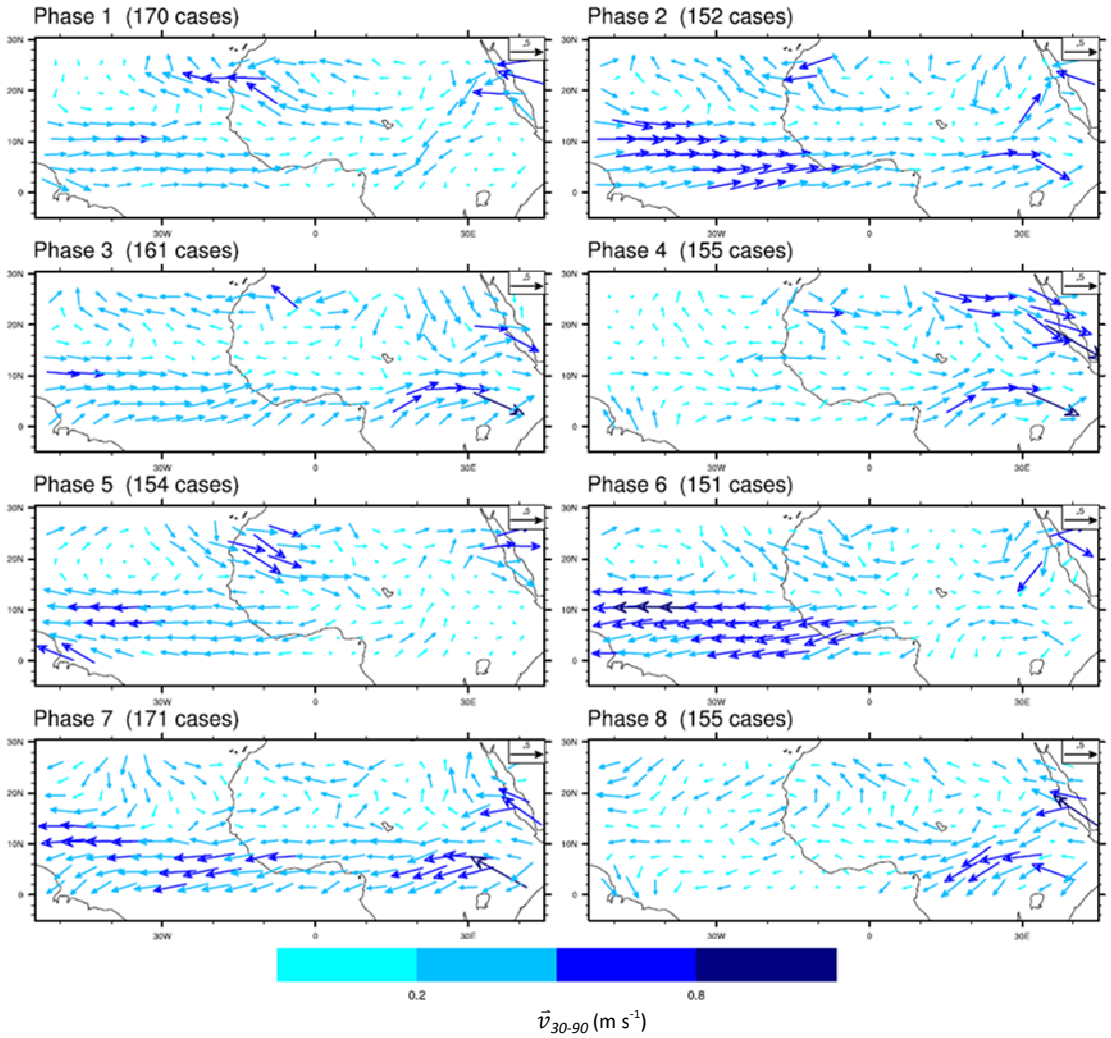

Figure 3.17. MJO phase composites of ERAi anomalous 30-90 day 850 hPa vector wind anomalies for June-September. The scale is given by the color bar. Units are in m s^{-1}.

suggests that onshore moisture advection may help the maintenance of waves in the AEW development region. Additionally, anomalous easterlies north of the monsoon flow in Phase 1 help create a low-level cyclonic shear zone. To the east of Greenwich, low-level northeasterly anomalies, which have magnitudes approaching 0.5 m s^{-1}, extend along an axis from the trigger region to the Gulf of Guinea. This flow suggests that the trigger region is characterized by negative moisture advection in Phase 1 (compare with Figure 3.6). Phases 2-4 feature the eastward propagation of anomalous westerlies at low latitudes. In particular, westerly anomalies dominate 0°-10°N in Phase 3 over all of

tropical north Africa and the tropical Atlantic (although they are in decay). Despite the widespread enhancement of monsoon flow in Phase 3, Figures 3.1 and 3.4 suggest that the onset of enhanced monsoon flow west of Greenwich is more strongly associated with enhanced convection. By Phase 5, low-level vector wind anomalies are easterly in the tropical Atlantic and tropical west Africa. The suppression of monsoon flow west of Greenwich in Phase 5 correlates with negative convective anomalies (Figure 3.1).

In Phases 6-8, low-level easterly anomalies south of 15 °N grow and recede from west to east. While these phases mark a transition of anomalous easterlies back to anomalous westerlies, they also reveal important aspects of the flow in the trigger region. In particular, anomalous southerly flow across the sharp basic state moisture gradient (see Figure 3.6) indicates positive moisture advection into this region. Positive moisture anomalies in this region support the initialization of convection in advance of Phase 1. Meridional moisture advection is further analyzed in Section 4.

The low-level 30-90 day vector wind is filtered for large-scale (zonal wavenumbers -10 to 10) eastward- or westward-propagating disturbances that may account for the observed variability in intraseasonal flow. The 30-90 day vector wind anomalies for eastward zonal wavenumbers are shown in Figure 3.18. Upon comparing Figures 3.17 and 3.18, it is evident that anomalies filtered for eastward-propagating wavenumbers describe most of the total 30-90 day low-level flow, especially at low latitudes. Thus, disturbances with eastward zonal wavenumbers strongly contribute to the total 30-90 day vector wind flow.

Figure 3.18 reveals a Kelvin wave signature consistent with the findings of the eastward-propagating, 30-90 day 400 hPa temperature anomalies in Figure 3.13. The

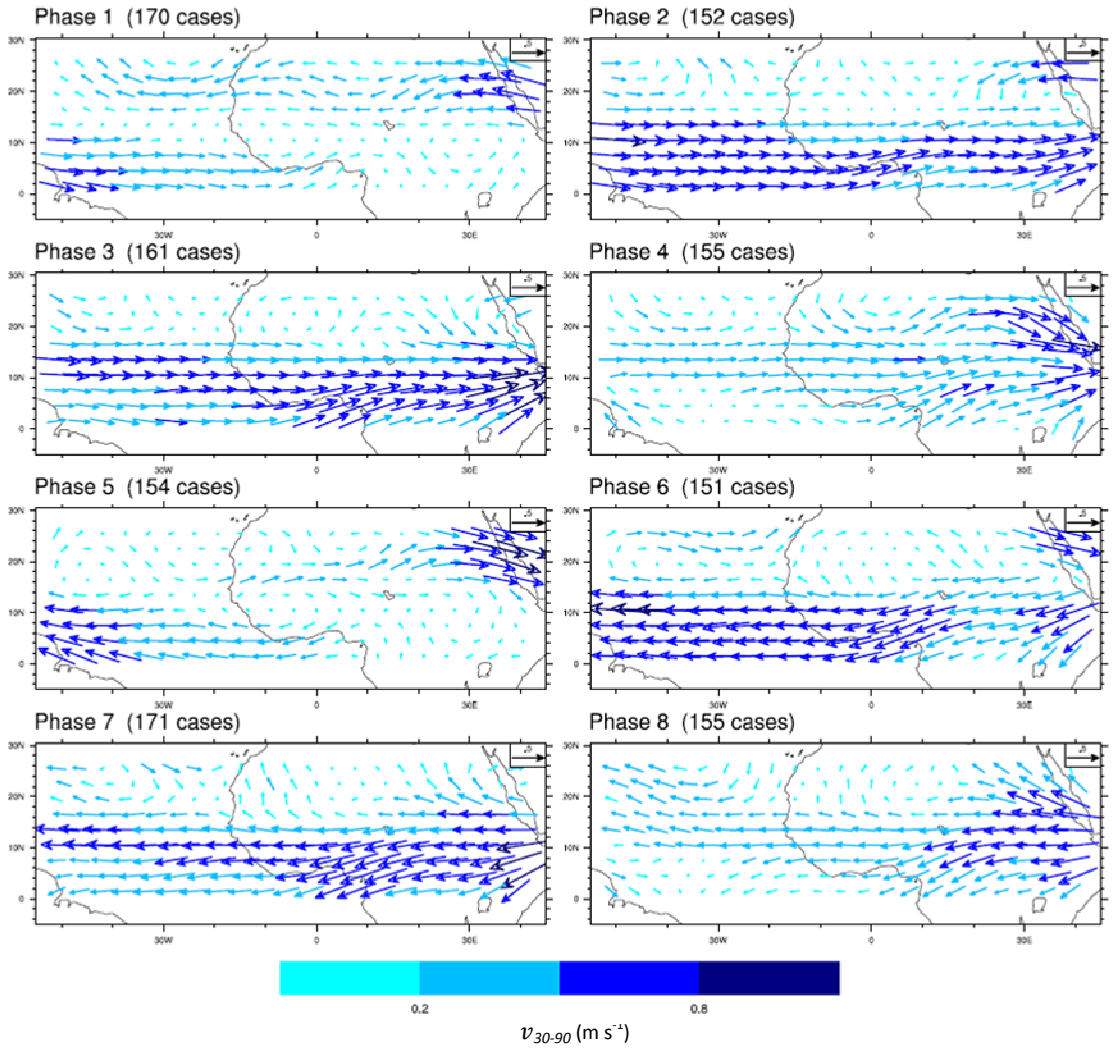

Figure 3.18. MJO phase composites of ERAi 30-90 day, eastward-propagating 850 hPa vector wind anomalies for June-September. The scale is given by the color bar. Units are in m s^{-1}.

negative phase of the Kelvin wave is characterized by anomalous westerlies, is associated with negative 400 hPa temperature anomalies, and is a response to negative MJO convection anomalies the Indian Ocean that initialize in Phase 5. In Phases 1-3, this Kelvin wave signature can be seen propagating eastward along the equator in tropical north Africa and the tropical Atlantic. The corresponding positive phase of the Kelvin wave can be seen in Phases 5-7.

Figure 3.19 shows the 30-90 day 850 hPa vector wind anomalies filtered for westward zonal wavenumbers. While westward-propagating $\vec{v}_{30\text{-}90}$ anomalies do not

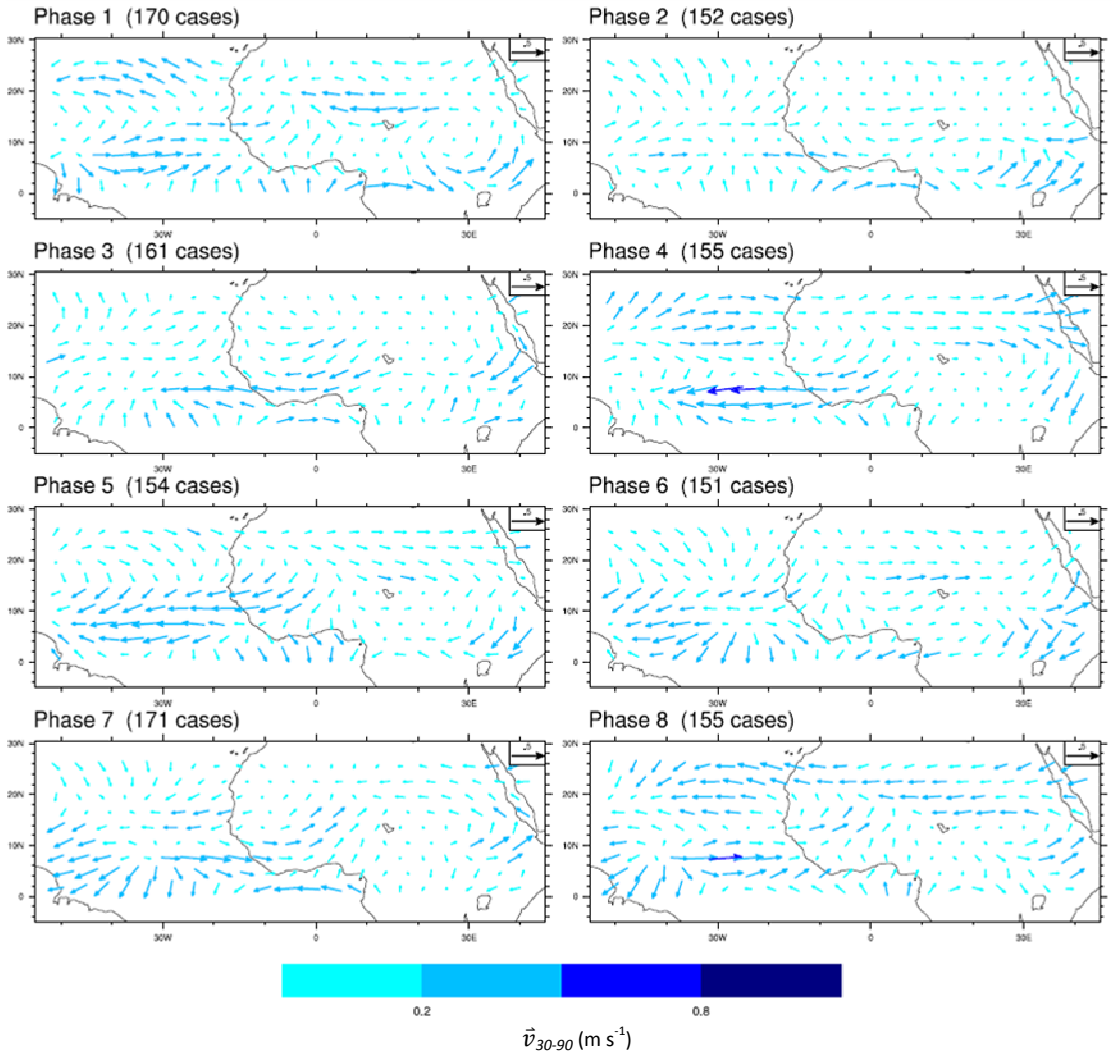

Figure 3.19. The same as Figure 3.18, except for westward zonal wavenumbers.

describe much of the total $\vec{v}_{30\text{-}90}$ anomalies, the flow pattern in Figure 3.19 does have strong coherence with 30-90 day convective anomalies. In particular, westerly onshore flow in Phase 8 supports negative brightness temperature anomalies (Figure 3.1). Additionally, a low-level cyclonic feature, which is located at 13°N, 30°E in Phases 7-8, supplies southerly flow to the trigger region and supports meridional moisture advection (Figure 4.3). In Phase 1, southerly and southwesterly flow extends from 40°W to the Gulf of Guinea, which is associated with and supports the widespread convective and precipitation anomalies witnessed in Figures 3.1 and 3.4. Therefore, while eastward-

propagating disturbances describe most of the total $\vec{v}_{30\text{-}90}$ anomalies, westward-propagating $\vec{v}_{30\text{-}90}$ anomalies produce important anomalies that likely significantly affect and are coherent with the observed convective pattern. Recall that in Figure 3.1, a general westward propagation of brightness temperature anomalies occurs.

3.6.2. African Easterly Jet

The African easterly jet (AEJ) is crucial to the propagation and maintenance of AEWs (Thorncroft and Hoskins 1994). Examination of the June-September AEJ provides insight to the background state and context for intraseasonal anomalies. Since the jet resides in the mid-troposphere, the June-September ERAi 650 hPa zonal wind is examined (Figure 3.20). The AEJ is the most prominent feature in Figure 3.20, with a maximum easterly magnitude of over 12 m s^{-1} located near the west African coast at 15°N. Another local maximum exists within the AEJ, contains magnitudes in excess of 11 m s^{-1} and is located from 5°W to 5°E. If the -9 m s^{-1} contour is used to demarcate the bounds of the jet, then the AEJ can be seen to extend for about 50° of longitude. The eastern extent, or the "entrance", of the average AEJ is approximately located at 17°E, which is just west of the trigger region. Since the AEJ varies zonally as a function of MJO phase, this entrance region will be seen to reside within the trigger region for some phases. The western end of the AEJ is located at approximately 37°W and extends well into the Atlantic. The AEJ is not purely zonal. To the east of Greenwich, the AEJ core is located at approximately 12°N. Between Greenwich and 15°W, the AEJ is oriented west-northwest with the jet core to the west of 15°W occurring at approximately 15°N. Over

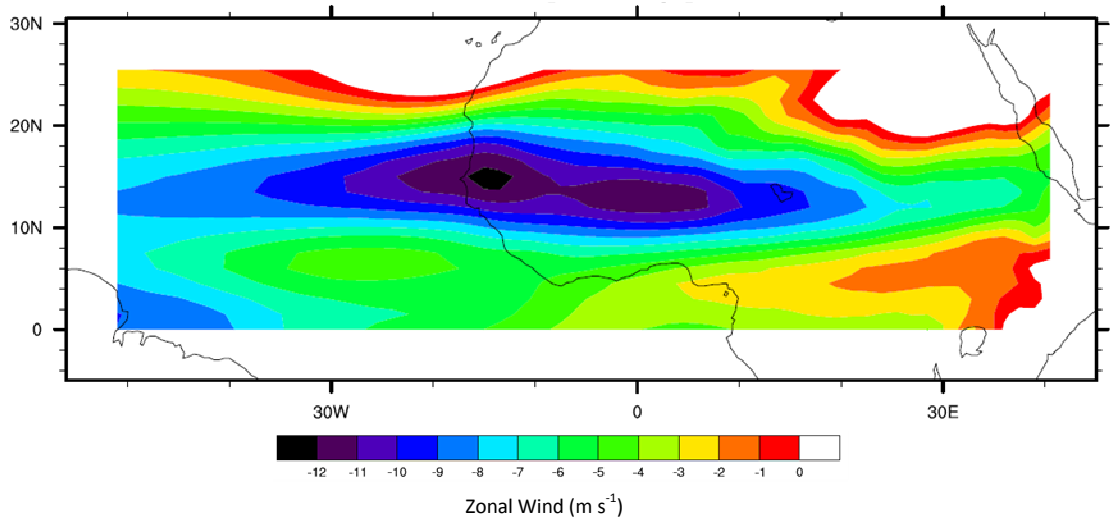

Figure 3.20. The average June-September 650 hPa zonal wind. The scale is given by the color bar. The contour interval is 1 m s^{-1}.

the eastern Atlantic, the AEJ is oriented just south of west. Mid-level winds for much of tropical north Africa and the east Atlantic are easterly.

The intraseasonal variability of the AEJ is examined in Figure 3.21. The entrance region is of particular interest since an extension of the AEJ to the east will not only help the propagation of precursor disturbances, but also would tend to enhance barotropic-baroclinic instability because of a lengthened isentropic potential vorticity (IPV) reversal (Figure 3.22). The IPV reversal is analyzed on the 315 K potential temperature surface, which is located near the center of the AEJ. In Phase 1, which marks the convective maximum over tropical north Africa on intraseasonal timescales, the AEJ is clearly extended to the east. This extension is due to anomalies of approximately -1 m s^{-1} located near the trigger region. In Phase 1, the eastern boundary of the -9 m s^{-1} contour associated with the AEJ is located at 22°E, or about 5° further east than in the boreal mean. The 30-90 day 650 hPa zonal wind anomalies reveal enhanced cyclonic shear located along the axis of the AEJ that extends out into the Atlantic. The induced anomalous cyclonic vorticity is consistent with the enhanced convective activity observed

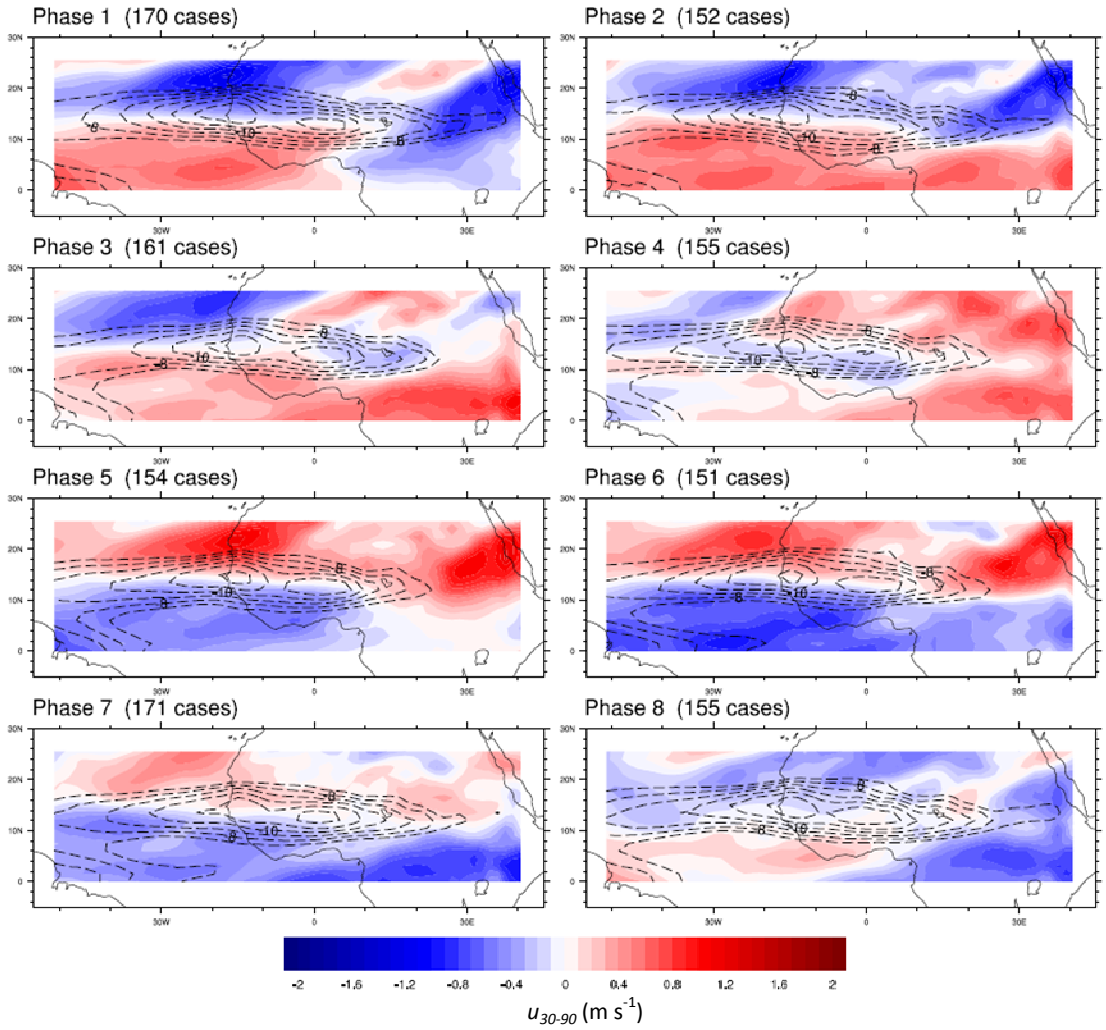

Figure 3.21. The anomalous (shading) and total (contours) ERAi 30-90 day 650 hPa zonal wind. The shading is given by the color bar. The contour interval is 0.1 m s^{-1} for the shading and 1.0 m s^{-1} for the contours. Contours are only plotted for zonal winds values ≤ -7 m s^{-1}.

in Phase 1. The IPV reversal (Figure 3.22) is longer and stronger near the trigger region in Phase 1, which is a response to an extended AEJ in this region as well.

The opposite is true in Phase 5, which has a shorter AEJ coinciding with negative convective anomalies. The shortening of the AEJ may be attributed to 1 m s^{-1} westerly anomalies within the trigger region. Thus, the variations between easterly and westerly anomalies within the trigger region occur in unison with the variations between enhanced and suppressed convection over tropical north Africa. In Phase 5, the eastern boundary of the -9 m s^{-1} contour associated with the AEJ is located at about 13°E, or about 4°

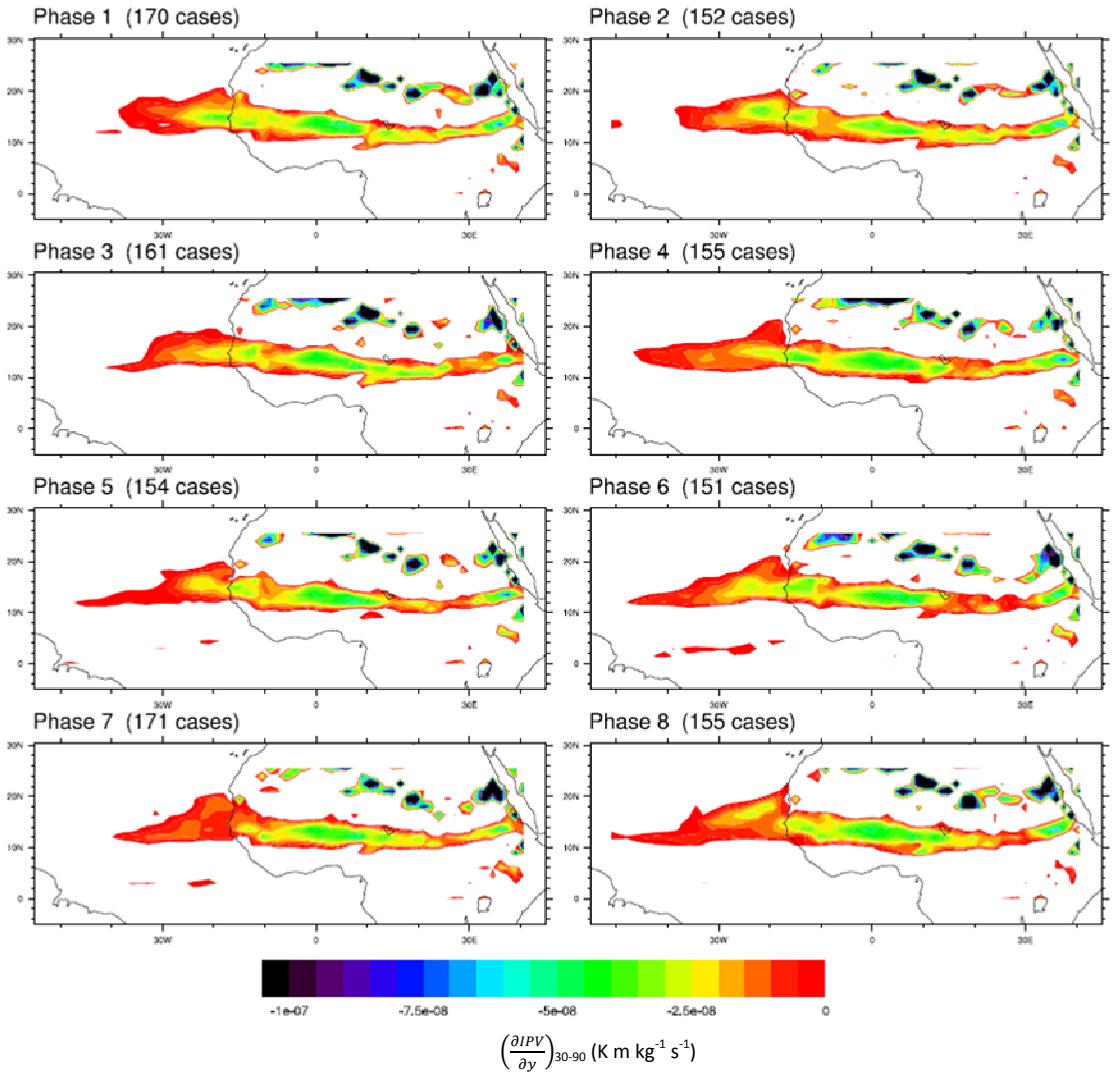

Figure 3.22. The meridional isentropic potential vorticity gradient on the θ = 315 K surface is shown above. Negative values between 0 and -1 x 10^{-7} are shaded, with a contour interval of 5 x 10-9. Units are K m kg^{-1} s^{-1}. These values are not 30-90 day anomalies.

further west than in the boreal mean. Additionally, anomalous anticyclonic shear exists along the axis of the AEJ, which is consistent with reduced convection there (see Figure 3.1). The shortened AEJ is supported by a less intense IPV reversal, particularly to the east of Lake Chad.

Phases 7-8 are investigated in order to assess the contribution of 30-90 day 650 hPa zonal wind anomalies to upstream AEW initiation. During this period, the AEJ begins its eastward extension, marking a transition from the dry phase to the wet phase.

Additionally, easterly anomalies to the south of the AEJ recede to the east, allowing westerly anomalies to grow and contribute to the cyclonic shear zone observed in Phase 1. Figure 3.22 also suggests that the meridional IPV gradient is stronger near the trigger region in Phases 7-8, which supports wave growth via barotropic and baroclinic conversions. The extension of the AEJ to the east in Phase 8 supports more wave growth in the trigger region that enters the jet and propagates downstream.

The contribution of large-scale eastward- and westward-propagating disturbances on zonal wind structure is examined in Figure 3.23. In the trigger region (Figures 3.23a and 3.23d), the large-scale 30-90 day 650 hPa zonal wind anomalies adequately describe the total 30-90 day anomalies. Specifically, the large-scale zonal wind anomalies contribute easterlies to the trigger region in Phase 7, in advance of the Phase 1 convective maximum. Upon closer inspection, the eastward components of the flow contribute introduce anomalous easterlies to the trigger region in Phase 8. In the land and ocean regions, the total (black-dashed) and large-scale (red solid) 30-90 day 650 hPa zonal wind is explained mostly by eastward zonal wavenumbers (green-dashed). Figure 3.23(d-f) suggests that eastward-propagating disturbances are the largest amplitude term in explaining mid-tropospheric zonal wind anomalies over tropical north Africa and the tropical east Atlantic. It is unknown whether or not equatorial waves are responsible for the observed anomalies, although the influx of easterlies in tropical east Africa may reflect a Kelvin wave propagation into the region, which is partially supported by the thermal structure in Figure 3.11. The story is unclear in the triggering region, however. Thus, evidence for Kelvin and Rossby wave signatures that initiate in the Indian Ocean is further examined in upper-tropospheric vector wind anomalies.

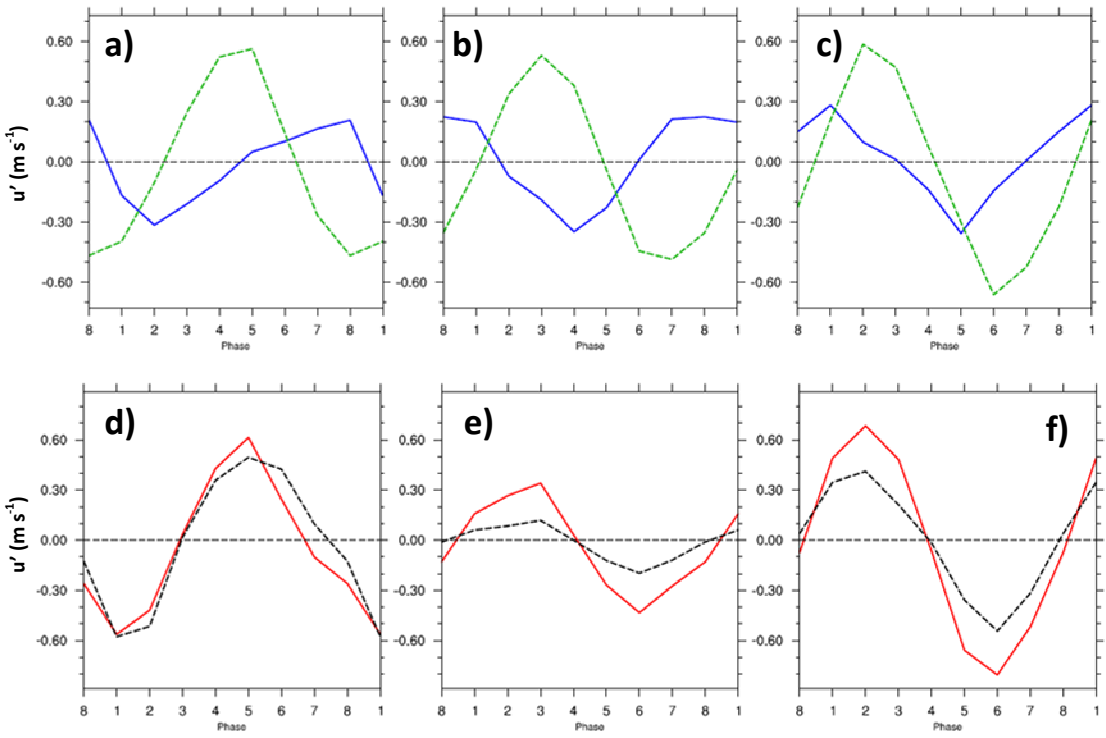

Figure 3.23. Convective box line plots for ERAi 30-90 day 650 hPa zonal wind (*u*) anomalies. (a-c) show how *u'* evolves as a function of phase for eastward (green dashed) and westward (solid blue) zonal wavenumbers. (d-f) illustrate how well the 30-90 day *u* anomalies with wavenumbers [-10, 5] (red solid) match up with the total 30-90 day anomalies. The trigger box is shown in a) and d). The land box is shown in b) and e). The ocean box is shown in c) and f). Values are *u'* averaged for each phase over the three regions of interest.

3.6.3. 200 hPa Vector Wind

The upper-tropospheric vector wind is utilized to identify equatorial waves within the flow. Since both Kelvin and Rossby waves exhibit deep vertical structure, signatures of these equatorial waves may be found in the flow within the sharp heating gradient above the level of mid-tropospheric maximum heating. Above the heating maximum associated with deep convection, the flow flow anomalies are of opposite sign to those at lower levels. For example, a positive heating anomaly will force cyclonic Rossby gyres below the heating maximum. Above the heating maximum, however, the Rossby gyres are anticyclonic. The same relationship is true for Kelvin waves, where a positive heating anomaly will force anomalous easterlies to the east in the lower troposphere and

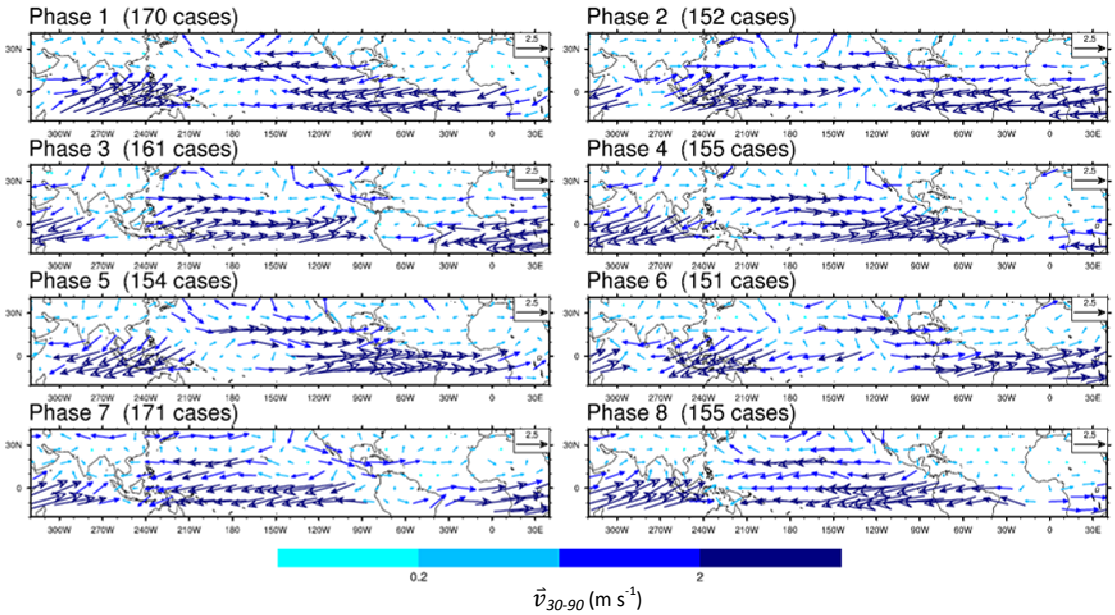

Figure 3.24. MJO phase composites of ERAi 30-90 day, eastward-propagating 200 hPa vector wind anomalies for June-September. Zonal wavenumbers filtering includes 0 to 10. The scale is given by the color bar. Units are in m s^{-1}.

anomalous westerlies above. Examination of the upper-tropospheric wind allows for the investigation of how equatorial waves propagate from the Indian Ocean to tropical Africa.

The propagation of Kelvin wave-type disturbances from MJO heating in the Indian Ocean to Africa is analyzed by filtering ERAi 30-90 day 200 hPa vector wind for eastward-propagating disturbances (Figure 3.24). In Phase 1, the initiation of MJO heating spawns anomalous westerlies in the upper troposphere. These upper-level westerlies are located to the east of MJO heating, and support the notion of a Kelvin wave response to heating that expands to the east. By Phase 5, the 30-90 day upper-level westerly vector wind anomalies approach the tropical Africa. This observation is supported by the propagation of 30-90 day 400 hPa warm temperature anomalies (Figure 3.13). The westerly anomalies propagate through equatorial Africa in Phases 5-8 and back into the Indian Ocean. The diminishment of upper-level westerly anomalies over

tropical Africa in Phase 8 is consistent with the off-equatorial temperature anomalies witnessed in Phase 8 of Figure 3.11 and discussed by Maloney and Sobel (2007), although a suitable explanation for the presence of the anomaly is still required.

Anomalously negative MJO activity in the Indian Ocean is represented by easterly anomalies in Phase 5. These anomalies propagate and spread to the east, arriving at the African coast by Phase 1, which is consistent with the propagation of mid-tropospheric temperature anomalies in Figure 3.13. Therefore, Kelvin waves generated through positive MJO heating anomalies in Phase 1 may be indirectly responsible for reducing the upstream static stability over the trigger region in Phase 8 (consistent with Figure 3.13). Cold Kelvin waves generated by negative MJO heating anomalies in Phase 5 arrive in tropical Africa in Phase 1, and may help maintain convective anomalies that have already maximized over the region.

The impact of Rossby wave-type disturbances on tropical north Africa is examined by filtering ERAi 30-90 day 200 hPa vector wind anomalies for westward-propagating disturbances (Figure 3.25). With the onset of MJO heating in the Indian Ocean, an upper-level anticyclone appears over India in Phase 1. By Phase 4, the anticyclone becomes elongated, spanning from Greenwich to 80°E. This elongation is representative of westward Rossby wave propagation into northern Africa. Additionally, Rossby wave signatures arrive in Africa one phase, or about 5 days, in advance of Kelvin wave anomalies. Negative MJO heating anomalies in the Indian Ocean near Phase 5 force an upper-level cyclone over India that propagates to the west. Phase 6 provides evidence of westward propagation, as the upper-level cyclone becomes elongated to the west. Phase 7 hints at the same elongation of the Rossby gyre as observed in Phase 3,

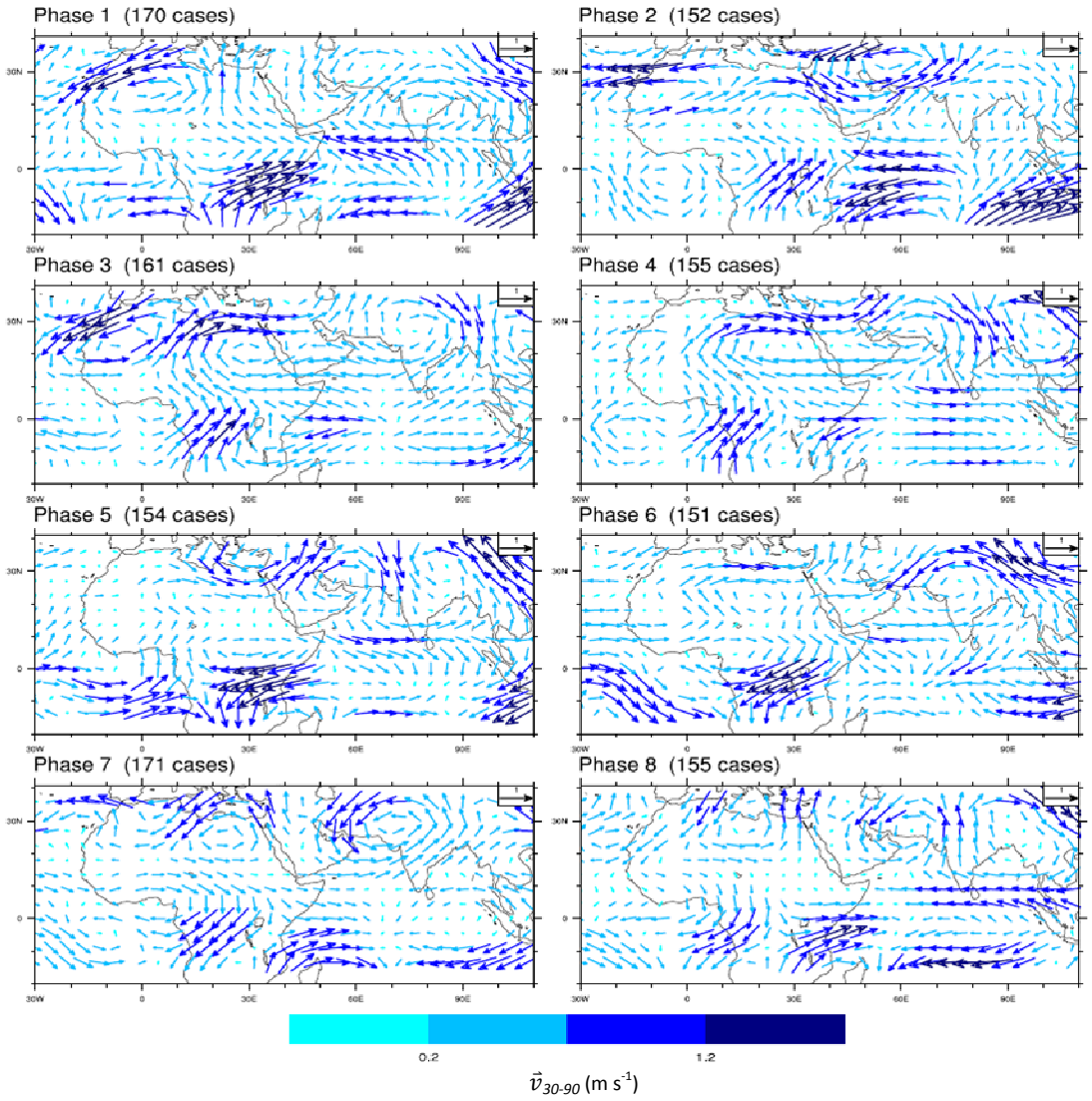

Figure 3.25. MJO phase composites of ERAi 30-90 day, westward-propagating 200 hPa vector wind anomalies for June-September. Zonal wavenumbers filtering includes -1 to -10. The scale is given by the color bar. Units are in m s^{-1}.

although a break in the gyre occurs over Saudi Arabia. Two upper-level cyclones exist in the composite in Phase 7. One of the cyclones is located near (30°N, 70°E), while the other resides near (25°N, 25°E). The western cyclone represents westward Rossby wave propagation that may be associated with the Indian monsoon. Overall, Rossby waves seem to arrive in Africa about 5 days in advance of Kelvin waves. While the propagation of both equatorial waves into Africa is observed, they do not arrive at the same time, as suggested by Janicot et al. (2009).

4. Moisture Budget

The moisture budget is examined to assess processes responsible for moistening (drying) in the trigger region in advance of the MJO wet (dry) phases. The vertically-integrated moisture budget equation is given by:

$$\langle\frac{\partial q}{\partial t}\rangle = -\langle u\frac{\partial q}{\partial x}\rangle - \langle v\frac{\partial q}{\partial y}\rangle - \langle q\nabla\cdot\vec{v}\rangle + E - P - R, \quad (4.1)$$

where q is the specific humidity, E represents the surface evaporation, P represents precipitation, and R is the residual. The term on the left side of (4.1) is the vertically-integrated moisture tendency. On the right side of the moisture budget, the first term describes the vertically-integrated zonal advection of moisture. The second term represents vertically-integrated meridional moisture advection, while the third term denotes vertically-integrated vertical advection of moisture (this can be seen when integrating by parts). Ideally, the residual should be zero, as it does not represent any source or sink of moisture. However, errors in the reanalysis model or errors in computing divergence and advection (since we are not using the native grid of the model) may cause a non-zero residual. In the budget, the evaporation term is a source of moisture, while the precipitation term is a sink of moisture. The three advective terms work to move moisture around in three-dimensional space. The moisture tendency is discussed to provide a sense of how moisture anomalies grow or decay over tropical north Africa. Then, the meridional moisture advection is analyzed since it is the

dominant term in the moisture budget. Finally, all terms in the moisture budget are compared over the trigger region to investigate how the moisture budget terms on the right-hand side of the equation combine to produce the observed moisture tendency anomalies.

4.1. Moisture Tendency

The moisture tendency represents the vertically-integrated time-rate of change of specific humidity or the time-rate of change of TPW, as shown by the following relationship:

$$\left\langle \frac{\partial q}{\partial t} \right\rangle = \frac{\partial TPW}{\partial t}. \tag{4.2}$$

The moisture tendency measures the water vapor entering or leaving the column as a result of sources, sinks, and advection.

Positive moisture tendency anomalies may support subsequent convection. On 30-90 day timescales, growing moisture anomalies may prime the troposphere for convection associated with the MJO. Figure 3.7 showed ERAi total precipitable water anomalies as a function of MJO phase. The intraseasonal moisture tendency is of particular importance to the convective maximum in Phase 1 and should reflect a moistening of the troposphere in the prior phases, particularly in the trigger region. The ERAi anomalous 30-90 day moisture tendency is shown in Figure 4.1. The important feature to note is the significant positive moisture tendency anomalies in Phases 5-7 near the trigger region. The growth of moisture anomalies in the triggering region may make the atmosphere in the Darfur region and east African highlands favorable for convective initiation. This pattern suggests that when convective activity is reduced, moisture is

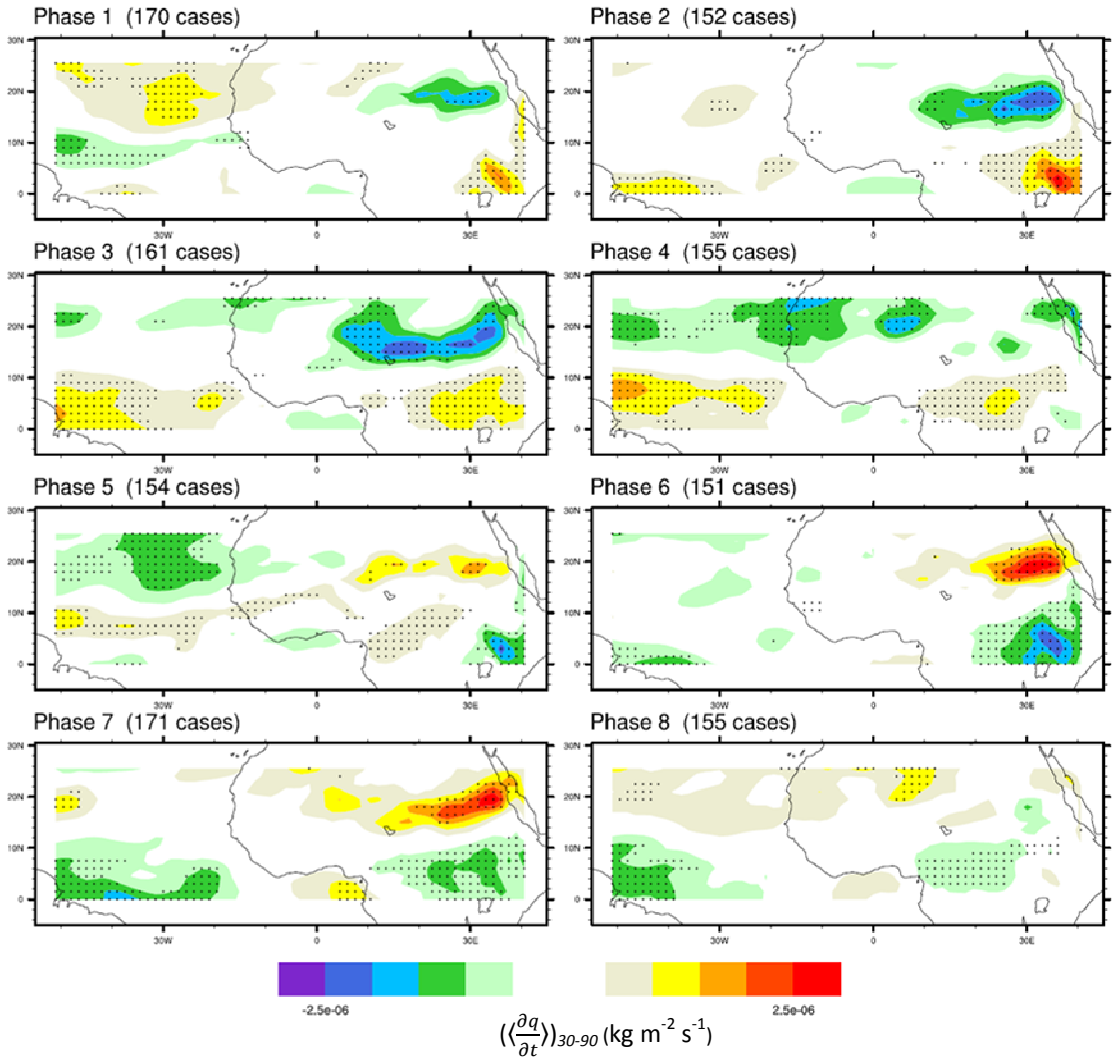

Figure 4.1. MJO phase composites of vertically-integrated ERAi anomalous 30-90 day moisture tendency for June-September. The scale is given by the color bar. The shading interval is 5x10^{-7} kg m^{-2} s^{-1}. The dots represent significant data points at the 95% confidence interval.

already returning to the trigger region, potentially priming the troposphere for convection in Phases 8 and 1 that may seed the AEJ. These tendency anomalies can be seen moving to the west after Phase 7, which is indicative of downstream propagation. In Phase 6, significant and positive 30-90 day moisture tendency anomalies, on the order of 2.5x10^{-6} kg m^{-2} s^{-1}, are located within the trigger region east of 25°E. By Phase 7, these significant and positive anomalies extend to 18°E and cover a larger surface area within

the trigger region. Moisture tendency anomalies disappear by Phase 8, suggesting that the troposphere is fully moistened in the trigger region by this time.

The role of the large-scale 30-90 day moisture tendency anomalies is analyzed in order to investigate contributions from Kelvin- and Rossby-like waves. Figure 4.2 displays the relative contributions of eastward-propagating, westward-propagating and large-scale disturbances to the total 30-90 day moisture tendency anomalies. Of particular importance is trigger region. Figure 4.2d reveals that large-scale 30-90 day moisture tendency anomalies correlate quite well with the total 30-90 day anomalies. When the large-scale zonal wavenumbers are separated by direction of propagation, it is clear that both eastward- and westward-propagating disturbances contribute to observed moisture tendency anomalies within the trigger region. Particularly, Figure 4.2a suggests that anomalies associated with eastward zonal wavenumbers, which peak in Phase 7, describe most of the total moisture tendency anomalies. It is unknown what dynamically causes moisture tendency anomalies associated with eastward components of the flow that maximize in Phase 7, although southerly flow anomalies clearly occur with eastward-filtered wind components at this time (Figure 3.18) that may contribute to positive moisture advection. Despite these observations, stationary moisture tendency anomalies are likely induced by flow field anomalies, which is a more likely scenario than propagation of these anomalies with the large-scale flow. Regardless, moisture tendency anomalies associated with large-scale components of the flow account for most of the observed total 30-90 day anomalies.

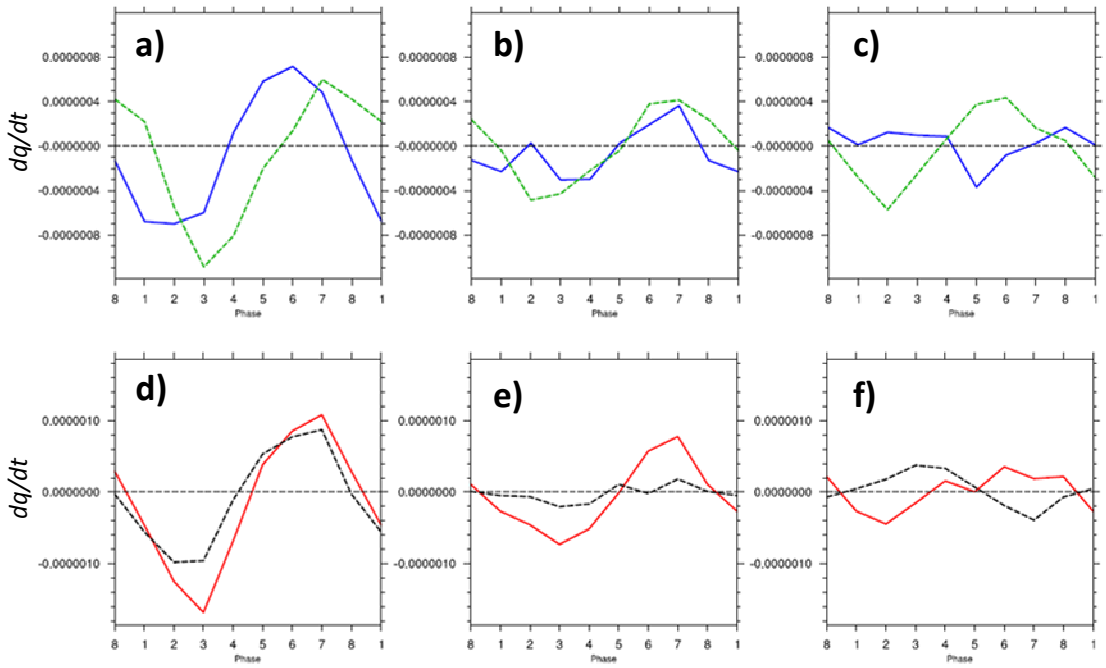

Figure 4.2. Convective box line plots for ERAi 30-90 day moisture tendency anomalies. (a-c) show how *dq/dt* evolves as a function of phase for eastward (green dashed) and westward (solid blue) zonal wavenumbers. (d-f) illustrate how well the 30-90 day *dq/dt* anomalies with wavenumbers [-10, 10] (red solid) match up with the total 30-90 day anomalies (black dashed). The trigger box is shown in a) and d). The land box is shown in b) and e). The ocean box is shown in c) and f). Values are *dq/dt* averaged for each phase over the three regions of interest. The units are kg m^{-2} s^{-1}.

4.2. Moisture Budget Terms in the Trigger Region

Positive moisture anomalies in the trigger region in advance of the convective maximum in Phase 1 support positive upstream convective anomalies that may seed the AEJ. The contributions of moisture budget terms over an MJO lifecycle are compared for the trigger region (Figure 4.3). Intraseasonal $-\langle v \frac{\partial q}{\partial y} \rangle$ anomalies are analyzed in Section 4.3 because they have the strongest amplitude, and almost in phase with the vertically-integrated moisture tendency (Figure 4.1).

The term $-\langle q \nabla \cdot \vec{v} \rangle - P$, which becomes positive in Phase 7, partially cancels the meridional advection term. This term represents the relationship between vertically-integrated moisture convergence and precipitation, which generally balance. In this case,

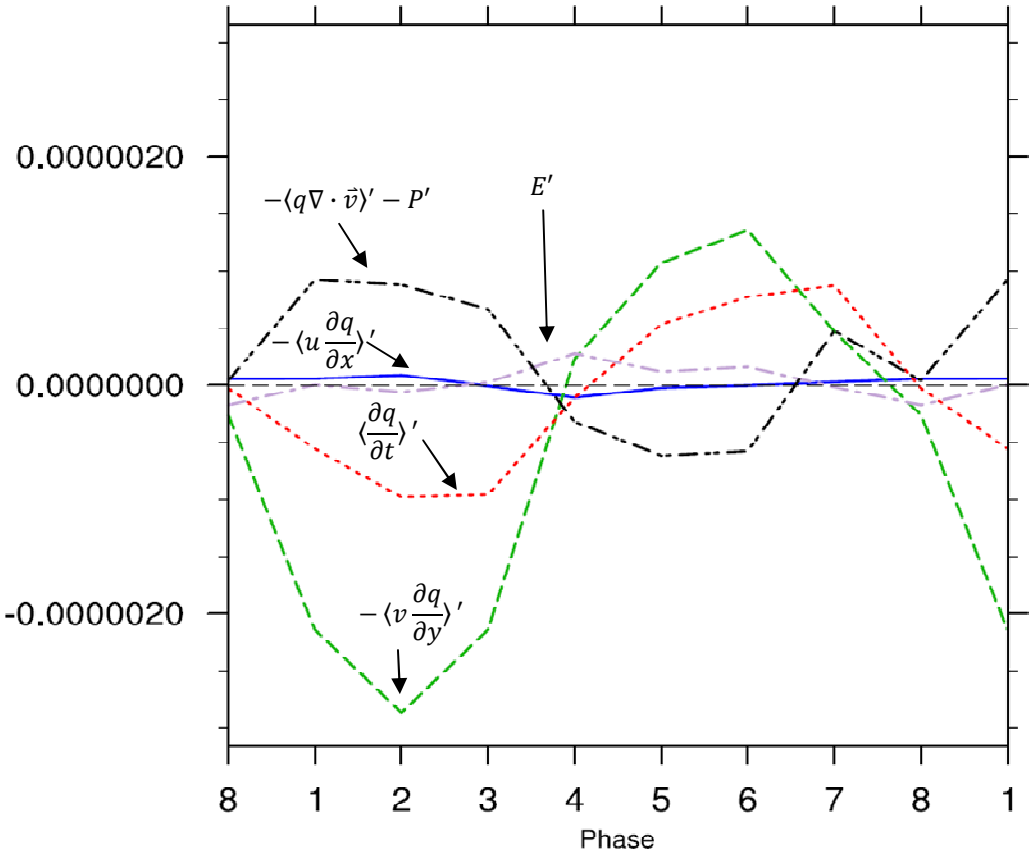

Figure 4.3. Convective averaging line plots for 30-90 day moisture budget terms in the trigger region. Terms shown include moisture tendency (red, dotted), zonal moisture advection (blue, solid), meridional moisture advection (green, dashed), the difference between vertical moisture advection and precipitation (black, dashed-double-dotted), and evaporation (gray, dashed-dotted). The residual is not included.

a non-negligible residual contributes an imbalance between convergence and precipitation. However, if vertically-integrated moisture convergence anomalies outweighs precipitation anomalies, $-\langle q\nabla\cdot\vec{v}\rangle - P$ will be positive and an anomalous positive moisture tendency will occur. If anomalous precipitation is greater than vertically-integrated anomalous moisture convergence, $-\langle q\nabla\cdot\vec{v}\rangle - P$ will be negative and moisture will decrease in the column. The term $-\langle q\nabla\cdot\vec{v}\rangle - P$ is generally out of phase with the vertically-integrated moisture tendency, which suggests that vertically-integrated moisture convergence anomalies and precipitation anomalies attempt to eliminate growing (shrinking) moisture anomalies by decreasing (increasing) $-\langle q\nabla\cdot\vec{v}\rangle' - P'$.

Vertically-integrated 30-90 day zonal moisture advection anomalies and evaporation anomalies are small when averaged in the trigger region. Although $-\langle u \frac{\partial q}{\partial x} \rangle'$ has a small average amplitude in the trigger region, closer inspection of this term reveals significant positive vertically-integrated zonal moisture advection anomalies in the trigger region in Phases 7 and 8. In particular, the zonal part of the flow fluxes moisture across a short dip in the TPW gradient near (15°N, 25°E) in Figure 3.6.

4.3. Meridional Moisture Advection

The vertically-integrated meridional moisture advection plays the strongest role in explaining the moisture tendency anomalies observed in Section 4.1. Upon closer inspection of Figures 3.5 and 4.1, the positive moisture tendency anomalies in Phases 6-7 are adjacent to the sharp meridional TPW gradient in the trigger region. Anomalous southerly flow would flux anomalously high moisture values into the trigger region, contribute to growing moisture anomalies and serve to precondition the troposphere for convection.

The vertically-integrated, 30-90 day ERAi meridional moisture advection anomalies are plotted in Figure 4.4 as a function of MJO phase. Here, positive values are indicative of growing moisture anomalies. Generally, $-\langle v \frac{\partial q}{\partial y} \rangle$ anomalies correlates quite well with the moisture tendency. In Phases 5-7, significant positive anomalies are located throughout the trigger region, which is due to anomalous southerly flow acting across the TPW gradient. Figures 3.5 and 3.16 support this claim, specifically showing how southerly anomalies are located near the boreal mean TPW gradient. The $-\langle v \frac{\partial q}{\partial y} \rangle$ anomalies tend to propagate downstream as well, as significant values extend further

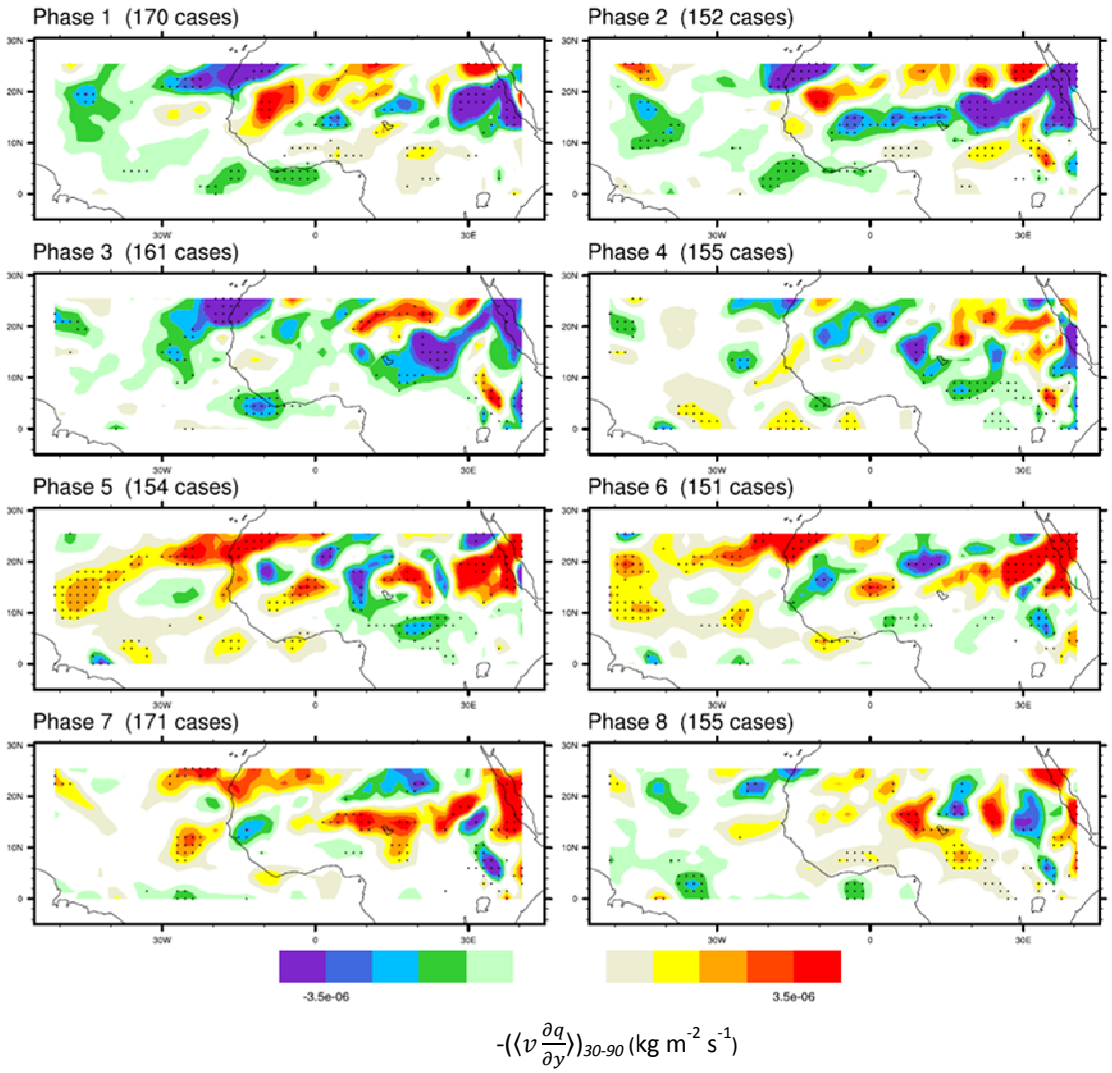

Figure 4.4. MJO phase composites of vertically-integrated ERAi anomalous 30-90 day meridional moisture advection for June-September. The scale is given by the color bar. The shading interval is 7x10^{-7} kg m^{-2} s^{-1}. The dots represent significant data points at the 95% confidence interval.

west with each phase. It is clear that anomalous meridional advection is more than enough to explain the moisture tendency in the trigger region in Phases 5-7. By Phase 8, the trigger region is almost completely devoid of significant and positive $-\langle v\frac{\partial q}{\partial y}\rangle$ anomalies, which are now focused to the west of the trigger region and in a narrow strip to the south of the AEJ. Importantly, opposite-signed advection anomalies occur in advance of the dry phase in the triggering region (Phases 1-3). Initial investigation into

linearized -$\langle v\frac{\partial q}{\partial y}\rangle$ anomalies suggests that meridional wind anomalies advect moisture across boreal mean TPW gradient (-$\langle v'\frac{\partial \bar{q}}{\partial y}\rangle$). Despite this observation, analysis of all linearized terms must be performed to understand relative contributions to total -$\langle v\frac{\partial q}{\partial y}\rangle$ anomalies.

Like the moisture tendency, meridional moisture advection may be filtered by zonal wavenumber to analyze the contribution of large-scale disturbances associated with eastward and westward zonal wavenumbers to the total 30-90 day anomalies. Figure 4.5 shows a strong relationship between the large-scale and total anomalies, especially within the trigger region. Figure 4.5a suggests that much of the signal is produced by anomalies with eastward zonal wavenumbers, although anomalies with westward zonal wavenumbers also make important contributions. These 30-90 day anomalies with eastward zonal wavenumbers are almost twice as large as those for westward zonal wavenumbers and strongly dictate the large-scale anomalies. Large-scale 30-90 day -$\langle v\frac{\partial q}{\partial y}\rangle$ anomalies describes most of the total anomalies, which is supported by Figure 4.5d and is achieved through a balance of anomalies associated with eastward- and westward-propagating disturbances. Importantly, the large-scale and total -$\langle v\frac{\partial q}{\partial y}\rangle$ anomalies are also strongly related in the land and ocean regions. Clearly, the -$\langle v\frac{\partial q}{\partial y}\rangle$ anomalies associated with eastward zonal wavenumbers dominates in these regions as well, with westward-propagating disturbances generally being out of phase with the total anomalies.

Meridional moisture advection anomalies support the moisture tendency anomalies witnessed in the previous section. In particular, anomalous southerly flow

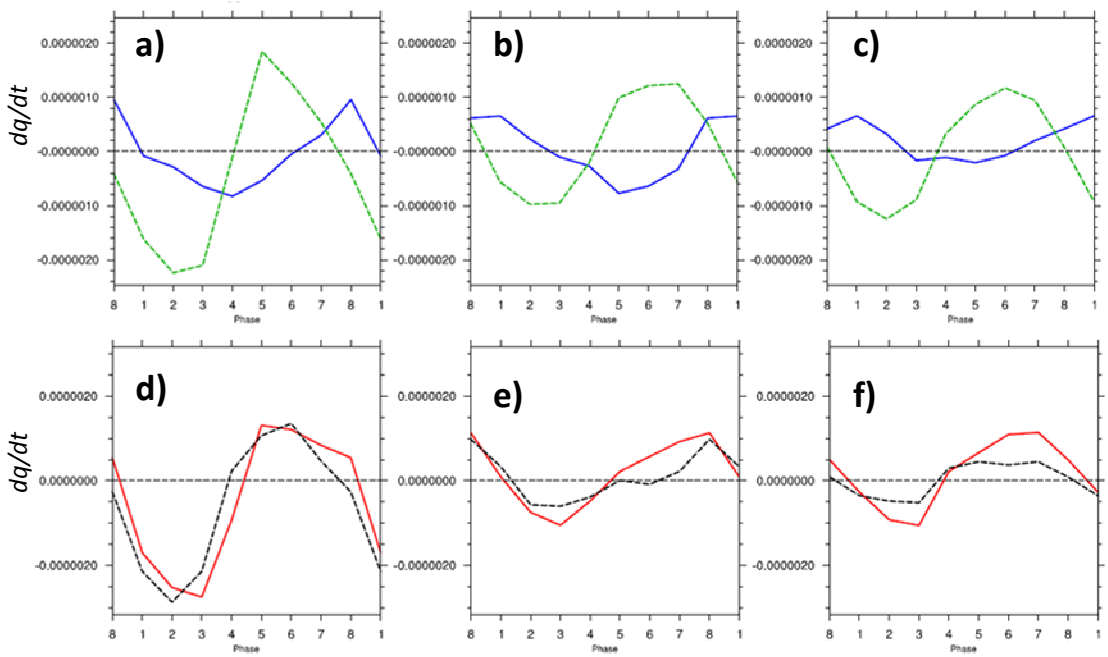

Figure 4.5. Convective box line plots for vertically-integrated ERAi 30-90 day meridional moisture advection anomalies. (a-c) show how $\langle v\frac{\partial q}{\partial y}\rangle$ evolves as a function of phase for eastward (green dashed) and westward (solid blue) zonal wavenumbers. (d-f) illustrate how well the 30-90 day $\langle v\frac{\partial q}{\partial y}\rangle'$ anomalies with wavenumbers [-10, 10] (red solid) match up with the total 30-90 day anomalies (black dashed). The trigger box is shown in a) and d). The land box is shown in b) and e). The ocean box is shown in c) and f). Values are $\langle v\frac{\partial q}{\partial y}\rangle'$ averaged for each phase over the three regions of interest. The units are kg m^{-2} s^{-1}.

(Figure 3.15) fluxes anomalously high moisture values down the mean gradient (Figure 3.6) and into the trigger region. Filtering by zonal wavenumber reveals that eastward-propagating disturbances are mostly responsible for the total -$\langle v\frac{\partial q}{\partial y}\rangle$ anomalies for all locations in tropical north Africa and the tropical east Atlantic. However, the processes responsible for the observed horizontal advection are still unclear.

5. Eddy Kinetic Energy Budget

The vertically-integrated eddy kinetic energy (EKE) budget is important for diagnosing regions of wave growth. With convincing evidence of upstream convective disturbances on intraseasonal timescales, investigation of the vertically-integrated EKE budget provides insight as to what processes contribute to AEW growth may occur over tropical north Africa. While positive moisture anomalies are favorable for enhanced deep convection, they do not directly describe AEW growth. The EKE budget explains how distinct processes contribute to or oppose the calculated EKE tendency. These processes include barotropic conversion, EKE advection, conversion of eddy available potential energy (EAPE) to EKE, the generation or destruction of EKE by local convergence or divergence of eddy geopotential flux, and frictional dissipitation. The vertically-integrated EKE budget equation is given by

$$\langle\frac{\partial KE}{\partial t}\rangle = -\langle\overline{\boldsymbol{V}_h'(\boldsymbol{V}'\cdot\nabla)\overline{\boldsymbol{V}_h}}\rangle - \langle\overline{\boldsymbol{V}}\cdot\nabla\overline{KE}\rangle$$

$$-\langle\overline{\boldsymbol{V}'\cdot\nabla KE}\rangle - \langle\frac{R}{p}\overline{\omega'T'}\rangle - \langle\nabla\cdot(\overline{\boldsymbol{V}'\Phi'})\rangle - D, \qquad (5.1)$$

where $KE \equiv \overline{\boldsymbol{V}_h'^{\,2}}/2$ is the horizontal EKE, $\Phi \equiv gz$ is the geopotential height, $\boldsymbol{V}_h$ is the horizontal wind, $\boldsymbol{V}$ is the vector wind, and D is the EKE dissipation term, which is calculated as a residual. Anomalies are from the 5-day running mean. The term on the left side of (5.1) is the EKE tendency, and represents the time-rate of change of EKE.

Here, the EKE tendency is calculated as shown and not assumed to be zero as in other studies (Lau and Lau 1992). The first term on the right side of (5.1) denotes barotropic conversion, which captures the conversion of mean kinetic energy to EKE. The second term represents advection of EKE by the time-mean flow, while the third term represents advection of EKE by transient fluctuations. The conversion of eddy available potential energy (EAPE) to EKE through the rising/sinking motion of warm/cold air parcels is denoted by the fourth term on the right side of (5.1). Dominant sources of EAPE, which are included in the EAPE budget (not shown), are diabatic heating and baroclinic conversion. Although further investigation into the EAPE budget is necessary to diagnose the relative contributions of diabatic heating and baroclinic conversion, both are important sources of EAPE that may be converted to EKE. The fifth term describes the generation or destruction of EKE by local convergence or divergence of eddy geopotential flux. The last term represents the residual, which, specifically, is the net generation or dissipation of EKE by frictional and other subgrid-scale effect. In this analysis, the residual is calculated as the remainder to balance the budget and may also include analysis increments and errors in calculating other budget terms.

The EKE budget is crucial to the determination of where and how AEWs acquire energy. Essentially, AEWs may grow via barotropic conversions, conversion of EAPE to EKE, flux convergence from geopotential height anomalies, or EKE advection. The EKE advection and $-\langle\nabla\cdot(\overline{\boldsymbol{V}'\Phi'})\rangle$ terms produce very noisy and low amplitude fields. Consequently, these two terms are not as important as other sources or sinks of EKE over northern Africa and the eastern Atlantic, and are consequently not discussed in this section.

5.1. Low-Level EKE

The low-level EKE is representative of AEWs. In particular, the ERAi 700 hPa EKE is analyzed due to the proximity of this level to the AEJ. The boreal mean ERAi 700 hPa EKE, shown in Figure 5.1, provides insight as to where AEW activity is likely to occur from June to September. The maximum boreal mean 700 hPa EKE is located at (13°N, 23°W), which is in the tropical east Atlantic, or just offshore from west Africa. This maximum EKE is greater than 9 m^2 s^{-2}. Although EKE values decrease as one moves east over tropical north Africa, an axis of higher EKE values extends along 9°N throughout this region. The higher values of EKE are indicative of high AEW activity and growth on the south side of the AEJ. However, the 5 m^2 s^{-2} contour also expands in latitude over northern Africa, which may be suggestive of the northern AEW track (Pytharoulis and Thorncroft 1995). Eddy activity to the south of the AEJ is more prominent to the east of Greenwich than activity to the north of the AEJ. Over the Atlantic, the EKE contours slope to the west-northwest, which is consistent with emerged easterly waves traveling around the subtropical ridge.

ERAi 30-90 day 700 hPa EKE anomalies explain how AEWs change in amplitude over tropical north Africa on MJO timescales. In Figure 5.2, 30-90 day 700 hPa EKE anomalies are composited for each MJO phase. In Phase 1, positive 30-90 day EKE anomalies in excess of 0.8 m^2 s^{-2} are located in tropical west Africa, which are coincident with the wet phase. Significant low-level $EKE_{30\text{-}90}$ anomalies span from the equator to 12°N and from 10°W to 12°E. Additionally, significant positive $EKE_{30\text{-}90}$ anomalies are positioned in the trigger region and first appear in Phases 7 and 8. This reinforces the role for the trigger region in seeding the AEJ to support subsequent downstream EKE and

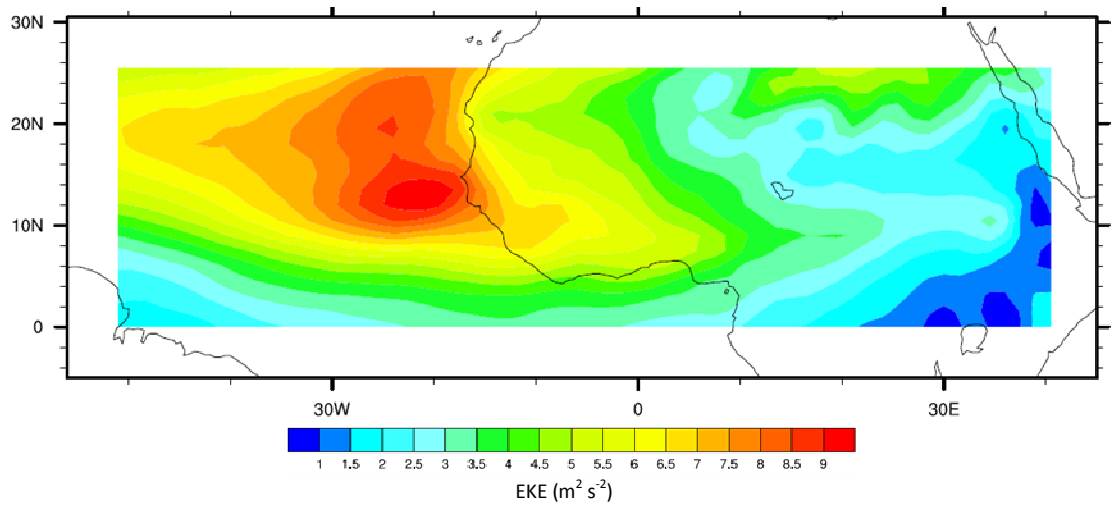

Figure 5.1. June-September mean ERAi 700 hPa EKE. The shading is given by the color bar and the contour interval is 0.5 m^2 s^{-2}.

convection anomalies. The $EKE_{30\text{-}90}$ maximum that occurs in Phase 2 lags the convective maximum by one phase (compare to Figure 3.1). Phase 2 features a more zonally expansive envelope of significant 30-90 day EKE anomalies, with significant anomalies from 28°W to 23°E. Although no significant anomalies exist west of 30°W, the EKE anomalies denote an easterly wave and TC track curving to the northwest from (12°N, 35°W) to (24°N, 48°W). By Phase 3, EKE anomalies are still high but have shifted to the west, which is indicative of AEW growth shutting down and AEW activity propagating downstream. The 30-90 day 700 hPa EKE is anomalously negative in Phase 5, suggesting a suppression of AEW activity that corresponds with negative convective anomalies (Figure 3.1). Importantly, suppressed EKE anomalies first appeared in the trigger region in Phases 3-4, indicating suppressed precursor disturbances there. In fact, the suppression of AEW activity could be more important than the enhancement. Positive 30-90 day 700 hPa EKE anomalies exist within the trigger region in Phase 8 that may be indicative of upstream precursor disturbances that seed the AEJ. These

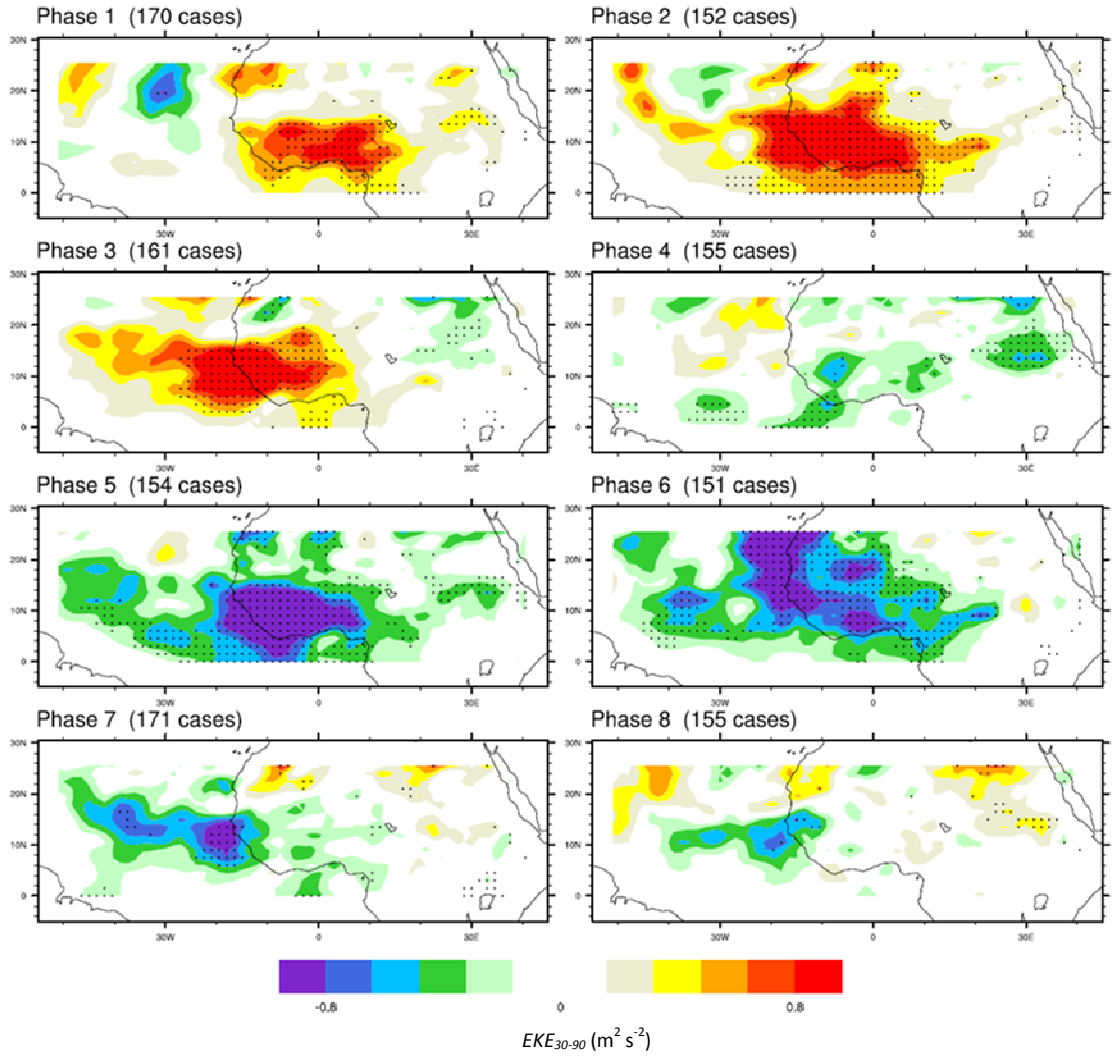

Figure 5.2. MJO phase composites of ERAi anomalous 30-90 day 700 hPa EKE for June-September. The scale is given by the color bar. The shading interval is 0.16 $m^2 s^{-2}$. The dots represent significant data points at the 95% confidence interval.

anomalies indicate upstream wave initiation and growth. The EKE budget is now analyzed in order to study how the sources and sinks of transient wave energy vary on intraseasonal timescales and how the trigger region is consequently affected.

5.2. EKE Tendency

The EKE tendency represents the time-rate of change of EKE. On intraseasonal timescales, variations of the EKE tendency with respect to MJO phase highlight when

EKE is increasing or decreasing with respect to time. In Figure 5.3, the vertically-integrated anomalous ERAi 30-90 day EKE tendency is computed as in (5.1). Clearly, the strongest intraseasonal EKE tendency anomalies are located offshore, which has implications for both the tropical Atlantic and tropical north Africa. Significant positive EKE tendency anomalies achieve maximum amplitude (near 0.01 m^2 s^{-2}) over the Atlantic in Phase 1. The minimum $\langle\frac{\partial KE}{\partial t}\rangle$ anomalies occur in Phase 4, or one phase before the dry phase, which suggests that column EKE decreases in advance of the convective minimum. Negative $\langle\frac{\partial KE}{\partial t}\rangle$ anomalies occur in Phases 3-5, with a sense of westward propagation. In Phases 6-8, significant and positive $\langle\frac{\partial KE}{\partial t}\rangle$ anomalies exist over topical north Africa, including the trigger region. The fact that EKE tendency anomalies grow in the trigger region in advance of the convective maximum supports the notion of upstream AEW growth. Likewise, EKE tendency is negative in the trigger region in Phases 1 and 2, which may stifle the generation of upstream precursor disturbances there.

5.3. Barotropic Conversion

Barotropic conversion represents the exchange between mean kinetic energy (MKE) and EKE. Barotropic conversion is positive in the EKE budget when eddy disturbances grow at the expense of MKE. In particular, MKE is converted to EKE when transient waves have an appropriate tilt against the background horizontal wind shear. For example, AEWs on the south of the AEJ tilt from southwest to northeast with latitude, or against the increasingly easterly winds with latitude. Waves on the north side of the AEJ tilt from southeast to northwest, or against the decreasingly easterly winds with latitude (Thorncroft and Hoskins 1994; Hall et al. 2006). Barotropic conversions are

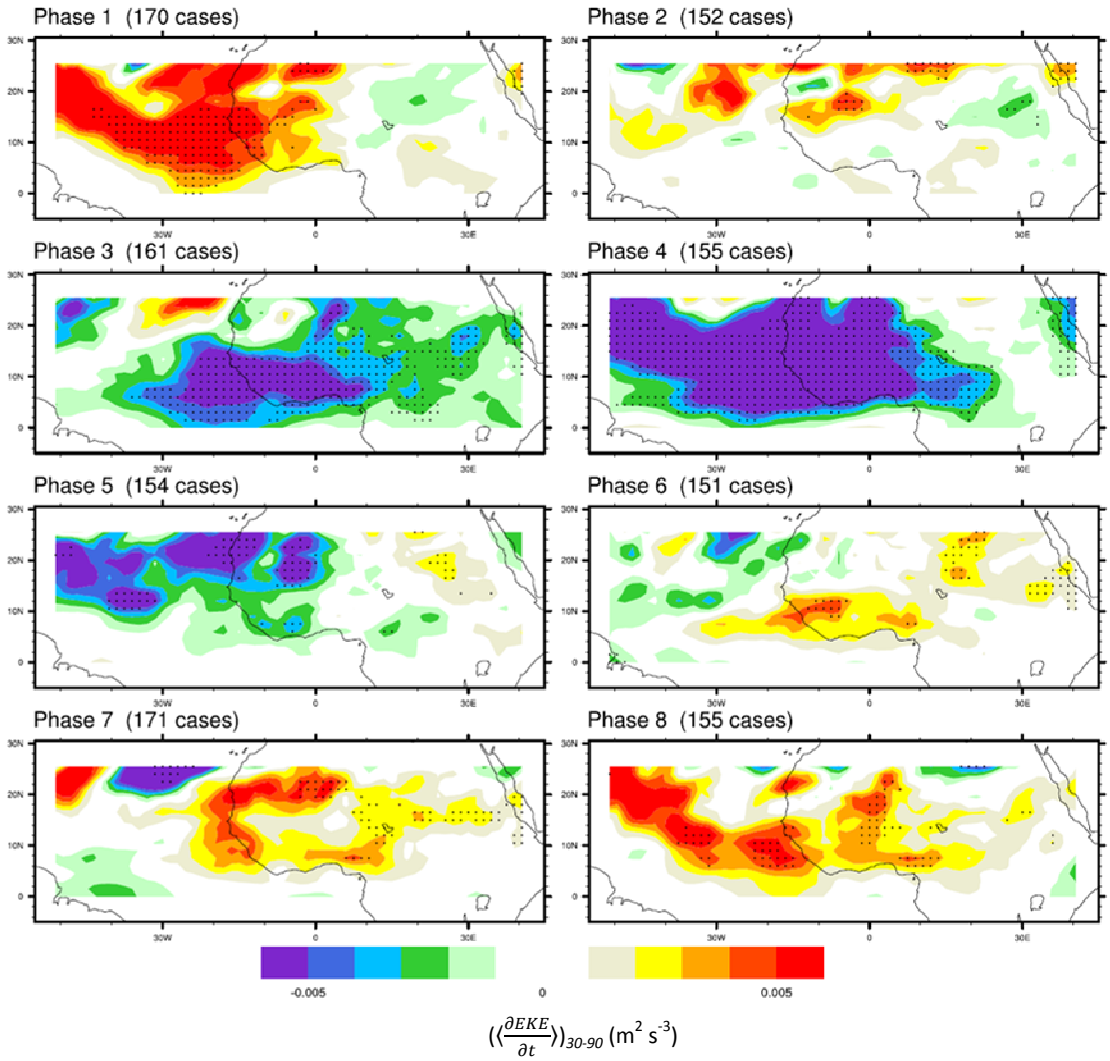

Figure 5.3. MJO phase composites of the vertically-integrated ERAi anomalous 30-90 day EKE tendency for June-September. The scale is given by the color bar. The shading interval is 1x10^{-3} m^2 s^{-3}. The dots represent significant data points at the 95% confidence interval.

extremely important for AEW maintenance within the AEW development region and along the AEJ. The AEJ is accompanied by a reversal in the meridional isentropic potential vorticity gradient, which satisfies the Charney-Stern necessary condition for barotropic-baroclinic instability (Charney and Stern 1962; Burpee 1972). Thus, waves may preferentially tilt against the flow in order to grow via barotropic conversions over tropical north Africa.

Figure 5.4 shows vertically-integrated ERAi 30-90 day barotropic conversion anomalies for the eight MJO phases. Phase 1 exhibits anomalous barotropic conversion maxima within the land and ocean regions, respectively, with values on the order of 0.04 $m^2\ s^{-3}$. Specifically, these maxima are located within strong meridional wind shear on the south side of the AEJ (Figure 3.21). The west African coast is void of anomalies in all phases and is located between the two maxima in Phase 1. Significant positive barotropic conversion anomalies are indicative of enhanced AEW growth, which coincides with the convective enhancement found in Phase 1 of other variables. Conversely, Phase 5 shows significant negative barotropic conversion anomalies near the AEJ denoting a suppression of AEW growth. Importantly, significant positive $-\langle\overline{\boldsymbol{V}_h'(\boldsymbol{V}'\cdot\nabla)\overline{\boldsymbol{V}}_h}\rangle$ anomalies are located within the trigger region in Phase 8, which suggests that barotropic conversion may aid precursor disturbances and AEW initiation. In fact, upstream 30-90 day $-\langle\overline{\boldsymbol{V}_h'(\boldsymbol{V}'\cdot\nabla)\overline{\boldsymbol{V}}_h}\rangle$ anomalies are associated with an eastward extension of the AEJ into the trigger region that initiates in Phase 7 and persists until Phase 2 (Figure 3.21). Upstream barotropic conversion in Phases 7 and 8 provides evidence of AEW growth in advance of the convective maximum in Phase 1.

Intraseasonal 700 hPa $-\langle\overline{\boldsymbol{V}_h'(\boldsymbol{V}'\cdot\nabla)\overline{\boldsymbol{V}}_h}\rangle$ anomalies, which are just beneath the mean level of the AEJ, display a more spatially coherent signal than the vertically-integrated term (Figure 5.5). Barotropic conversion tends to maximize in the lower troposphere, which justifies the selection of the 700 hPa level. The most important feature to note is the significant $-\langle\overline{\boldsymbol{V}_h'(\boldsymbol{V}'\cdot\nabla)\overline{\boldsymbol{V}}_h}\rangle$ anomalies in the trigger region of Phase 8, which provides strong evidence of upstream eddy growth, which may be important to AEW initiation.

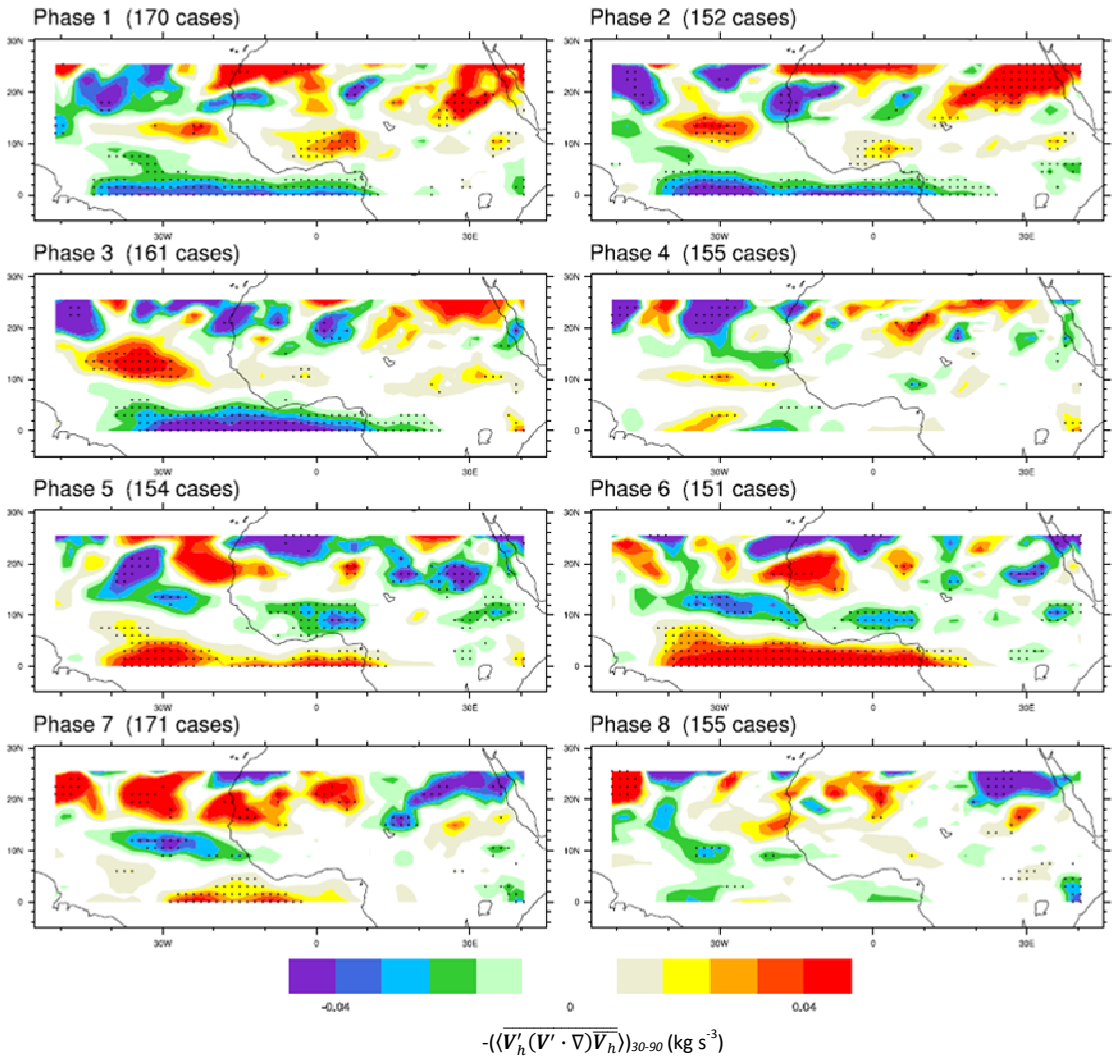

Figure 5.4. MJO phase composites of the vertically-integrated ERAi anomalous 30-90 day barotropic conversion for June-September. The scale is given by the color bar. The shading interval is 8x10^{-3} kg s^{-3}. The dots represent significant data points at the 95% confidence interval.

Additionally, the zonal extent of positive barotropic conversion anomalies during Phase 1 spans more than 50° of longitude.

Overall, both the 700 hPa and vertically-integrated $-\overline{v_h'(v'\cdot\nabla)\overline{v}_h}$ anomalies produce behavior consistent with supporting the EKE maximum in Phases 2 and 3 and EKE minimum in Phases 5 and 6 (see Figure 5.2). Most importantly, significant $-\overline{v_h'(v'\cdot\nabla)\overline{v}_h}$ anomalies populate the trigger region, indicative of growing upstream precursor

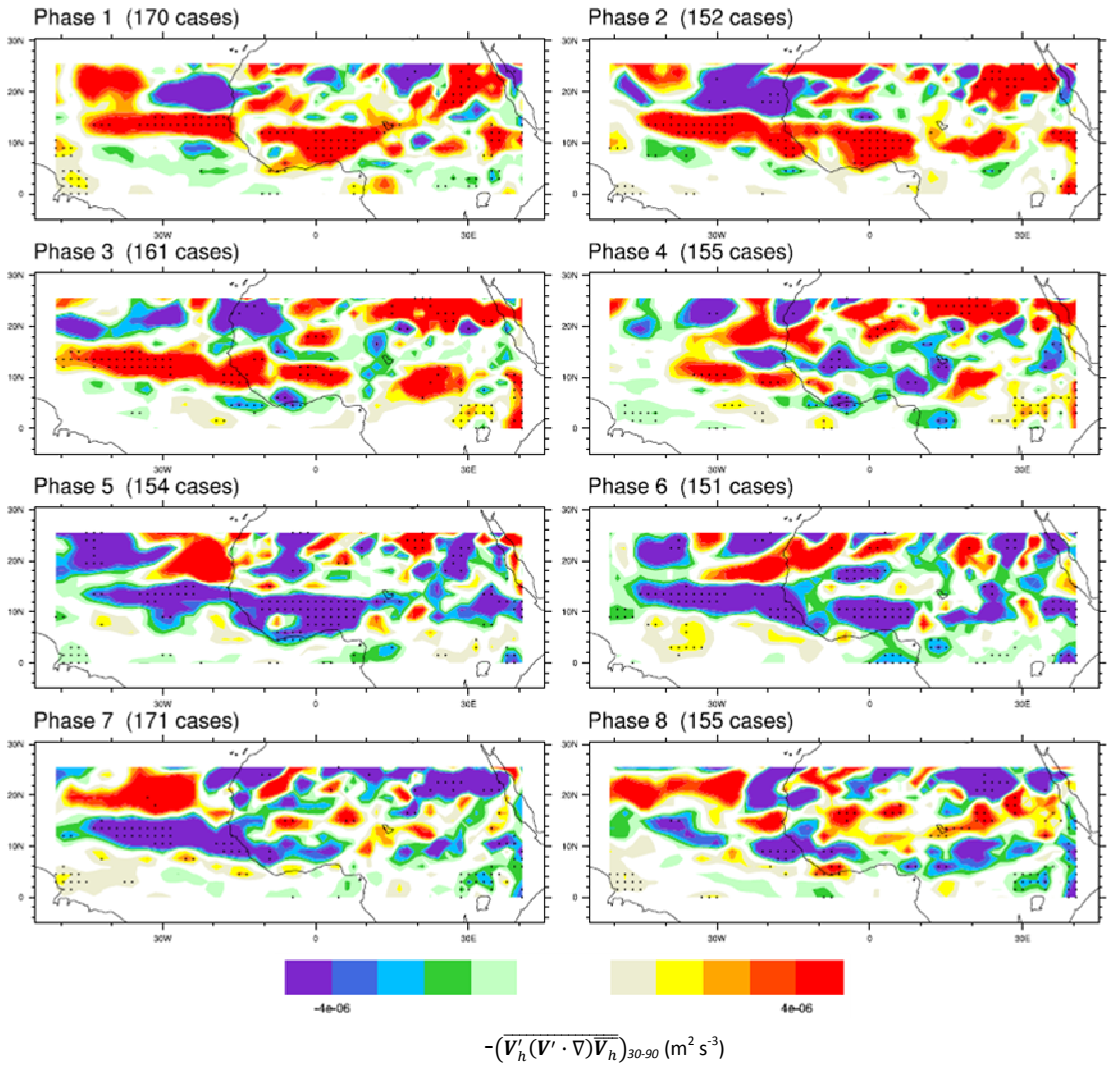

Figure 5.5. MJO phase composites of the ERAi anomalous 30-90 day 700 hPa barotropic conversion for June-September. The scale is given by the color bar. The shading interval is 8×10^{-7} m^2 s^{-3}. The dots represent significant data points at the 95% confidence interval.

disturbances on intraseasonal timescales. Barotropic conversion is enhanced over tropical north Africa due to stronger shear in the AEJ and to an eastward extension of the jet. Consequently, the enhancement of vertically-integrated and 700 hPa 30-90 day barotropic conversion suggests that stronger disturbances are propagating along the AEJ.

5.4. EAPE Conversion

While barotropic conversion makes a significant contribution to AEW initiation and growth on intraseasonal timescales, the amplitude is only half that of the EAPE-to-EKE conversion term. The EAPE conversion term represents the conversion of EAPE-to-EKE through the rising (sinking) of warm (cold) air parcels (Lau and Lau 1992). EAPE is predominantly generated through both baroclinic energy conversions associated with the AEJ, and through the positive covariance of diabatic heating and temperature anomalies in AEWs (Thorncroft et al. 2008)

The intraseasonal variability of EAPE-to-EKE conversion is analyzed in Figure 5.6. With the maximum amplitude around 0.08 kg s^{-3}, the EAPE-to-EKE conversion is about twice as large as the barotropic conversion term. In Phase 1, the pattern of $-\langle\frac{R}{p}\overline{\omega' T'}\rangle$ anomalies are quite similar barotropic conversion, with a maximum in the land region and a separate maximum over the eastern Atlantic within the ocean region. Thus, EAPE-to-EKE and barotropic conversions give evidence of enhanced AEW growth in Phase 1, with EAPE-to-EKE conversions accounting for the majority of the observed EKE growth. Phases 8-2 also feature significant $-\langle\frac{R}{p}\overline{\omega' T'}\rangle$ anomalies in the trigger region, which suggests the importance of EAPE-to-EKE conversion to upstream convective anomalies before and during the wet phase. The strengthened jet in this region (Figure 3.21) and positive precipitation anomalies (Figure 3.4) suggest that both diabatic heating-temperature correlations and baroclinic conversion may support EAPE generation and subsequent conversion to EKE in this region. EAPE-to-EKE conversion supports the growth of strong precursor disturbances that may amplify as they propagate

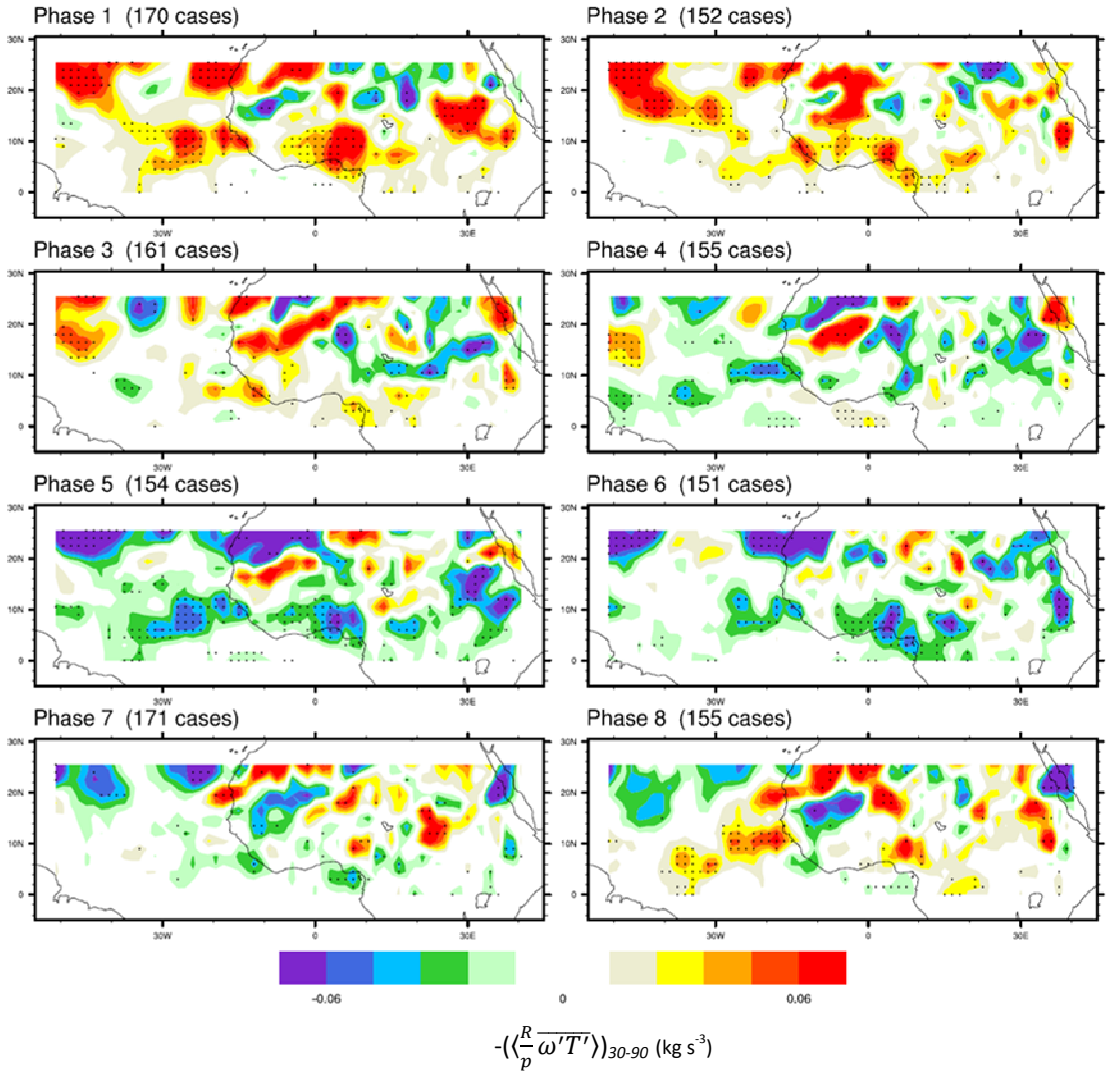

Figure 5.6. MJO phase composites of the vertically-integrated ERAi anomalous 30-90 day EAPE conversion for June-September. The scale is given by the color bar. The shading interval is 1.2x10^{-2} kg s^{-3}. The dots represent significant data points at the 95% confidence interval.

to the west along the AEJ. Conversely, Phases 3-5 suggest a suppression of AEW growth in the trigger region, suppressing downstream wave growth.

The dependence of EKE and subsequent AEW growth on EAPE-to-EKE conversion is undeniable. Further investigation into the EAPE budget is necessary in order to understand the relative contributions of diabatic heating and baroclinic conversions. Baroclinic conversions represent a conversion from mean available potential energy (MAPE) to eddy available potential energy (EAPE). The most likely

scenario is that upstream diabatic heating creates EAPE, which, by conversion to EKE, initiates AEW growth. The opposite occurs in advance of suppressed convective periods, when upstream EAPE-to-EKE conversion anomalies are negative and AEW wave growth is suppressed. As the waves grow, they produce more diabatic heating while they propagate to the west. Additionally, the reversal in the meridional IPV gradient encourages substantial baroclinic conversions in the AEW development region, which are aided through the strong growing disturbances that also creates EAPE. These terms are supported by relatively weaker barotropic conversion anomalies.

6. Summary and Discussion

This study investigates how the Madden-Julian Oscillation (MJO) modulates convective activity, the moisture budget and easterly wave activity in the west African monsoon in boreal summer. Several studies have examined the intraseasonal variability of convection and precipitation anomalies in association with the west African monsoon and African easterly waves (AEWs; Maloney and Shaman 2008; Matthews 2004; Janicot et al. 2009; Sultan et al. 2003), although the analysis performed here provides greater detail. Specifically, a diverse set of data products was utilized to make a more convincing argument of how related fields vary on MJO timescales. Analysis of convection, the moisture budget, and the eddy kinetic energy (EKE) budget support the upstream initiation of convection and AEWs ahead of the wet phase over tropical north Africa (defined as Phase 1). Large-scale components of the flow, including Kelvin and Rossby waves, describe most of the total intraseasonal anomalies, as evidenced by several convective averaging line plots. The main conclusions of the study may be summarized as:

- Intraseasonal brightness temperature and precipitation anomalies support maximum convection in Phase 1 (wet phase) and minimum convection in Phase 5 (dry phase) over tropical north Africa.

- Cold (warm) 400 hPa $T_{30\text{-}90}$ anomalies in Phase 8 (Phase 3) reduce (increase) the static stability in the trigger region, making the troposphere more (less) favorable for upstream convection.
- Anomalous ascent populates the trigger region in Phases 7-8, which supports the onset of precursor convective disturbances in advance of the wet phase. Anomalous descent in Phase 4 suppressed convection before the dry phase.
- The African easterly jet (AEJ) extends eastward into the trigger region in Phases 7-8, strengthening the PV reversal in the same location and supporting more upstream wave growth. Conversely, a shortening of the AEJ in Phases 3-4 may suppress upstream wave growth.
- Positive (negative) upstream moisture anomalies are induced by positive (negative) $-\langle v\frac{\partial q}{\partial y}\rangle$ anomalies in Phases 5-7 (Phases 1-3). Increased $-\langle v\frac{\partial q}{\partial y}\rangle$ supports a corresponding increase in total precipitable water anomalies in the trigger region during Phases 7-8.
- Positive (negative) EKE tendency anomalies near the trigger region supports wave growth (decay) in Phases 7-8 (Phases 3-4).
- EAPE-to-EKE conversion anomalies are positive (negative) in the trigger region in Phases 7-8 (Phases 3-4), which enhances (suppressed) wave growth. This term includes the effects of diabatic heating and baroclinic conversion, and is also important for downstream maintenance of AEWs in Phases 1-2.
- Barotropic conversion anomalies, although not as strong as EAPE-to-EKE conversion anomalies, enhance (suppress) AEW growth at approximately the same times and locations as EAPE-to-EKE conversion.

This study lends support to the idea that periods of MJO-related convection and AEW activity in the west African monsoon region are first triggered over the Darfur mountains and Ethiopian highlands. Another point of emphasis is the initiation of strong upstream convection and EKE anomalies by large-scale eastward and westward components of the 30-90 day flow and the corresponding maintenance of those features with propagation down the AEJ. The term "large-scale" refers zonal wavenumbers between -10 and 10, which includes contributions from Kelvin and Rossby waves on 30-90 day timescales. Since upstream convection may be induced by topography, including the Darfur Mountains and Ethiopian highlands (Burpee 1972; Carlson 1969; Thorncroft et al. 2008), an area near the AEJ entrance, which is known as the "trigger region" and is located to the northeast of Lake Chad, is monitored for evidence of precursor convective events and their relationship to the large-scale flow. Regions over tropical west Africa ("land region") and the tropical east Atlantic ("ocean region") help to assess the evolution of convection and AEWs as they propagate to the west along the AEJ.

An MJO index was created by performing combined EOF analysis on the 30-90 day CLAUS brightness temperature, 30-90 day ERAi 850 hPa zonal wind and 30-90 day ERAi 200 hPa zonal wind. This index, which includes the amplitude and phase of the MJO for each day from 1989 to 2005, is similar to the one described in Wheeler and Hendon (2004), although they use outgoing longwave radiation as a proxy for convection instead of brightness temperature. With the help of the MJO index, significant MJO events were isolated, and composite fields were created that consisted of eight MJO phases.

Composite intraseasonal brightness temperature (Figure 3.1) and precipitation (Figure 3.4) anomalies reveal significant convection anomalies that maximize (minimize) over tropical west Africa in Phase 1 (Phase 5). These phases are nicknamed the "wet" and "dry" phases, respectively. The enhancement of convection over tropical west Africa coincides with the initiation of MJO convection in the Indian Ocean, which is supported by findings in Janicot et al. (2009). Negative (positive) upstream 30-90 day brightness temperature anomalies, which appear near the trigger region in Phase 7 (Phase 3) and intensify by Phase 8 (Phase 4), occur 5-10 days before the wet (dry) phase. Thus, the timing of large-scale components of the flow, including Kelvin and Rossby waves, as they arrive in Africa is crucial for determining the exact role of the MJO in initiating anomalies near the trigger region, and maintaining anomalies in the land and ocean regions.

Upper-tropospheric ERAi vector wind anomalies retain Kelvin wave signatures when filtered for eastward zonal wavenumbers (Figure 3.24) and Rossby wave signatures when filtered for westward zonal wavenumbers (Figure 3.25). A Kelvin wave front forced by positive MJO heating anomalies in the Indian Ocean produces anomalous westerlies at 200 hPa along the equator. These westerlies propagate quickly to the east at approximately 15 m s^{-1} and arrive in tropical Africa in Phase 5. Thus, the positive phase of the Kelvin wave is associated with the dry phase over tropical north Africa. Negative MJO heating anomalies in the Indian Ocean in Phase 5 are produced anomalous 200 hPa easterlies along the equator. The anomalous easterlies reach tropical Africa in Phase 1, indicating that the negative phase of the Kelvin wave arrives in coincidence with the wet phase over tropical north Africa.

Mid-tropospheric temperature anomalies associated with MJO convection support this claim. Positive eastward-propagating ERAi 30-90 day 400 hPa temperature anomalies (Figure 3.13), which are associated with the positive phase of the Kelvin wave, initiate in the Indian Ocean in Phase 1 and arrive at the west African coast (15°W) in Phase 5. Positive upper-tropospheric temperature anomalies represent an increase in the static stability due to a decreased lapse rate, and support suppressed convection over tropical north Africa in Phase 5. Conversely, negative 30-90 day 400 hPa temperature anomalies, which propagate with the negative phase of the Kelvin wave, reduce the static stability in tropical north Africa in Phase 1 (Figure 3.11). Eastward-propagating negative (positive) off-equatorial 30-90 day 400 hPa temperature anomalies exist near the trigger region in Phase 8 (Phase 4), but are not associated with the negative (positive) phase of the Kelvin wave that arrives in Phase 1 (Phase 5). Negative (positive) off-equatorial anomalies might be indirectly associated with the previous positive (negative) Kelvin wave. Maloney and Sobel (2007) also noted these off-equatorial temperature anomalies in association with Kelvin waves, and further analysis is necessary to understand the mechanism responsible for this signal. Regardless, eastward-propagating components of the flow support positive (negative) convective anomalies near the AEW development region in the wet (dry) phase, in addition to enhancing (suppressing) upstream convection in Phase 8 (Phase 4) in association with off-equatorial temperature anomalies.

Rossby wave signatures that propagate from the Indian Ocean are observed in the large-scale westward components of the 200 hPa vector wind (Figure 3.25). An upper-tropospheric anticyclone is observed over India along with the onset of MJO convection in the Indian Ocean. This anticyclone is a response to growing convective anomalies

over India and, also, takes the appearance of a Rossby wave associated with heating along the equator. By Phases 3-4, the anticyclone is elongated to the west, which is consistent with propagation into tropical east Africa. Conversely, an upper-tropospheric cyclone forms in Phase 5 in association with a suppression of the Indian monsoon and propagates into tropical east Africa by Phases 7-8. The Rossby cyclone at 200 hPa may induce rising motion on its westward flank as it propagates to the west. Intraseasonal vertical velocity anomalies for westward components of the flow support this notion (Figure 3.15a), with ascent in the trigger region during Phases 7-8 and descent during Phases 3-4.

Low-level intraseasonal vector wind anomalies reveal the variability of west African monsoon flow, which is not enhanced prior to the wet phase. Low-tropospheric vector wind anomalies become westerly over the Atlantic and exhibit anomalous onshore flow beginning in Phase 1 (Figure 3.17). The opposite is true in Phase 5. An isolated area of anomalous southerly flow is observed near the trigger region in Phases 6-8, which is responsible for positive meridional moisture advection across the sharp total precipitable water (TPW) gradient (Figure 4.3). Since meridional moisture advection dominates the moisture budget in the trigger region (Figure 4.5), moisture anomalies grow within the trigger region, which supports the onset of strong upstream convective disturbances in advance of the wet phase. Initial investigation of the term $-v' \frac{\partial \bar{q}}{\partial y}$ suggests that the anomalous wind acting upon the mean meridional moisture gradient describes most of the $-v \frac{\partial q}{\partial y}$ variability observed in Figure 4.4, although further analysis is required to determine the relative role of all linearized $-v \frac{\partial q}{\partial y}$ terms.

Intraseasonal meridional moisture advection anomalies in the trigger region (Figure 4.4a) that are filtered to retain only eastward components maximize (minimize) in Phase 5 (Phase 2). On the other hand, intraseasonal meridional moisture advection anomalies in the trigger region filtered to retain the large-scale west components of the flow maximize (minimize) in Phase 8 (Phase 4). Positive meridional moisture advection in the trigger region is produced in Phases 6-8 due to the sum of the large-scale anomalies. Further investigation is necessary to determine how Kelvin and Rossby waves, which are included in the large-scale flow, may induce low-level southerly flow in the trigger region.

An extension of the AEJ to the east during Phases 7-8 (see Figure 3.21) is important for enhancing upstream barotropic conversion, EAPE-to-EKE conversion, and advecting precursor convection events downstream more efficiently. The longer jet in advance of and during the convective maximum over tropical north Africa is characterized by a stronger reversal in the isentropic potential vorticity gradient (Figure 3.22), which is a necessary condition for barotropic-baroclinic instability as suggested by Charney and Stern (1962). Thus, convective anomalies that are initiated upstream grow more rapidly along the extended jet and support unstable wave growth. The extension of the AEJ near the trigger region is mostly due to large-scale eastward components of the flow (Figure 3.23a). Anomalous mid-tropospheric easterlies propagate into tropical Africa from the west and increase the zonal extent of the AEJ in Phases 7-8. Conversely, anomalous mid-tropospheric westerlies propagate into tropical Africa during Phases 3-4 and are responsible for shortening the AEJ and suppressing the growth of upstream convection.

Positive EKE anomalies are generated in the trigger region in Phase 7-8 (Figure 5.2). The extension of the AEJ, as well as the presence of positive convection anomalies, results in increased barotropic conversion and EAPE-to-EKE conversion in the trigger region (Figures 5.4 and 5.6) in Phases 7-8. EAPE-to-EKE conversions consist of diabatic heating and baroclinic conversions, but the relative contributions of each are not understood at this time. Overall, the trigger region experiences enhanced AEW growth in advance of the convective maximum in Phase 1.

In the trigger region, the convective signal in Phases 7-8 is enhanced by the large-scale components of the flow. On the contrary, large-scale components of the flow suppress the convective signal in Phases 3-4. Although most of the discussion has focused on the relationship between the MJO and enhanced convection in tropical north Africa, the suppression of convection in tropical north Africa by the MJO may be of equal importance. Westward-propagating disturbances, including Rossby waves, are responsible for inducing positive meridional moisture advection anomalies, negative anomalous ascent, and positive TPW anomalies in the trigger region before the wet phase. Eastward-propagating disturbances, including Kelvin waves, are more important for inducing positive (negative) convection anomalies during Phase 1 (Phase 5). However, eastward components of the flow may reduce static stability off the equator prior to Phase 1, although the precise mechanism by which this happens requires further study. On intraseasonal timescales, precursor disturbances in the form of convection and EKE anomalies are induced in the trigger region by the large-scale components of the flow. Since the MJO is predictable a few weeks in advance and upstream precursor disturbances will amplify (be suppressed) 5-10 days in advance of the onset of wet (dry)

phase in the west African monsoon, the enhancement or suppression of AEW and TC activity is related to the MJO.

Future work will continue focus on the relationship between the MJO and AEWs. Primitive equation modeling studies will be performed to determine whether jet variations or the strength of precursor disturbances are more important for producing EKE variations associated with the MJO in the west African monsoon system. In particular, the relationship between MJO phase and AEW characteristics and amplitude will be sought out. More in-depth analysis of the contributions of eastward and westward components of the flow is necessary to better understand the independent influence of each on tropical Africa and the MJO influence on this region. Additionally, an in-depth analysis of the EAPE budget is necessary to analyze independent contributions from diabatic heating and baroclinic conversions to wave growth in the trigger region and to the west. It is important to discover when and where diabatic heating or baroclinic conversion dominates the EAPE budget. The goal of future studies is to learn more about the link between AEW variability and the MJO, such that skillful AEW activity forecasts may be created based on the state of the MJO.

References

1. Agudelo, P. A., J. A. Curry, C. D. Hoyos, and P. J. Webster, 2006: Transition between suppressed and active phases of intraseasonal oscillations in the Indo-Pacific warm pool. *J. Climate,* **19,** 5519–5530.

7. Albignat, J. P., and R. J. Reed, 1980: The origin of African wave disturbances during Phase III of GATE. *Mon. Wea. Rev.*, **108,** 1827–1839.

8. Annamalai, H., and J. M. Slingo, 2001: Active/break cycles: Diagnosis of the intraseasonal variability of the Asian Summer Monsoon. *Climate Dyn.*, **18,** 85–102.

9. Bantzer, C. H., and J. M. Wallace, 1996: Intraseasonal variability in tropical mean temperature and precipitation and their relation to the tropical 40–50 day oscillation. *J. Atmos. Sci.*, **53,** 3032–3045.

10. Benedict, J. J., and D. A. Randall, 2007: Observed characteristics of the MJO relative to maximum rainfall. *J. Atmos. Sci.*, 64, 2332-2354.

11. Berrisford P., D. P. Dee, K. Fielding, M. Fuentes, P. Kallberg, S. Kobayashi, S. M. Uppala, 2009: The ERA-Interim Archive. ERA Report Series No. 1, ECMWF, Reading, UK.

12. Brandt, P., G. Caniaux, B. Bourle, A. Laza, M. Dengler, A. Funk, V. Hormann, H. Giordani, and F. Marin, 2010: Equatorial upper-ocean dynamics and their interaction with the West African monsoon. *Atmospheric Science Letters*, in press.

13. Bretherton, C. S., M. E. Peters, and L. E. Back, 2004: Relationships between water vapor path and precipitation over the tropical oceans. *J. Climate,* **17,** 1517–1528.

14. Burpee, R. W., 1972: The origin and structure of easterly waves in the lower troposphere of North Africa. *J. Atmos. Sci.*, **29,** 77–90.

15. Burpee, R. W., 1974: Characteristics of North African easterly waves during the summers of 1968 and 1969. *J. Atmos. Sci.,* **31,** 1556–1570.

16. Burpee, R. W., 1975: Some features of synoptic–scale waves based on a compositing analysis of GATE data. *Mon. Wea. Rev.,* **103,** 921–925.

17. Camargo, S. J., M. C. Wheeler, A. H. Sobel, 2009: Diagnosis of the MJO Modulation of Tropical Cyclogenesis Using an Empirical Index. *J. Atmos. Sci.*, **66**, 3061–3074.

18. Carlson, N., 1969: Synoptic histories of three African disturbances that developed into Atlantic hurricanes. Mon. Wea. Rev., 97, 256–276.

19. Chang, C. P., and H. Lim, 1988: Kelvin-wave CISK: A possible mechanism for the 30–50 day oscillations. *J. Atmos. Sci.,* **45,** 1709–1720.

20. Chao, W. C., 1995: A critique of wave-CISK as an explanation for the 40-50 day tropical intraseasonal oscillation. *J. Meteor. Soc. Japan*, 73, 677-684.

21. Charney, J. G., and M. E. Stern, 1962: On the stability of internal baroclinic jets in a rotating atmosphere. *J. Atmos. Sci.*, **19,** 159–172.

22. Dickinson, M. J., and J. Molinari, 2000: Climatology of sign reversals of the meridional potential vorticity gradient over Africa and Australia. *Mon. Wea. Rev.,* **128,** 3890–3900.

23. Diedhiou, A., S. Janicot, A. Viltard, P. de Felice, and H. Laurent, 1999: Easterly wave regimes and associated convection over West Africa and the tropical Atlantic: Results from NCEP/NCAR and ECMWF reanalyses. *Climate Dyn.,* **15,** 795–822.

24. Emanuel, K. A., 1987: Air-sea interaction model of intraseasonal oscillations in the Tropics. *J. Atmos. Sci.*, 44, 2324-2340.

25. Emanuel, K. A., 1994: *Atmospheric Convection.* Oxford University Press, 580 pp.

26. Emanuel, K. A., J. D. Neelin, and C. S. Bretherton, 1994: On largescale circulations in convecting atmospheres. *Quart. J. Roy. Meteor. Soc.,* **120,** 1111–1143.

27. Frank, N. L., 1969: The “inverted v” cloud pattern—An easterly wave? *Mon. Wea. Rev.,* **97,** 130–140.

28. Fuchs, Z., and D. J. Raymond, 2007: A simple, vertically resolved model of tropical disturbances with a humidity closure. *Tellus*, 59A, 344-354.

29. Gill, A. E., 1980: Some simple solutions for heat-induced tropical circulation. *Quart. J. Roy. Meteor. Soc.,* **106,** 447–462.

30. Gill, A. E., 1982: Studies of moisture effects in simple atmospheric models: The stable case. *Geophys. Astrophys. Fluid Dyn.,* **19,** 119–152.

31. Gu, G., R. F. Adler, G. J. Huffman, and S. Curtis, 2004: African easterly waves and their association with precipitation. *J. Geophys. Res.,* **109,** D04101, doi:10.1029/2003JD003967.

32. Hagos, S. M., K. H. Cook, 2007: Dynamics of the West African Monsoon Jump. *J. Climate,* **20**, 5264–5284.

33. Hall, N. M. J., G. N. Kiladis, and C. D. Thorncroft, 2006: Three-dimensional structure of African easterly waves. Part II: Dynamical modes. *J. Atmos. Sci.,* **63,** 2231–2245.

34. Heckley, W. A., and A. E. Gill, 1984: Some simple solutions to the problem of forced equatorial long waves. *Quart. J. Roy. Meteor. Soc.,* **110,** 203–217.

35. Hendon, H. H. , and M. L. Salby, 1994: The life cycle of the Madden–Julian oscillation. *J. Atmos. Sci.,* **51,** 2225–2237.

36. Hodges, K. I., B. J. Hoskins, J. Boyle, and C. D. Thorncroft, 2003: A comparison of recent reanalysis datasets using objective feature tracking: Storm tracks and tropical easterly waves. *Mon. Wea. Rev.,* **131,** 2012–2037.

37. Hodges, K. I., and C. D. Thorncroft, 1997: Distribution and statistics of African mesoscale convective weather systems based on the ISCCP Meteosat imagery. *Mon. Wea. Rev.,* **125,** 2821–2837.

38. Hsieh, J.-H., and K. H. Cook, 2005: Generation of African easterly wave disturbances: Relationship to the African easterly jet. *Mon. Wea. Rev.,* **133,** 1311–1327.

39. Holton, J. R., 2004: Introduction to dynamic meteorology, *International. Geophysics Series*, **Vol.** 88, fourth edn, Elsevier Academic Press.

40. Houze, R. A., Jr., 1997: Stratiform precipitation in regions of convection: A meteorological paradox? *Bull. Amer. Meteor. Soc.,* **78,** 2179–2196.

41. Hu, Q., and D. Randall, 1994: Low frequency oscillations in radiative-convective systems. *J. Atmos. Sci.*, 51, 1089-1099.

42. Huffman, G. J., R. F. Adler, M. Morrissey, D. T. Bolvin, S. Curtis, R. Joyce, B. McGavock, and J. Susskind, 2001: Global precipitation at one-degree daily resolution from multisatellite observations. *J. Hydrometeor.*, **2,** 36–50.

43. Janicot, S., F. Mounier, S. Gervois, B. Sultan, G. N. Kiladis, 2010: The Dynamics of the West African Monsoon. Part V: The Detection and Role of the Dominant Modes of Convectively Coupled Equatorial Rossby Waves. *J. Climate,* **23**, 4005–4024.

44. Janicot, S., F. Mounier, N. M. J. Hall, S. Leroux, B. Sultan, G. N. Kiladis, 2009: Dynamics of the West African Monsoon. Part IV: Analysis of 25–90-Day Variability of Convection and the Role of the Indian Monsoon. *J. Climate*, 22, 1541–1565.

45. Janicot, S., and B. Sultan, 2001: Intra-seasonal modulation of convection in the West African monsoon. *Geophys. Res. Lett.*, 28, 523–526.

46. Janicot, S., Thorncroft, C. D., Ali, A., Asencio, N., Berry, G., Bock, O., Bourles, B., Caniaux, G., Chauvin, F., Deme, A., Kergoat, L., Lafore, J.-P., Lavaysse, C., Lebel, T., Marticorena, B., Mounier, F., Nedelec, P., Redelsperger, J.-L., Ravegnani, F., Reeves, C. E., Roca, R., de Rosnay, P., Schlager, H., Sultan, B., Tomasini, M., Ulanovsky, A., and ACMAD forecasters team, 2008: Large-scale overview of the summer monsoon over West Africa during the AMMA field experiment in 2006, Ann. Geophys., 26, 2569–2595.

47. Kanamitsu, M., W. Ebisuzaki, J. Woollen, S.-K. Yang, J. J. Hnilo, M. Fiorino, and G. L. Potter, 2002a: NCEP–DOE AMIP-II Reanalysis (R-2). *Bull. Amer. Meteor. Soc.*, **83,** 1631–1643.

48. Kemball-Cook, S. R. and B. C. Weare, 2001: The onset of convection in the Madden-Julian Oscillation. *J. Climate*, 14, 780-793.

49. Kiladis, G. N., G. A. Meehl, and K. M. Weickmann, 1994: Large-scale circulation associated with westerly wind bursts and deep convection over the western equatorial Pacific, *J. Geophys. Res.*, 99(D9), 18,527–18,544, doi:10.1029/94JD01486.

50. Kiladis, G. N., K. H. Straub, and P. T. Haertel, 2005: Zonal and vertical structure of the Madden–Julian Oscillation. *J. Atmos. Sci.*, **62,** 2790–2809.

51. Kiladis, G. N., and M. Wheeler, 1995: Horizontal and vertical structure of observed tropospheric equatorial Rossby waves. *J. Geophys. Res.*, **100** (D11), 22 981–22 997.

52. Knutson, D. R., K. M. Weickmann, and J. E. Kutzbach, 1986: Global-scale intraseasonal oscillations of outgoing longwave radiation and 250 mb zonal wind during Northern Hemisphere summer. *Mon. Wea. Rev.*, **114,** 605–623.

53. Knutson, D. R., and K. M. Weickmann, 1987: 30–60 day atmospheric oscillations: Composite life cycles of convection and circulation anomalies. *Mon. Wea. Rev.*, **115,** 1407–1436.

54. Landsea, C. W., G. D. Bell, W. M. Gray, and S. B. Goldenberg, 1998: The extremely active 1995 Atlantic hurricane season: Environmental conditions and verification of seasonal forecasts. *Mon. Wea. Rev.*, **126,** 1174–1193.

55. Lau, K.-H., and N.-C. Lau, 1992: The energetics and propagation dynamics of tropical summertime synoptic-scale disturbances. *Mon. Wea. Rev.*, **120,** 2523–2539.

56. Lavender S. L., Matthews A. J.., 2009: Response of the West African monsoon to the Madden-Julian oscillation. *Journal of Climate* **22**: 4097–4116, DOI:10.1175/2009JCLI2773.1.

57. Le Barbe´, L., T. Lebel, and D. Tapsoba, 2002: Rainfall variability in West Africa during the years 1950–90. *J. Climate,* **15,** 187–202.

58. Lebel, T., Parker, D. J., Bourles, B., Flamant, C., Marticorena, B., Peugeot, C., Gaye, A., Haywood, J., Mougin, E., Polcher, J., Redelsperger, J.-L., and Thorncroft, C. D., 2010: The AMMA field campaigns: multiscale and multidisciplinary observations in the West African region, *Q. J. R. Meteorol. Soc.* **136**: 8–33.

59. Lin, J-L., B. Mapes, M. Zhang, and M. Newman, 2004: Stratiform precipitation, vertical heating profiles, and the Madden-Julian Oscillation. *J. Atmos. Sci.*, 61, 296-309.

60. Lin, X., and R. H. Johnson, 1996: Kinematic and thermodynamic characteristics of the flow over the western Pacific warm pool during TOGA COARE. J. Atmos. Sci., **53,** 695–715.

61. Lindzen, R. S., 1967: Planetary waves on beta planes. Mon. Wea. Rev., **95,** 441–451.

62. Lindzen, R.S., 1974: Wave-CISK in the Tropics. *J. Atmos. Sci.,* **31,** 156–179.

63. Madden, R. A., and P. Julian, 1971: Detection of a 40-50 day oscillation in the zonal wind. *J. Atmos. Sci.*, 28, 702-708.

64. Madden, R., and P. Julian, 1994: Observations of the 40–50-day tropical oscillation—A review. *Mon. Wea. Rev.*, **122,** 814–837.

65. Majda, A. J., and S. N. Stechmann, 2009: A Simple Dynamical Model with Features of Convective Momentum Transport. *J. Atmos. Sci.*, **66**, 373–392.

66. Maloney, E. D., and D. L. Hartmann, 1998: Frictional moisture convergence in a composite life cycle of the Madden-Julian Oscillation. *J. Climate*, 11, 2387-2403.

67. Maloney, E. D., and D. L. Hartmann, 2000a: Modulation of eastern North Pacific hurricanes by the Madden-Julian oscillation. *J. Climate*, 13, 1451-1460.

68. Maloney, E. D., and D. L. Hartmann, 2000b: Modulation of hurricane activity in the Gulf of Mexico by the Madden–Julian oscillation. *Science,* **287,** 2002–2004.

69. Maloney, E. D., and J. Shaman, 2008: Intraseasonal variability of the West African monsoon and the Atlantic ITCZ. *J. Climate*, 21, 2898-2918.

70. Maloney, E. D., and A. H. Sobel, 2004: Surface fluxes and ocean coupling in the tropical intraseasonal oscillation. *J. Climate*, 17, 4368-4386.

71. Maloney, Eric D., Adam H. Sobel, 2007: Idealized Hot Spot Experiments with a General Circulation Model. *J. Climate*, **20**, 908–925.

72. Mapes, B. E., 1997: Equilibrium versus activation control of largescale variations of tropical deep convection. *The Physics and Parameterization of Moist Convection,* R. K. Smith, Ed., Kluwer Academic, 512 pp.

73. Mapes, B. E., 2000: Convective inhibition, subgrid-scale triggering energy, and stratiform instability in a toy tropical wave model. *J. Atmos. Sci.,* **57,** 1515–1535.

74. Mapes, B. E., and R. A. Houze , 1995: Diabatic divergence profiles in western Pacific mesoscale convective systems. *J. Atmos. Sci.,* **52,** 1807–1828.

75. Matsuno, T., 1966: Quasi-geostrophic motions in the equatorial area. *J. Meteor. Soc. Japan,* **44,** 25–43.

76. Matthews, A. J., 2000: Propagation mechanisms for the Madden–Julian oscillation. *Quart. J. Roy. Meteor. Soc.,* **126,** 2637–2652.

77. Matthews, A. J., 2004: Intraseasonal variability over tropical Africa during northern summer. *J. Climate,* **17,** 2427–2440.

78. McPhaden, M. J., H. P. Freitag, S. P. Hayes, B. A. Taft, Z. Chien, and K. Wyrtki, 1988: The response of the equatorial Pacific Ocean to a westerly wind burst in may 1986. *J. Geophys. Res.,* **93** (C9), 10 589–10 603.

79. Mekonnen, A., C. D. Thorncroft, and A. R. Aiyyer, 2006: Analysis of convection and its association with African easterly waves. J. Climate, in press.

80. Mo, Kingtse C., 2000: The Association between Intraseasonal Oscillations and Tropical Storms in the Atlantic Basin. *Mon. Wea. Rev.*, **128**, 4097–4107.

81. Neelin, J. D., I. M. Held, and K. H. Cook, 1987: Evaporation-wind feedback and low-frequency variability in the tropical atmosphere. *J. Atmos. Sci.* 44, 2341-2348.

82. Neelin, J. D., and J.-Y. Yu, 1994:Modes of tropical variability under convective adjustment and the Madden-Julian Oscillation. Part I: Analytical theory. *J. Atmos. Sci.*, 51, 1876-1894.

83. Oouchi, K., 1999: Hierarchical organization of super cloud cluster caused by WISHE, convectively induced gravity waves and cold pool. *J. Meteor. Soc. Japan*, **77,** 907–927.

84. Pohl, Benjamin, Serge Janicot, Bernard Fontaine, Romain Marteau, 2009: Implication of the Madden–Julian Oscillation in the 40-Day Variability of the West African Monsoon. *J. Climate*, **22**, 3769–3785. doi: 10.1175/2009JCLI2805.1.

85. Pytharoulis, I. and C. Thorncroft, 1999: The low-level structure of African easterly waves in *1995*. *Mon. Wea. Rev.*, 127:2266–2280.

86. Raymond, David J., Željka Fuchs, 2009: Moisture Modes and the Madden–Julian Oscillation. *J. Climate*, **22**, 3031–3046. doi: 10.1175/2008JCLI2739.1

87. Redelsperger, J.-L., A. Diongue, A. Diedhou, J.-P. Ceron, M. Diop, J.-F. Gueremy, and J.-P. Lafore, 2002: Multi-scale description of a Sahelian synoptic weather system representative of the West African Monsoon. *Quart. J. Roy. Meteor. Soc.*, **128,** 1229–1257.

88. Reed, R. J., J. C. Norquist, and E. E. Recker, 1977: The structure and properties of African wave disturbances as observed during phase III of GATE. *Mon. Wea. Rev.,* **105,** 317–333.

89. Rennick, M. A., 1976: The generation of African waves. *J. Atmos. Sci.,* **33,** 1955–1969.

90. Robinson, G. J., and K. I. Hodges, 2005: Cloud Archive User Service User Guide. *NERC Environmental Systems Science Centre*. 1-16.

91. Schubert, W. H., P. E. Ciesielski, D. E. Stevens, and H. Kuo, 1991: Potential vorticity modeling of the ITCZ and the Hadley circulation. *J. Atmos. Sci.*, **48,** 1493–1509.

92. Seiki, A., and Y. N. Takayabu, 2007: Westerly wind bursts and their relationship with intraseasonal variations and ENSO. Part I: Statistics. Mon. Wea. Rev., 135, 3324–3345.

93. Shaman, J., S. K. Esbensen, E. D. Maloney, 2009: The Dynamics of the ENSO–Atlantic Hurricane Teleconnection: ENSO-Related Changes to the North African–Asian Jet Affect Atlantic Basin Tropical Cyclogenesis. *J. Climate,* **22**, 2458–2482. doi: 10.1175/2008JCLI2360.1 .

94. J. Simmons, 1977: Baroclinic instability in the summer mesosphere. *Quarterly Journal of the Royal Meteorological Society,* **103**:435, 211-215.

95. Sobel, A. H., and C. S. Bretherton, 2000: Modeling Tropical Precipitation in a Single Column. *J. Climate,* **13**, 4378–4392.

96. Sobel, A. H., E. D. Maloney, G. Bellon, and D. M. Frierson, 2009: Surface fluxes and tropical intraseasonal variability: A reassessment, J. Adv. Model. Earth Syst., 2, Article 2.

97. Sobel, A. H., J. Nilsson, and L. M. Polvani, 2001: The weak temperature gradient and balanced tropical moisture waves. *J. Atmos. Sci.,* **58,** 3650–3665.

98. Sperber, K. R., 2003: Propagation and vertical structure of the Madden-Julian Oscillation. *Mon. Wea. Rev.*, 131, 3018-3037.

99. Straub, K. H., and G. N. Kiladis, 2002: Observations of a convectively coupled Kelvin wave in the eastern Pacific ITCZ, J. Atmos. Sci., 59, 30–53.

100. Sugiyama, M., 2009: The moisture mode in the quasi-equilibrium tropical circulation model. Part I: Analysis based on the weak temperature gradient approximation. *J. Atmos. Sci.*, 66, 1507-1523.

101. Sultan, B., and S. Janicot, 2000: Abrupt shift of the ITCZ over West Africa and intraseasonal variability. *Geophys. Res. Lett.,* **27,** 3353–3356.

102. Sultan, B., S. Janicot, A. Diedhiou, 2003: The West African Monsoon Dynamics. Part I: Documentation of Intraseasonal Variability. *J. Climate,* **16**, 3389–3406.

103. Sultan, B., and S. Janicot, 2003:West African monsoon dynamics. Part II: The ‘‘pre-onset’’ and the ‘‘onset’’ of the summer monsoon. *J. Climate,* **16,** 3407–3427.

104. Thayer-Calder, Katherine, David A. Randall, 2009: The Role of Convective Moistening in the Madden–Julian Oscillation. *J. Atmos. Sci.*, **66**, 3297–3312.

105. Thorncroft, C. D., and M. Blackburn, 1999: Maintenance of the African easterly jet. *Quart. J. Roy. Meteor. Soc.,* **125,** 763–786.

106. Thorncroft, C. D., and K. Hodges, 2001: African easterly wave variability and its relationship to Atlantic tropical cyclone activity. *J. Climate,* **14,** 1166–1179.

107. Thorncroft, C. D., and B. J. Hoskins, 1994a: An idealised study of African easterly waves. 1. A linear view. *Quart. J. Roy. Meteor. Soc.,* **120,** 953–982.

108. Thorncroft, C. D., and B. J. Hoskins, 1994b: An idealised study of African easterly waves. 2. A nonlinear view. *Quart. J. Roy. Meteor. Soc.,* **120,** 983–1015.

109. Thorncroft, C. D., and D. P. Rowell, 1998: Interannual variability of African wave activity in a general circulation model. *Int. J. Climatol.,* **18,** 1305–1323.

110. Thorncroft, C. D., N. M. J. Hall, and G. N. Kiladis, 2008: Three dimensional structure and dynamics of African easterly waves. Part III: Genesis, J. Atmos. Sci., 65, 3596–3607.

111. Vitart, F., and F. Molteni, 2010: Simulation of the Madden– Julian Oscillation and its teleconnections in the ECMWF forecast system. *Quart. J. Roy. Meteor. Soc.*, 136, 842-855.

112. Wallace. J. M., 1971: Spectral studies of tropospheric wave disturbances in the tropical western Pacific. *Rev. Geophys. Space Phys.*, **9**, 557-612.

113. Wang, B., 1988: Dynamics of tropical low-frequency waves: An analysis of the moist Kelvin wave. J. Atmos. Sci., 45, 2051-2065.

114. Wang, B., 2005: Theories. Intraseasonal Variability in the Atmosphere-Ocean Climate System, K. M. Lau and D. E. Waliser, Eds., Praxis, 307-360.

115. Wheeler, M. C., and H. H. Hendon, 2004: An all-season real-time multivariate MJO index: Development of an index for monitoring and prediction. *Mon. Wea. Rev.*, 132, 1917-1932.

116. Wheeler, M., and G. N. Kiladis, 1999: Convectively coupled equatorial waves: Analysis of clouds in the wavenumber-frequency domain. *J. Atmos. Sci.,* **56,** 374–399.

117. Wheeler, M., and K. M. Weickmann, 2001: Real-time monitoring and prediction of modes of coherent synoptic to intraseasonal tropical variability. *Mon. Wea. Rev.,* **129,** 2677–2694.

118. Wheeler, M., G. N. Kiladis, and P. J. Webster, 2000: Large-scale dynamical fields associated with convectively coupled equatorial waves. *J. Atmos. Sci.,* **57,** 613–640.

119. Yanai, M., and M. Murakami, 1970: Spectrum analysis of symmetric and antisymmetric equatorial waves. *J. Meteor. Soc. Japan,* **48,** 186–197.

120. Yu, J.-Y., and J. D. Neelin, 1994: Modes of tropical variability under convective adjustment and the Madden–Julian oscillation. Part II: Numerical results. *J. Atmos. Sci.,* **51,** 1895–1914.

121. Zhang, C., 2005: The Madden-Julian oscillation, Rev. Geophys.,43, RG2003, doi:10.1029/2004RG000158.